

MODELING AND SIMULATION OF A FLUTTERING BIOINSPIRED SUBMERSIBLE

By

Aren Michael Helling

A DISSERTATION

Submitted to
Michigan State University
in partial fulfillment of the requirements
for the degree of

DOCTOR OF PHILOSOPHY

Mechanical Engineering

2011

ABSTRACT

MODELING AND SIMULATION OF A FLUTTERING BIOINSPIRED SUBMERSIBLE

By

Aren Michael Hellum

A bioinspired submersible propelled by a fluttering, fluid-conveying tail was designed and analyzed. A simple model of the submersible was created by treating the rigid hull of the submersible as a rigid body boundary condition on the fluid-conveying tail. Curves of neutral stability were determined in the internal/external velocity parameter space for several values of rigid body mass, and the thrust produced by these neutrally-stable waveforms was determined using Lighthill's methods. The power required to produce these waveforms and their efficiency were also determined. The efficiency was found to be greater than 50%, comparable to a small marine propeller, but below the 90% quoted in fish propulsion literature.

A more general model of the submersible which removed many of the linearizing assumptions made in the simplified model was also developed and solved numerically. This model is comprised of the equations of motion for a non-inertial frame fixed on the rigid head of the submersible and the equations of motion for a fluid-conveying tail within that non-inertial frame. Simulations were made using several flexible tail geometries, as well as for a rigid tube and a rigid tail which was dimensionally identical to one of the geometries. The forward speed of the fluttering flexible tail configuration was found to be higher than that of the rigid tube configuration for one geometry, and higher than that of the rigid tail for most geometries. A prototype of this submersible was constructed, and qualitative features and findings of the general model were verified. The general model was also extended to

incorporate a time-variable velocity of the conveyed fluid, and a functional description of this velocity was found which caused the submersible to turn without the incorporation of additional actuators on the tail or hull-mounted fins.

Copyright by
AREN MICHAEL HELLUM
2011

TABLE OF CONTENTS

List of Tables	viii
List of Figures	ix
1 Motivation	1
2 Dynamics of a Pipe Conveying Fluid with a Non-Uniform Velocity Profile	5
2.1 Introduction	5
2.2 Background - Uniform Velocity Profile	6
2.3 Non-Uniform Velocity Profile	8
2.3.1 Triple plug flow model	8
2.3.2 N-plug flow model	11
2.4 Analysis of a Cantilever Pipe	13
2.4.1 Solution of the differential equation	13
2.4.2 Determination of momentum flux correction factor	14
2.5 Model Comparison:	
Uniform and Non-Uniform Flow	16
2.5.1 Turbulent flow	16
2.5.2 Laminar flow	20
3 Simplified Dynamics of a Fluid-Conveying, Fluid-Immersed Pipe Affixed to a Rigid Body	23
3.1 Introduction	23
3.2 Background	24
3.2.1 Fluid-conveying pipes	24
3.2.2 Slender body swimming	28
3.3 Fluid-conveying pipe affixed to a rigid body	32
3.3.1 Simplified boundary conditions	32
3.3.2 Method of analysis	35
3.4 Stability, thrust and efficiency	38
3.4.1 Neutral stability	38
3.4.2 Thrust characteristics	40
3.4.3 Hydrodynamic efficiency	42
4 General Dynamics of a Fluid-Conveying, Fluid-Immersed Pipe Affixed to a Rigid Body	46
4.1 Nomenclature	46

4.2	Introduction	51
4.3	Assumptions	52
4.4	Dynamic Model - Newtonian Formulation	55
4.4.1	Force and Moment Equations	55
4.4.2	Added Mass	60
4.4.3	Expansion of a General Volume Term	64
4.4.4	Individual Volume Terms	66
4.4.4.1	Rigid Head: Ω_h	66
4.4.4.2	Flexible Tail: Ω_t	66
4.4.4.3	Head Internal Fluid: Ω_1	67
4.4.4.4	Tail Internal Fluid: Ω_2	68
4.4.4.5	Head External Fluid: Ω_3	69
4.4.4.6	Tail External Fluid: Ω_4	69
4.4.5	Individual Surface Terms	70
4.4.5.1	Jet Inlet: Γ_1	70
4.4.5.2	Jet Outlet: Γ_2	71
4.4.5.3	External Flow Head Inlet: Γ_3	72
4.4.5.4	External Flow Head Outlet: Γ_4	73
4.4.5.5	External Flow Tail Inlet: Γ_5	73
4.4.5.6	External Flow Tail Outlet: Γ_6	74
4.4.6	Combined Scalar Equations	75
4.4.7	Pressure and Drag Forces	79
4.5	Dynamics of the Flexible Tail	81
4.5.1	Equations of Motion	81
4.5.2	Discretization	86
4.6	Numerical Simulations	88
4.6.1	Simulation Parameters and Procedure	88
4.6.2	Estimation of Drag Coefficients	88
4.6.3	Simulation Results	91
4.7	Validation	96
5	Experimental Studies and Control	99
5.1	Introduction	99
5.2	Experiments	101
5.2.1	SPI Performance	103
5.3	Effect of Time-Varying Internal Fluid Velocity	105
5.3.1	Additional Terms	105
5.3.2	Numerical Simulations	108
6	Concluding Remarks and Future Work	113
6.1	Dynamics of a Pipe Conveying Fluid with a Non-Uniform Velocity Profile . .	113
6.2	Simplified Dynamics of a Fluid-Conveying, Fluid-Immersed Pipe Affixed to a Rigid Body	114

6.3	General Dynamics of a Fluid-Conveying, Fluid-Immersed Pipe Affixed to a Rigid Body	116
6.4	Experimental Studies and Control	118
Bibliography		121

LIST OF TABLES

4.1	Names of different fluid control volumes and control surfaces. Note that there is no need for a “head internal outlet” and “tail internal inlet”, since these surfaces are the same.	57
4.2	Parameters used in simulations	90
4.3	Different tail geometries and their forward speeds and steady-state oscillation amplitudes.	95
5.1	Mean speeds of the three configurations in experiments	104

LIST OF FIGURES

2.1	A fluid-conveying pipe and a magnified view of a small length element	7
2.2	Free-body diagram of (a) a fluid element and (b) its corresponding pipe element	7
2.3	A cross-sectional view of the three fluid volumes of a triple plug flow	9
2.4	Plot of the momentum flux correction factor μ as a function of the Reynolds number. The data points obtained through simulation are shown by circles. .	15
2.5	(a) Locus of the first three roots of $\text{Det}(\mathbf{Z}) = 0$ for uniform (dashed line) and non-uniform (solid line) flow models with $\beta = 0.3$ (b) A magnified image of the second root loci in (a).	17
2.6	Plot of (a) u_{cr} and (b) ω_{cr} for uniform (dashed line) and non-uniform (solid line) turbulent flow for different values of β	19
2.7	Left: Modes two and three of the uniform profile case prior to mode switch, $\beta = 0.385$. Right: Closeup of boxed region. The marked points are the values of each locus at $u = 8.498$, and are at points (23.75, 5.64) and (24.46, 6.25) for the second and third mode, respectively.	19
2.8	Left: Modes two and three of the uniform profile case after mode switching has occurred, $\beta = 0.387$. Right: Closeup of boxed region. The marked points are the values of each locus at $u = 8.502$, and are at points (23.60, 6.08) and (24.59, 5.92) for the second and third mode, respectively.	20
2.9	Closeup of second mode, where $\beta = 0.290, 0.297, 0.305$ in the direction of the plotted arrow.	21
2.10	Plot of (a) u_{cr} and (b) ω_{cr} for uniform (thin line) and laminar (thick line) flow for different values of β	22
3.1	A cantilevered fluid-conveying pipe, with a magnified view of a small length element.	25

3.2	The cross-section of a finned tube with fluid-conduit diameter D and tail span S . The dotted circle describes the area responsible for the added external mass M_e , which is equal to $0.25\rho_f\pi S^2$, where ρ_f is the density of the external fluid.	26
3.3	The proposed submersible, comprised of a rigid body and a fluid-conveying flexible tail. Note that the tail is assumed to have a finned-tube cross section, as shown in Fig.3.2.	29
3.4	Free-body diagrams of the rigid body and tail of the submersible in Fig.3.3.	33
3.5	Argand diagram for the first three modes of oscillation for $\beta_i = 0.01$, $\beta_e = 0.9$, $\lambda = 1/2$, $\psi_B = 1/12$, $\mu = 2.25$ and $u_e = 1.0$.	36
3.6	Illustration of the procedure used to find the neutral stability curve.	37
3.7	Neutral stability curves for different values of μ .	39
3.8	Plot showing the relationship between ω_{cr} and u_e for different values of μ .	40
3.9	The darkened region of each neutral stability curve (left of the dotted lines) depicts the region of negative thrust.	41
3.10	Efficiency for neutrally stable points in the u_i - u_e space and for different values of μ . Note that the curve for $\mu = 2.5$ is unique in that it has an interim region of zero efficiency.	43
3.11	Efficiency as a function of u_i and u_e for the mass fraction $\mu = 2.5$.	44
4.1	A submersible with a fluid-conveying flexible tail. The submersible is propelled by the combined action of the fluid jet and fluttering tail. In this figure, the deflection of the tail has been exaggerated.	53
4.2	The cross-section of (a) the rigid head of the submersible at some point along its length, and (b) the flexible tail of the submersible, which is a finned tube. In both figures, the dotted circle describes the area responsible for the added fluid mass in the y direction.	54
4.3	Depiction of control volumes Ω_h , Ω_t , and Ω_i , $i = 1, 2, 3, 4$; and control surfaces Γ_j , $j = 1, 2, 3, 4, 5, 6$, along with their outward normals.	56

4.4	Free-body diagrams of (a) a differential element of Ω_2 (tail internal fluid), (b) a differential element of Ω_t (flexible tail), and (c) a differential element of Ω_4 (tail external fluid).	82
4.5	A fluid-conveying beam in the form of a finned-tube with fin height h	89
4.6	The subplot on the left shows the forward speed of the submersible with flexible tail, rigid tail, and rigid tube configurations. On the right, the displacement of the tail tip $y(L)$ and orientation θ of the rigid head of the submersible are given for the flexible tail configuration.	92
4.7	Sequence of images of the submersible with the flexible tail. The scaling for the y axis has been adjusted to make the tail oscillations more visible.	94
4.8	The subplot on the left shows the forward speed of the submersible with $L = 0.30, 0.34$ and 0.38 where $h = 0.077$. On the right, the displacement of the tail tip $y(L)$ is shown for these tail configurations.	95
4.9	The subplot on the left shows the forward speed of the submersible with $h = 0.067, 0.072$ and 0.077 where $L = 0.34$. On the right, the deflection of the tail tip $y(L)$ is shown for these tail configurations.	96
4.10	Displacement of the tail tip $y(L)$ in mm for a cantilever, $U = U_{cr} = 2.372$ m/s. Neutral stability is evident, since the oscillations of the tail are neither growing nor shrinking over time.	97
5.1	Exterior of the current prototype SPI, with marked features of interest. For interpretation of the references to color in this and all other figures, the reader is referred to the electronic version of this dissertation.	101
5.2	High-speed images of the submersible with the flexible tail acquired over a period of 1 sec, soon after it started from rest in the MSU swimming pool. The average speed of the submersible in these images was $\approx 0.4 \text{ BL/s}$, less than the maximum speed of $\approx 1.15 \text{ BL/s}$. Note the large deflections of the tail which occur during acceleration.	103
5.3	Mean speeds of the configurations listed in Table 5.1. The error bars express the 95% confidence intervals.	105
5.4	Comparison of the constant-velocity $U = 4.0$ case to non-constant velocity case where $\alpha = 40, k = 0.75$	110

5.5	Comparison of three values of k : 0.25, 0.75 and 1.0. The scaling parameter $\alpha = 40$ for all cases.	111
5.6	An image sequence of the submersible during a turn. Note that the dashed line is collinear with the non-inertial x axis.	112

Chapter 1

Motivation

Fish-like propulsion has been a matter of academic interest since Gray's pioneering work in the 1930's; the oft-cited "Gray's Paradox" is derived from a 1936 paper [14] in which the speed attained by a dolphin was calculated to require approximately seven times the power available to the animal. Though later workers resolved this apparent paradox (see the work by Fish [12]), interest in the efficiency of fish-like motion has been sustained to the present day. An early model of oscillatory propulsion Taylor [42] was based on calculation of the resistive force applied by the surrounding fluid; this model, which neglects inertial effects, is more appropriate to the study of low-Reynolds number propulsion, such as that of spermatozoa. These inertial effects were accounted for by Lighthill in his seminal 1960 paper [23] which used slender-body theory to approximate the effect of the pressure field surrounding the fish. Lighthill found that a travelling waveform with higher amplitude at the tail than the head is required to produce efficient thrust. Later works have extended these initial efforts to account for a planform of variable height [44], deflections of arbitrary amplitude [26], and to account for the wing-like "lunate" tail which is a feature of the fastest

carangiform¹ swimmers [11], along with a host of other works.

The continued drive within the academic community to “chase the tail” is in large part due to impressive estimates of efficiency. For example, Lighthill’s slender body methods estimate that 90% of the power expended by a swimming fish is available to propel the fish, and that the remainder is wasted, serving only to raise the kinetic energy in the wake. This value of 90% “Froude” efficiency lines up well with a figure of 87% found by Anderson and coworkers [2] found on a simplified experimental setup. Some simplifications were required to obtain these figures; it is difficult to precisely measure the efficiency of a self-propelled swimming body, since the sources of drag and thrust cannot be separated. An interesting paper by Schultz and Webb [37] describes a variety of approaches which have been employed to determine drag and thrust, but they conclude that forward speed is the most robust way of determining whether a tail waveform is superior to another for a given platform.

This interest has manifested itself in a number of robotic platforms designed to harness the efficiency of fish-like motion. The MIT RoboTuna [5, 43] is a well known “biomimetic” platform. That device employs a tail composed of several links covered by a Neoprene sheath. These links were then individually actuated in an approximation of a fishes motion. A different type of linked system was built by McMasters and coworkers [27] which used a novel geared mechanism to produce a fish-like motion using only a single servomotor, while a third approach was taken by Alvarado and Youcef-Toumi [1], who described a system which used a wholly flexible tail, excited with a single actuator at the base. These platforms are simply some of the more complex and recent devices; experimental devices used to measure

1: “Carangiform” swimming is typified by large amplitude motion concentrated in the posterior half of a swimming fishes body. The term is used in contrast to “anguilliform” motion, in which large amplitude deflections take place over the length of the creature’s body. Lighthill’s excellent review paper [24] describes these and other propulsion mechanisms in more detail.

fish propulsion were built as early as 1933 [13]. Other devices have also been built to investigate single aspects of fish swimming, such as the caudal fin work of Anderson and coworkers [2], and studies of pectoral fin swimming undertaken by Lauder and coworkers [22].

A fundamental difference between the approaches taken by Triantafyllou [43] and Alvarado and Youcef-Tuomi [1] is that the RoboTuna’s need to independently actuate its linked tail means that the system must essentially be driven against its natural dynamics. In contrast, the flexible tail described in [1] can be induced to oscillate near its natural frequency. This approach can lead to reduced transmission losses and lower motor bandwidth requirements, and the mechanism so produced can easily be made very robust, since it consists of a single flexible element. The present work proposes a sort of flexible tail that is fundamentally different from that described by Alvarado. Specifically, the desired traveling waveform is produced not by an actuator at the base, but instead by flutter instability induced in a slender tail by conveying fluid down its center. This instability is sometimes referred to as the “garden hose instability”, after the tendency of such a hose to whip about when the faucet is opened too far.

The fluid-conveying pipes and flutter instability are well-represented in the academic literature - the lists of papers cited in Paidoussis’ review books on the topic [30, 31] are a testament to this. However, the literature is largely grounded in a relatively small number of applications, such as pipeline vibrations [3]. Therefore, even a simplified model of a fluttering fluid-conveying submersible requires expansion of the literature.

This work is organized as follows. Chapter 2 derives the equations of motion for a fluid-conveying pipe, and presents a simple way to account for a non-uniform velocity profile found

in real pipe flow. Chapter 3 presents a simple, analytically tractable model of a fluttering fluid-conveying submersible, consisting of a rigid body affixed to one end of a fluid-conveying tail. This rigid body boundary condition, while not particularly unusual, had never been presented in the fluid-conveying pipe literature. Chapter 3 also presents some estimates of thrust and efficiency for a fluid-conveying tail's waveform based on the results of Lighthill [23] and Wu [44].

Chapter 4 derives a considerably more complex model of the submersible, a model which is able to account for the general motion of a fluttering fluid-conveying submersible within a plane. As with the rigid body boundary condition, it is interesting that despite the well-developed state of the literature, the equations of motion for a fluid-conveying pipe in a non-inertial reference frame have not been presented. Chapter 5 discusses previous designs of fish-like submersibles and presents preliminary experimental data from a platform designed at Michigan State University. The equations of motion derived in Chapter 4 are also extended to account for a time-varying velocity of the conveyed fluid and are solved with an eye toward maneuvering the submersible. Conclusions and thoughts for the direction of future research on this topic are provided in Chapter 6.

Chapter 2

Dynamics of a Pipe Conveying Fluid with a Non-Uniform Velocity Profile

2.1 Introduction

Analytical treatments of the fluid-conveying pipe problem typically invoke the “plug flow” assumption, under which the velocity profile is uniform across the cross-section of the pipe. At high Reynolds number, this assumption is approximately correct, since the velocity profile is nearly uniform over the central region of the cross-section, with only a thin, highly sheared annular region near the pipe wall. The plug flow assumption is less valid at low Reynolds numbers, since a larger fraction of the fluid at a given cross section has significantly different momentum than the average fluid element at that cross section. The deviation from the plug flow assumption is particularly apparent for laminar flow. This chapter presents a method by which the boundaries of flutter instability of pipes conveying low Reynolds number fluid may be determined.

This chapter is organized as follows. The equation of motion of a pipe conveying fluid with a uniform velocity profile (plug flow) is first presented in Section 2.2 as background material. The derivation of plug flow is extended to a non-uniform velocity profile in Section 2.3. A flow model composed of three concentric plugs of fluid derived first and extended to N plugs; large values of N can be used to model an arbitrary velocity profile. The resulting equation for the non-uniform flow differs from the standard equation for uniform flow by a single constant; it is highly tractable, requiring no more effort to solve than the standard equation. This constant, a momentum flux correction factor similar to that used in many fluid mechanics texts [33], is determined in Section 2.4. The equations of motion for a cantilever pipe are solved and the results for the uniform and non-uniform flow equations are compared in Section 2.5 for both laminar and turbulent flow.

2.2 Background - Uniform Velocity Profile

Consider the fluid-conveying pipe in Fig.2.1 where U denotes the fluid velocity (constant) relative to the pipe. Assuming an Euler-Bernoulli beam model of the pipe, its equation of motion [30] can be written as follows

$$EI \frac{\partial^4 y}{\partial x^4} + MU^2 \frac{\partial^2 y}{\partial x^2} + 2MU \frac{\partial^2 y}{\partial x \partial t} + (M + m) \frac{\partial^2 y}{\partial t^2} = 0, \quad (2.1)$$

where E and I are the Young's modulus of elasticity and area moment of inertia of the cross-section of the pipe, and M and m are the fluid mass and pipe mass per unit length. The above equation can be obtained by showing that the rate of change of linear momentum

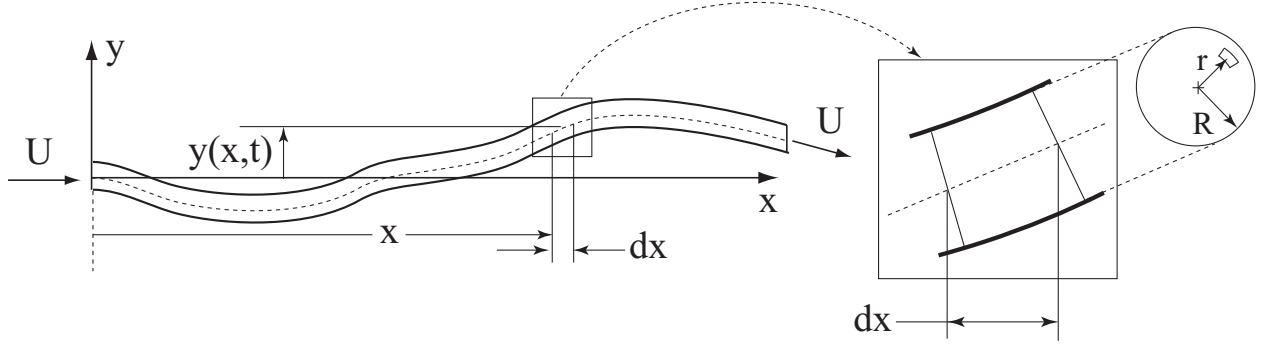


Figure 2.1: A fluid-conveying pipe and a magnified view of a small length element

of a fluid element is given by the expression [30]

$$\frac{d\vec{L}}{dt} = M \left[\frac{\partial}{\partial t} + U \frac{\partial}{\partial x} \right]^2 y dx \hat{j}$$

and from the equations of motion of a fluid element and its corresponding pipe element

Fig.2.2 in the x and y directions

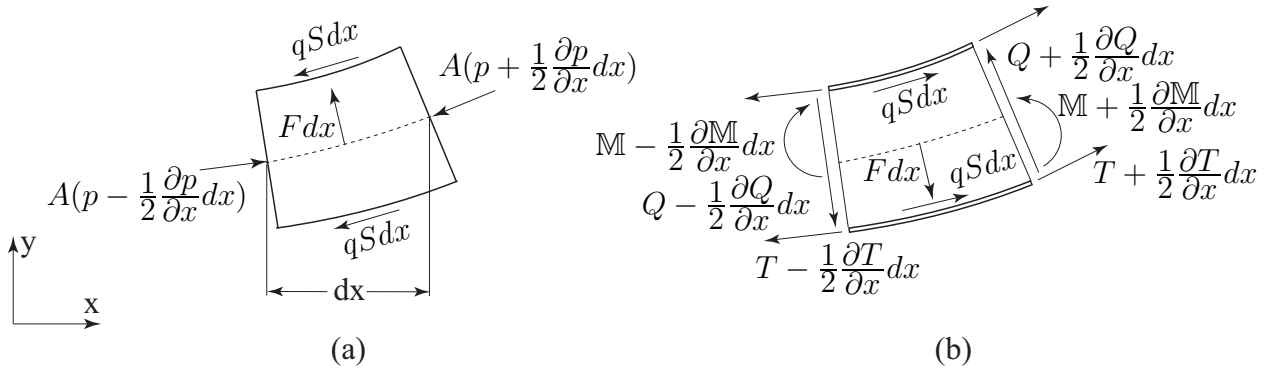


Figure 2.2: Free-body diagram of (a) a fluid element and (b) its corresponding pipe element

Plug fluid element:

$$-A \frac{\partial p}{\partial x} - qS - F \frac{\partial y}{\partial x} = 0, \quad (2.2)$$

$$F - A \frac{\partial}{\partial x} \left(p \frac{\partial y}{\partial x} \right) - qS \frac{\partial y}{\partial x} = M \left[\frac{\partial}{\partial t} + U \frac{\partial}{\partial x} \right]^2 y, \quad (2.3)$$

Pipe element:

$$\frac{\partial T}{\partial x} + qS + F \frac{\partial y}{\partial x} - Q \frac{\partial^2 y}{\partial x^2} = 0, \quad (2.4)$$

$$\frac{\partial Q}{\partial x} - F + \frac{\partial}{\partial x} \left(T \frac{\partial y}{\partial x} \right) + qS \frac{\partial y}{\partial x} = m \frac{\partial^2 y}{\partial t^2}. \quad (2.5)$$

In Eqs.(2.2) through (2.5), A denotes the cross-sectional area of the pipe, S denotes its internal surface area per unit length, p denotes the fluid pressure, q denotes the shear stress in the fluid, and F denotes the force per unit length normal to the wall. For the pipe element, Q , \mathbb{M} and T denote the traverse shear force, bending moment, and tension, respectively.

2.3 Non-Uniform Velocity Profile

2.3.1 Triple plug flow model

The triple plug flow model assumes three concentric volumes of fluid being conveyed through the pipe; the cross-sectional area of these volumes are shown in Fig.2.3. The flow velocity is different for the three volumes but is assumed to be constant within each volume. The triple plug flow is not physically realizable but its analysis provides the framework for investigation of a general velocity profile. Note that the fluid volume at the center (marked 1 in Fig.2.3) has a single fluid-fluid interface; the volume in the middle (marked 2 in Fig.2.3) has two fluid-fluid interfaces; and the outermost fluid volume (marked 3 in Fig.2.3) has one fluid-fluid and one fluid-pipe interface. The analysis for a general velocity profile will require us to introduce more volumes with two fluid-fluid interfaces, similar to volume 2. It is for this reason that three “plugs” are required; using fewer does not give rise to volumes with two

fluid-fluid interfaces, and using more creates redundant elements.

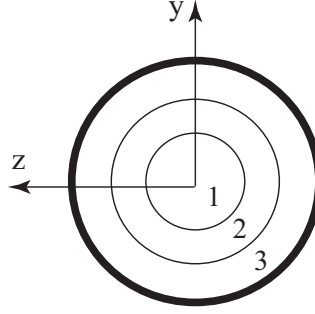


Figure 2.3: A cross-sectional view of the three fluid volumes of a triple plug flow

To extend the analysis of plug flow in section 2.2 to triple plug flow, we first denote the cross-sectional areas of volumes 1, 2, and 3 as A_1 , A_2 and A_3 respectively; their flow velocities as U_1 , U_2 and U_3 respectively; and their mass per unit length as M_1 , M_2 and M_3 respectively. F_{12} , F_{23} and F_{3p} denote the radial force per unit length between fluid volumes 1 and 2, fluid volumes 2 and 3, and fluid volume 3 and the pipe, respectively. The shear force at these interfaces are denoted by q_{12} , q_{23} and q_{3p} respectively, and the surface area per unit length of these interfaces are denoted by S_{12} , S_{23} and S_{3p} respectively. The dynamics of the fluid volumes 1, 2 and 3 can now be replicated from Eqs.(2.2) and (2.3), and that of the pipe from Eqs.(2.4) and (2.5), as follows

Volume 1:

$$-A_1 \frac{\partial p}{\partial x} - q_{12} S_{12} - F_{12} \frac{\partial y}{\partial x} = 0, \quad (2.6)$$

$$F_{12} - p A_1 \frac{\partial^2 y}{\partial x^2} - q_{12} S_{12} \frac{\partial y}{\partial x} = M_1 \left[\frac{\partial}{\partial t} + U_2 \frac{\partial}{\partial x} \right]^2 y, \quad (2.7)$$

Volume 2:

$$-A_2 \frac{\partial p}{\partial x} - q_{23} S_{23} + q_{12} S_{12} - (F_{23} - F_{12}) \frac{\partial y}{\partial x} = 0, \quad (2.8)$$

$$(F_{23} - F_{12}) - p A_2 \frac{\partial^2 y}{\partial x^2} - (q_{23} S_{23} - q_{12} S_{12}) \frac{\partial y}{\partial x} = M_2 \left[\frac{\partial}{\partial t} + U_2 \frac{\partial}{\partial x} \right]^2 y, \quad (2.9)$$

Volume 3:

$$-A_3 \frac{\partial p}{\partial x} - q_{3p} S_{3p} + q_{23} S_{23} - (F_{3p} - F_{23}) \frac{\partial y}{\partial x} = 0, \quad (2.10)$$

$$(F_{3p} - F_{23}) - p A_3 \frac{\partial^2 y}{\partial x^2} - (q_{3p} S_{3p} - q_{23} S_{23}) \frac{\partial y}{\partial x} = M_3 \left[\frac{\partial}{\partial t} + U_3 \frac{\partial}{\partial x} \right]^2 y \quad (2.11)$$

Pipe:

$$\frac{\partial T}{\partial x} + q_{3p} S_{3p} + F_{3p} \frac{\partial y}{\partial x} - Q \frac{\partial^2 y}{\partial x^2} = 0, \quad (2.12)$$

$$\frac{\partial Q}{\partial x} - F_{3p} + T \frac{\partial^2 y}{\partial x^2} + q_{3p} S_{3p} \frac{\partial y}{\partial x} = m \frac{\partial^2 y}{\partial t^2}. \quad (2.13)$$

The summation of equations in the x direction, namely Eqs.(2.6), (2.8), (2.10) and (2.12), gives

$$-(A_1 + A_2 + A_3) \frac{\partial p}{\partial x} + \frac{\partial T}{\partial x} = 0$$

Note that $(A_1 + A_2 + A_3) = A$, where A is the inner cross-sectional area of the pipe. The above equation simplifies to

$$\frac{\partial}{\partial x}(T - pA) = 0$$

if $A \neq A(x)$, the same result as that which is obtained for plug flow. The summation of

equations in the y direction, Eqs.(2.7), (2.9), (2.11) and (2.13), gives

$$-pA \frac{\partial^2 y}{\partial x^2} + \frac{\partial Q}{\partial x} + T \frac{\partial^2 y}{\partial x^2} = \sum_{n=1}^3 M_n \left[\frac{\partial}{\partial t} + U_n \frac{\partial}{\partial x} \right]^2 y + m \frac{\partial^2 y}{\partial t^2}$$

Following the derivation of plug flow [30] and substituting $(T - pA) = 0$ and $Q = -EI \frac{\partial^3 y}{\partial x^3}$ into the above equation, the following expression is obtained:

$$EI \frac{\partial^4 y}{\partial x^4} + \left(\sum_{n=1}^3 M_n U_n^2 \right) \frac{\partial^2 y}{\partial x^2} + 2 \left(\sum_{n=1}^3 M_n U_n \right) \frac{\partial^2 y}{\partial x \partial t} + \left(m + \sum_{n=1}^3 M_n \right) \frac{\partial^2 y}{\partial t^2} = 0. \quad (2.14)$$

2.3.2 N-plug flow model

It is simple to envision the analysis of the preceding section with more volumes. The additional volumes, similar to Volume 2 of the triple plug flow in that they possess two fluid-fluid interfaces, do not complicate the analysis since all interfacial terms are cancelled. Thus Eq.(2.14) can be rewritten as

$$EI \frac{\partial^4 y}{\partial x^4} + \left(\sum_{n=1}^N M_n U_n^2 \right) \frac{\partial^2 y}{\partial x^2} + 2 \left(\sum_{n=1}^N M_n U_n \right) \frac{\partial^2 y}{\partial x \partial t} + \left(m + \sum_{n=1}^N M_n \right) \frac{\partial^2 y}{\partial t^2} = 0, \quad (2.15)$$

where N is any integer greater than three. For very large values of N , the volumes have infinitesimal thickness and the summations in the coefficients of Eq.(2.15) can be replaced with integrals. The average velocity of fluid over a cross section is defined as

$$\bar{U} = \frac{1}{A} \iint_A U(A) dA = \frac{2}{R^2} \int_0^R U(r) r dr$$

for a cylindrical pipe of radius R .

The coefficients of the dynamical equation in Eq.(2.15) can now be expressed as

$$\begin{aligned}
\left(\sum_{n=1}^N M_n U_n^2 \right) &= \rho_f \iint_A U^2(A) dA = 2\pi\rho_f \int_0^R U^2(r) r dr = \mu M \bar{U}^2, \\
2 \left(\sum_{n=1}^N M_n U_n \right) &= 2\rho_f \iint_A U(A) dA = 2\rho_f A \bar{U} = 2M \bar{U}, \\
\left(m + \sum_{n=1}^N M_n \right) &= m + M,
\end{aligned} \tag{2.16}$$

where ρ_f is the density of the conveyed fluid, and μ is the non-dimensional momentum flux correction factor. For a cylindrical pipe with a known fluid velocity profile $U(r)$, μ has the expression

$$\mu = \frac{2}{R^2} \int_0^R \left[\frac{U(r)}{\bar{U}} \right]^2 r dr. \tag{2.17}$$

Using the algebraic simplifications in Eq.(2.16), Eq.(2.15) can be rewritten as follows

$$EI \frac{\partial^4 y}{\partial x^4} + \mu M \bar{U}^2 \frac{\partial^2 y}{\partial x^2} + 2M \bar{U} \frac{\partial^2 y}{\partial x \partial t} + (m + M) \frac{\partial^2 y}{\partial t^2} = 0. \tag{2.18}$$

Note the similarity of Eq.(2.18) with that of plug flow given by Eq.(2.1). All terms are essentially identical with the exception of the additional constant μ , which is a function of the velocity profile. Note also that evaluation of Eq.(2.17) for a uniform velocity profile yields $\mu = 1$, meaning that Eq.(2.1) is consistent with its plug flow assumption under this expanded derivation.

2.4 Analysis of a Cantilever Pipe

2.4.1 Solution of the differential equation

The behavior of a fluid-conveying pipe for cantilever boundary conditions has been analyzed, namely

$$y(0, t) = 0, \quad \frac{\partial y(0, t)}{\partial x}(0, t) = 0, \quad \frac{\partial^2 y(L, t)}{\partial x^2} = 0, \quad \frac{\partial^3 y(L, t)}{\partial x^3} = 0, \quad (2.19)$$

The equation of motion is made non-dimensional with the following change of variables

$$Y = \frac{y}{L}, \quad X = \frac{x}{L}, \quad T = t \Omega.$$

By introducing the non-dimensional velocity, mass fraction and frequency as follows

$$u = \left(\frac{M}{EI} \right)^{1/2} \bar{U} L, \quad \beta = \frac{M}{m + M}, \quad \omega = \left(\frac{M + m}{EI} \right)^{1/2} \Omega L^2,$$

and assuming a separable form for $Y(X, T)$ such that

$$Y(X, T) = \phi(X) e^{-i\omega T}$$

the following non-dimensional equation of motion and boundary conditions are obtained:

$$\begin{aligned} \frac{d^4 \phi}{dX^4} + \mu u^2 \frac{d^2 \phi}{dX^2} + 2\beta^{1/2} u i \omega \frac{d\phi}{dX} - \omega^2 \phi &= 0 \\ \phi(0) = 0, \quad \frac{\partial \phi(0)}{\partial X}(0, t) &= 0, \quad \frac{\partial^2 \phi(1)}{\partial X^2} = 0, \quad \frac{\partial^3 \phi(1)}{\partial X^3} = 0 \end{aligned} \quad (2.20)$$

The solution of ϕ is assumed to be of the form $\phi(X) = Ae^{zX}$ and this yields the characteristic polynomial

$$z^4 + \mu u^2 z^2 + 2\beta^{1/2} ui\omega z - \omega^2 = 0. \quad (2.21)$$

For specific values of μ , u and β , Eq.(2.21) provides four roots, z_n , $n = 1, 2, 3, 4$, where $z_n = z_n(\omega)$. The complete solution of $\phi(X)$ has the form

$$\phi(X) = A_1 e^{z_1 X} + A_2 e^{z_2 X} + A_3 e^{z_3 X} + A_4 e^{z_4 X}$$

The solution of the equation above based on the boundary conditions in Eq.(2.20) results in the complete solution

$$Y(X, T) = \sum_{n=1}^4 A_n e^{z_n X} e^{i\omega T} = \sum_{n=1}^4 A_n \underbrace{e^{Re[z_n]X}}_{(i)} \underbrace{e^{i(Im[z_n]X + Re[\omega]T)}}_{(ii)} \underbrace{e^{-Im[\omega]T}}_{(iii)}$$

An inspection of the above equation indicates that $Y(X, T)$ is a product of three exponential terms of which the first term is bounded since X is bounded and the second term is oscillatory since the exponent is imaginary. The third term can grow unbounded with time if $Im[\omega] < 0$ and this represents unstable dynamics of the pipe. The exact mode and velocity at which the fluid-conveying pipe becomes unstable depends on the fluid mass fraction β .

2.4.2 Determination of momentum flux correction factor

For laminar flow, the Poiseuille solution of Navier-Stokes equation holds [33] and the value of μ can be analytically determined to be equal to 4/3 for a circular pipe. For turbulent flow, the value of μ approaches unity as the value of Reynolds number approaches infinity.

The literature [7] commonly cites single values of μ for turbulent flow based on the boundary layer model employed, and the values cited are derived using assumptions better suited to high-Reynolds number turbulence. Since the present work relaxes the assumption of high-Reynolds number turbulence, a model for μ such that $\mu = \mu(Re)$ is desired. Numerical values of μ for turbulent flow were calculated based on Eq.(2.17) using velocity profiles generated by the commercial software STAR-CCM. Even with this improved resolution, knowledge of μ is required for more values of the Reynolds number than are feasible to simulate. To predict the value of μ for laminar, transition, and turbulent flow regimes, the following curve-fit was employed:

$$\mu(Re) = \begin{cases} 4/3 & Re \leq 2200 \\ 3.647 - 0.001052 \times Re & 2200 < Re < 2413 \\ 1.04 + 167.2/Re & Re \geq 2413. \end{cases} \quad (2.22)$$

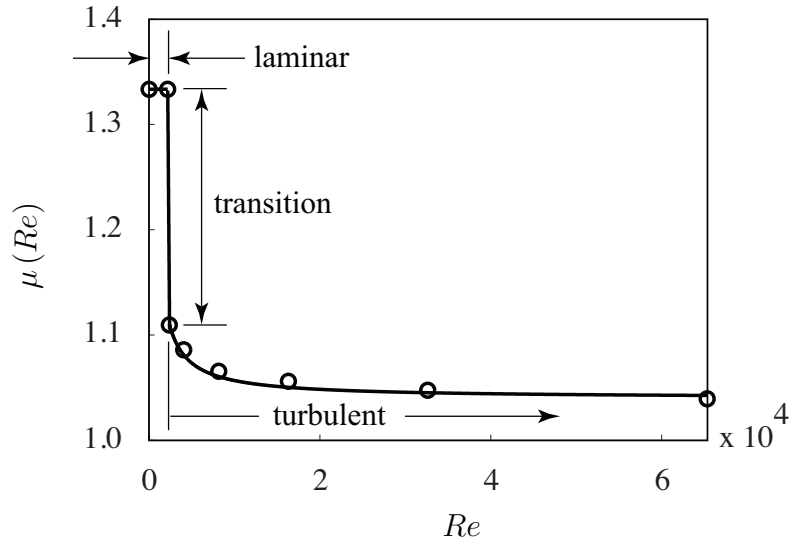


Figure 2.4: Plot of the momentum flux correction factor μ as a function of the Reynolds number. The data points obtained through simulation are shown by circles.

It can be seen from Fig.2.4 that the data points obtained from simulation matches well with the expression of μ in Eq.(2.22). The choice of $2200 < Re < 2413$ to define the “transition

region” is somewhat arbitrary, as might be the choice of using one single value for μ to represent a phenomenon as complex as turbulent transition. However, the authors note that for a given flow setup the range of velocities corresponding to transition flow is small, making the choice of the transition model relatively unimportant¹.

For a circular pipe, expressions can be determined which relate the non-dimensional velocity u and the Reynolds number:

$$u = \left(\frac{M}{EI}\right)^{1/2} \bar{U}L, \quad \text{Re} = \frac{\bar{U}D}{\nu} \quad \Rightarrow \quad u = \nu L \text{Re} \sqrt{\frac{\pi \rho_f}{4EI}}. \quad (2.23)$$

Clearly, a value of u does not uniquely determine the Reynolds number. The geometric properties of the pipe (L , E , I) and density and kinematic viscosity of the working fluid (ρ_f , ν) should be specified to determine the Reynolds number for a given u . Since the momentum flux correction factor μ is a function of the Reynolds number, it follows that the value of μ cannot be determined from the value of u alone.

2.5 Model Comparison:

Uniform and Non-Uniform Flow

2.5.1 Turbulent flow

The locus of the first three roots of $\text{Det}(\mathbf{Z}) = 0$ is shown in the Argand diagram in Fig.2.5(a) for $\beta = 0.308$ for both uniform and non-uniform flow models. Since the fluid-conveying pipe undergoes flutter instability in the second mode, a separate Argand diagram of the loci of the

1: The laminar to turbulent transition region can be seen in the Argand diagram in Fig.2.5.

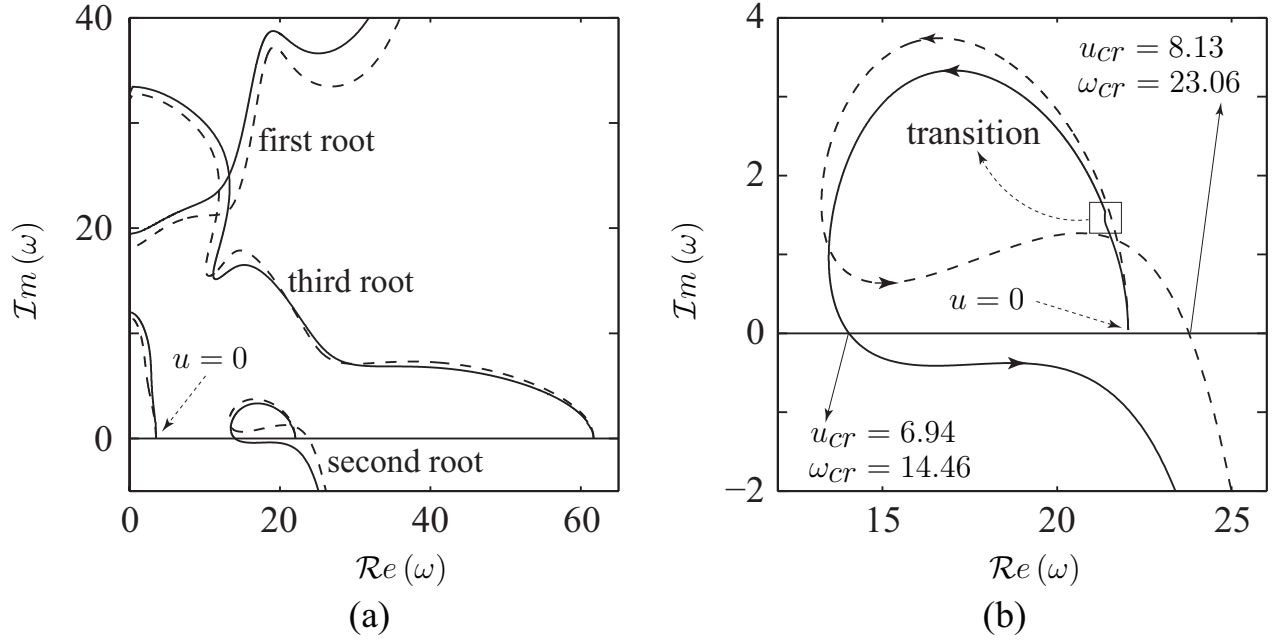


Figure 2.5: (a) Locus of the first three roots of $\text{Det}(\mathbf{Z}) = 0$ for uniform (dashed line) and non-uniform (solid line) flow models with $\beta = 0.3$ (b) A magnified image of the second root loci in (a).

second root is shown in Fig.2.5(b). The root loci for the uniform flow model are a function of u alone (μ is implicitly assumed to be unity) but they are a function of both u and μ for the non-uniform flow model. As noted in the previous section, the value of μ is not uniquely defined in terms of u . Certain dimensional coefficients related to the working fluid and pipe geometry must be assumed to obtain this relationship. The non-uniform flow model assumes water to be the working fluid ($\rho_f = 1000 \text{ kg/m}^3$, $\nu = 1.0 \times 10^{-6} \text{ m}^2/\text{s}$) and the following parameters for the pipe:

$$E = 1.7 \text{ MPa}, \quad I = 6.48 \times 10^{-10} \text{ m}^4, \quad L = 0.5 \text{ m}$$

It is acknowledged that the need to specify dimensional parameters is a limitation but this limitation is not significant. An inspection of Fig.2.4 reveals that μ is weakly related to

the Reynolds number for turbulent flow and therefore dependence of μ on the dimensional parameters is not significant.

It can be seen from Fig.2.5 that the root loci for the uniform and non-uniform flow models are quite different though their μ values are quite similar¹. A close look at the second root loci indicates that the uniform flow model predicts flutter instability of the pipe to occur for a critical velocity of $u_{cr} = 8.13$ with $\omega_{cr} = 23.06$ whereas the non-uniform flow model predicts significantly lower values of $u_{cr} = 6.94$ (15% lower) and $\omega_{cr} = 14.46$ (37% lower). Clearly, the dynamics of the system are very sensitive to the value of μ in the neighborhood of $\beta = 0.3$. The values of u_{cr} and ω_{cr} are plotted in Fig.2.6 for different values of β . This figure indicates that the non-uniform flow model predicts significantly lower values of u_{cr} and ω_{cr} for β in the neighborhood of 0.7 as well. There is good agreement between the uniform and non-uniform turbulent flow models for values of β that are not in the neighborhood of 0.3 or 0.7.

The system's behavior in the regions near $\beta = 0.3$ and $\beta = 0.7$ is somewhat different than what has appeared in the literature [15], since we are examining only the lowest velocity at which the pipe becomes unstable. The source of the system's sensitivity to changes in β is not a mode-switching phenomenon [38]. A mode switch for the uniform flow system does occur near $\beta = 0.386$, and this phenomenon is depicted in Figs.2.7 and 2.8.

Rather, the discontinuous behavior is a consequence of the unusual shape of the second mode's locus in this region of the β parameter space. Fig.2.9 shows the shape of second mode's locus in this sensitive region of the β -space. The $\beta = 0.297$ curve is nearly tangent to the real axis near $\omega = 16$ and the $\beta = 0.290, 0.305$ curves first cross the real axis at

1: The value of μ is implicitly assumed to be unity for the uniform flow model whereas it has values in the neighborhood of 1.05 for the non-uniform flow model.

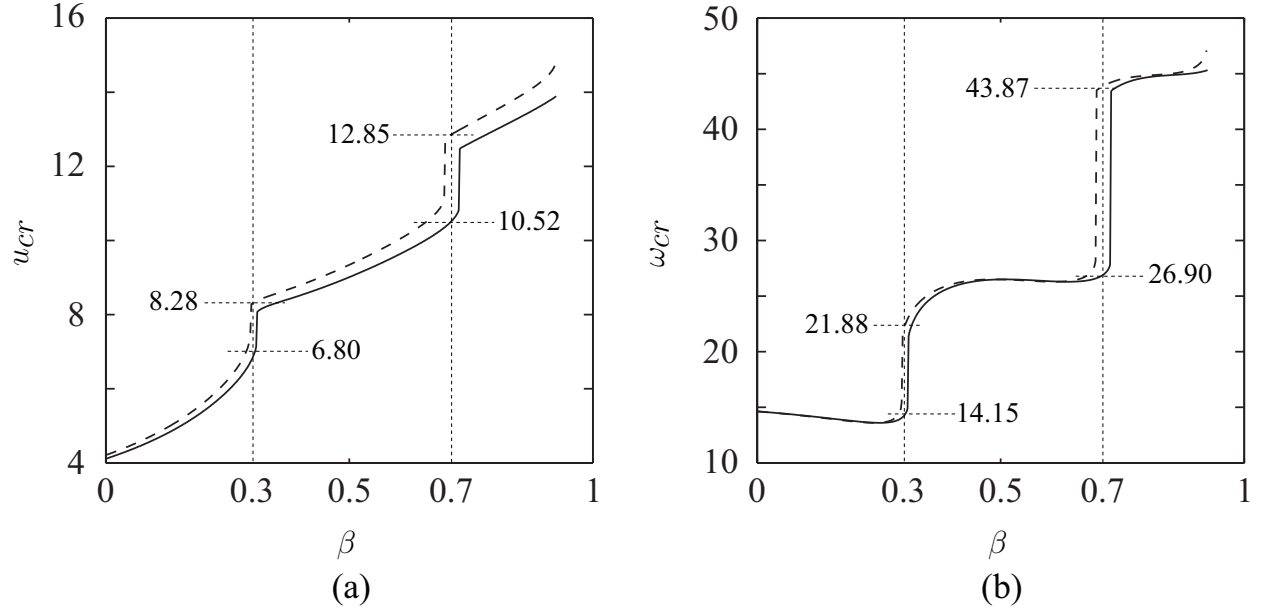


Figure 2.6: Plot of (a) u_{cr} and (b) ω_{cr} for uniform (dashed line) and non-uniform (solid line) turbulent flow for different values of β .

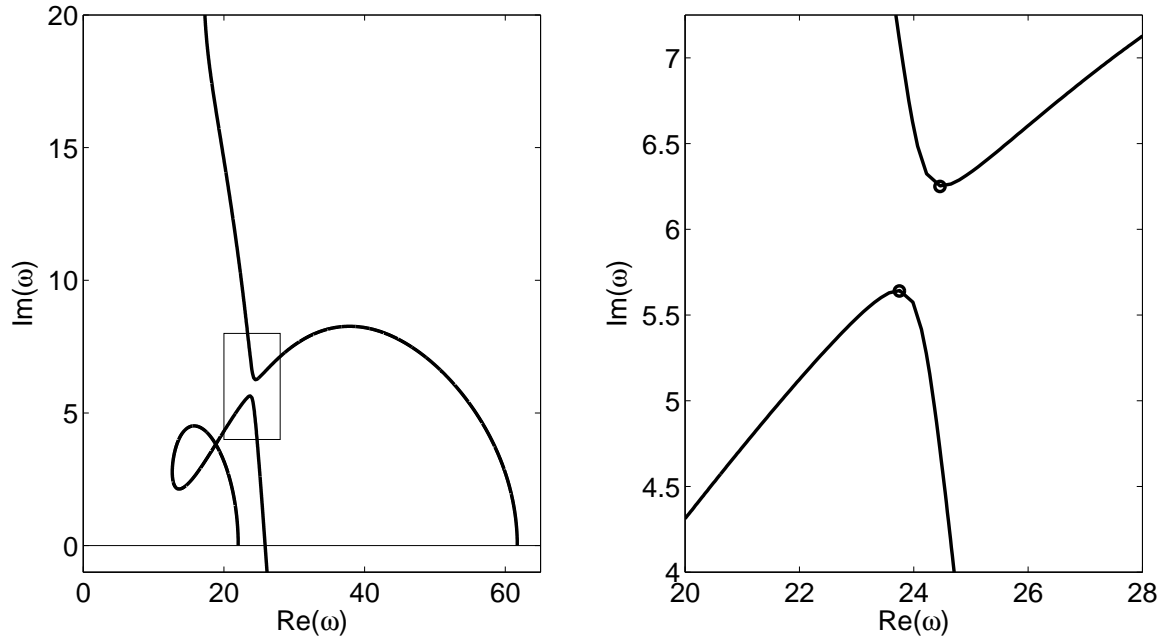


Figure 2.7: Left: Modes two and three of the uniform profile case prior to mode switch, $\beta = 0.385$. Right: Closeup of boxed region. The marked points are the values of each locus at $u = 8.498$, and are at points $(23.75, 5.64)$ and $(24.46, 6.25)$ for the second and third mode, respectively.

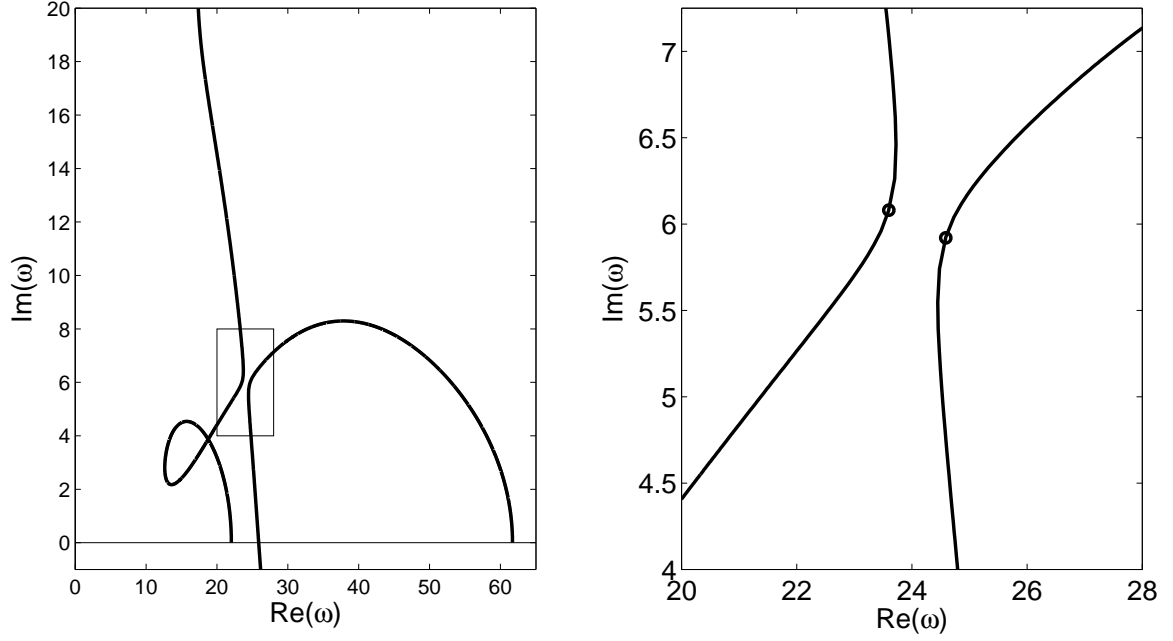


Figure 2.8: Left: Modes two and three of the uniform profile case after mode switching has occurred, $\beta = 0.387$. Right: Closeup of boxed region. The marked points are the values of each locus at $u = 8.502$, and are at points $(23.60, 6.08)$ and $(24.59, 5.92)$ for the second and third mode, respectively.

$\omega = 14.35$ and $\omega = 22.54$, respectively.

2.5.2 Laminar flow

In prior work, the plug flow model implicitly made the assumption that $\mu = 1$. It is clear from Fig.2.4 that this assumption is reasonable only for high Reynolds number. The non-unique relationship between u and Re allows situations where this assumption is not reasonable. For example, inspection of Eq.(2.23) reveals that a sufficiently long pipe could have a large value for u at low Reynolds number. A sufficiently long fluid-conveying pipe could therefore undergo flutter instability with laminar flow, in which case $\mu = 4/3$. In the case of turbulent flow, the near-unity value of μ yields values of u_{cr} and ω_{cr} which differ significantly from the uniform case only in certain thin regions of the β parameter space. Figure 2.10 is analogous

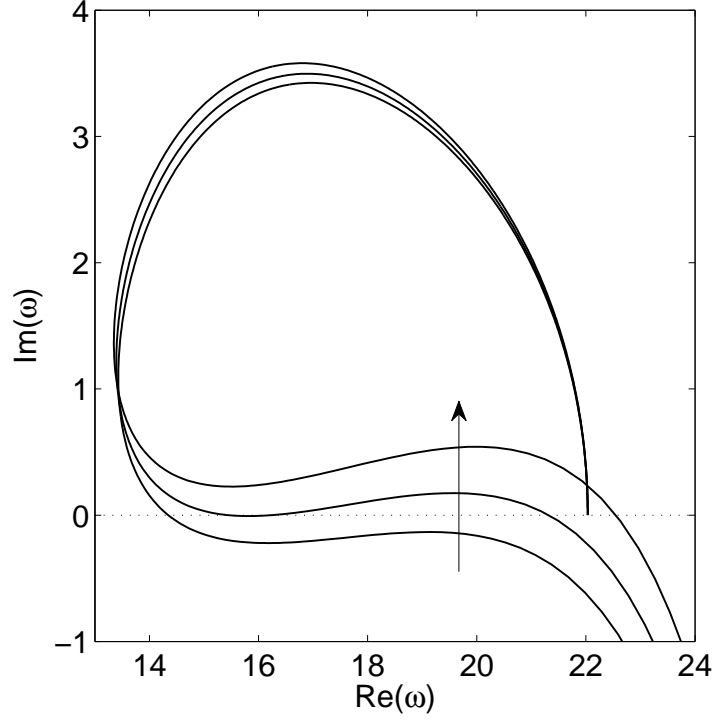


Figure 2.9: Closeup of second mode, where $\beta = 0.290, 0.297, 0.305$ in the direction of the plotted arrow.

to Fig.2.6, but assumes laminar flow and gives a very different result. The values of u_{cr} for laminar flow are quite different from that of uniform flow in all regions of the parameter space. The values of ω_{cr} for laminar flow are similar to that of uniform flow over much of the range of β but there are certain regions where the predicted values are significantly different. Unlike the thin regions near $\beta = 0.3$ and $\beta = 0.7$ for turbulent flow (see Fig.2.6), the regions of large separation for laminar flow extend from approximately $\beta = 0.29$ to $\beta = 0.40$ and from $\beta = 0.69$ to $\beta = 0.93$.

This dramatic difference between the solution found using the “standard” plug flow assumption and the improved model presented in this communication is perhaps the best argument for the standard use of this improved model, particularly at scales outside of typical engineering practice.

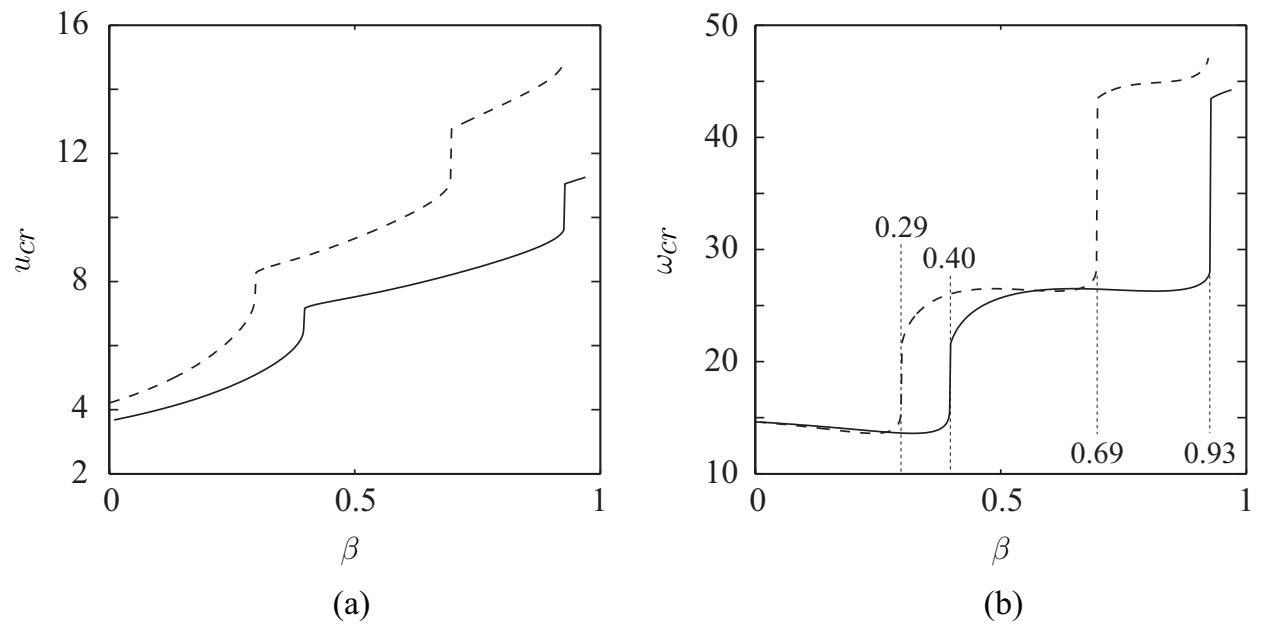


Figure 2.10: Plot of (a) u_{cr} and (b) ω_{cr} for uniform (thin line) and laminar (thick line) flow for different values of β .

Chapter 3

Simplified Dynamics of a Fluid-Conveying, Fluid-Immersed Pipe Affixed to a Rigid Body

3.1 Introduction

In the 1970s, Paidoussis and coworkers built and tested [28] a propulsor consisting of a fluid-conveying pipe affixed to the underside of a large surface hull. That work has limited theoretical justification, but the superficial similarity between a fluttering fluid-conveying cantilever and a fish is readily apparent — both motions take the form of a traveling wave which grows in amplitude from tip to tail. It is therefore easy to appreciate that the well-documented efficiency of fish-like motion [14, 25] was the motivation for this type of mechanism. Although the fluttering motion of the tail was found to be a net gain above the thrust provided by the jet exhausting into the water, the efficiency did not approach that of a propeller, and after

a patent [29], the idea appears to have been dropped.

Interim developments since these initial efforts justify a reexamination of the fluttering fluid-conveying tail as a propulsor. Improvements in battery and motor technologies now permit the prime mover and power source to be packaged into the neutrally buoyant hull of a small submersible, whereas Paidoussis' surface hull was very large relative to the propulsor. Reducing the size of the hull changes the system's dynamics, since the fluid-conveying tail may produce sufficient transverse force and moments to alter the motions of the hull. That is, the boundary conditions of the tail are likely to be significantly different than those of a cantilever. The rigid body boundary condition developed in this chapter and used in its investigations is a close linear approximation to the boundary condition acting on the base of a fluttering, fluid-conveying submersible's tail.

This chapter is organized as follows. Section 3.2 provides the background for the dynamic equations of fluid conveying, fluid immersed pipes and the mechanics of slender body swimming. Section 3.3 presents the rigid body boundary conditions and makes them non-dimensional. The analytical method used for solution is also describe in this section. Section 3.4 investigates the flow requirements for controlled flutter and calculations of thrust and efficiency of the waveforms produced by the fluttering tail.

3.2 Background

3.2.1 Fluid-conveying pipes

The equations of motion and boundary conditions for a cantilever pipe conveying fluid with constant velocity U_i , immersed in an inviscid fluid flowing with constant velocity U_e , and

ignoring gravitational, viscous, pressurization and tensile effects, are as follows [31]:

$$EI \frac{\partial^4 y}{\partial x^4} + (MU_i^2 + M_e U_e^2) \frac{\partial^2 y}{\partial x^2} + 2(MU_i + M_e U_e) \frac{\partial^2 y}{\partial x \partial t} + (m + M + M_e) \frac{\partial^2 y}{\partial t^2} = 0, \quad (3.1)$$

$$y(0, t) = 0, \quad \frac{\partial y}{\partial x}(0, t) = 0, \quad \frac{\partial^2 y}{\partial x^2}(L, t) = 0, \quad \frac{\partial^3 y}{\partial x^3}(L, t) = 0$$

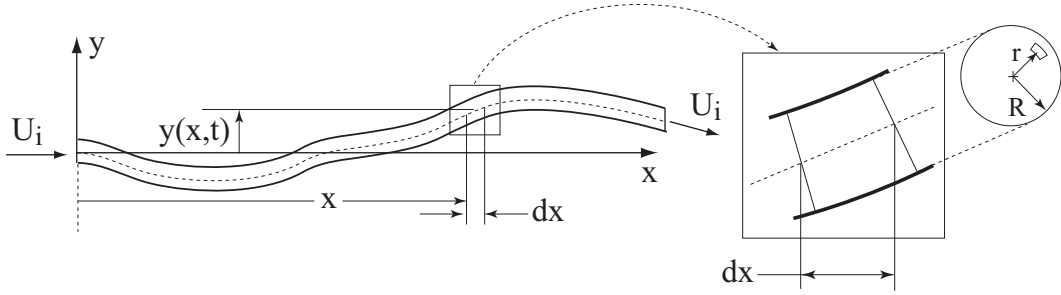


Figure 3.1: A cantilevered fluid-conveying pipe, with a magnified view of a small length element.

where $y(x, t)$ is the displacement of the pipe, as shown in Fig.3.1, E , I and L denote the Young's modulus, area moment of inertia, and length of the pipe, respectively, and m , M and M_e represent the mass per unit length of the beam, the internal (conveyed) fluid, and the external fluid. The masses per unit length of the beam and internal fluid can be easily computed but the mass per unit length of the external fluid requires approximation. One method for computation of M_e is to use the added mass coefficient [9]. For thin cross sections, such as that of a flat plate, the added mass is equal to the mass of water within the cylinder which circumscribes the plate cross-section. A “finned tube”, well suited to providing both a fluid conduit and a tail of adequate span, is depicted in Fig.3.2 with the area responsible for the added external mass marked. Viscous terms characteristic of the external flow [17] and internal flow [20] are of course needed to compute the overall efficiency of the submersible,

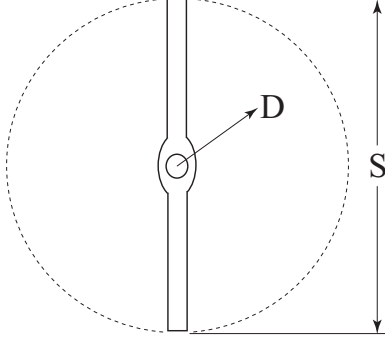


Figure 3.2: The cross-section of a finned tube with fluid-conduit diameter D and tail span S . The dotted circle describes the area responsible for the added external mass M_e , which is equal to $0.25\rho_f\pi S^2$, where ρ_f is the density of the external fluid.

and affect beam stability as well. These effects are neglected in this section to permit an analytical solution of the equations, and will be considered in the following section along with the additional accelerations and nonlinear rotations of the rigid body.

Equation (3.1) may be made non-dimensional via the following change of variables

$$X = \frac{x}{L}, \quad Y = \frac{y}{L}, \quad T = \frac{t}{L^2} \left(\frac{EI}{m + M + M_e} \right)^{1/2}. \quad (3.2)$$

The non-dimensional velocities u_i and u_e and the mass fractions β_i and β_e are defined as follows

$$\begin{aligned} u_i &= \left(\frac{M}{EI} \right)^{1/2} U_i L, & \beta_i &= \frac{M}{m + M + M_e}, \\ u_e &= \left(\frac{M_e}{EI} \right)^{1/2} U_e L, & \beta_e &= \frac{M_e}{m + M + M_e}, \end{aligned}$$

then Eq.(3.1) can be written in its non-dimensional form

$$\frac{\partial^4 Y}{\partial X^4} + (u_i^2 + u_e^2) \frac{\partial^2 Y}{\partial X^2} + 2(u_i \sqrt{\beta_i} + u_e \sqrt{\beta_e}) \frac{\partial^2 Y}{\partial X \partial T} + \frac{\partial^2 Y}{\partial T^2} = 0$$

A separable form for $y(x, t)$ is assumed, *i.e.*, $y(x, t) = f(x)e^{i\Omega t}$, such that the non-dimensional

variable Y takes the form

$$Y(X, T) = \phi(X)e^{i\omega t}, \quad \omega = \left(\frac{m + M + M_e}{EI} \right)^{1/2} \Omega L^2. \quad (3.3)$$

Separation yields the ordinary differential equation and boundary conditions

$$\frac{\partial^4 \phi}{\partial X^4} + (u_i^2 + u_e^2) \frac{\partial^2 \phi}{\partial X^2} + 2(u_i \sqrt{\beta_i} + u_e \sqrt{\beta_e}) i\omega \frac{\partial \phi}{\partial X} - \omega^2 \phi = 0, \quad (3.4)$$

$$\phi(0) = 0, \quad \frac{\partial \phi(0)}{\partial X} = 0, \quad \frac{\partial^2 \phi(1)}{\partial X^2} = 0, \quad \frac{\partial^3 \phi(1)}{\partial X^3} = 0,$$

The solution of ϕ is assumed to be of the form $\phi(X) = Ae^{zX}$. For specific values of u_i, u_e, β_i and β_e , the characteristic polynomial of Eq.(3.4) provides four roots z_n , where $z_n = z_n(\omega)$, $n = 1, 2, 3, 4$. The solution of $\phi(X)$ therefore takes the form

$$\phi(X) = A_1 e^{z_1 X} + A_2 e^{z_2 X} + A_3 e^{z_3 X} + A_4 e^{z_4 X}. \quad (3.5)$$

Substitution of Eq.3.5 into Eq.3.4 yields the identity

$$\underbrace{\begin{bmatrix} 1 & 1 & 1 & 1 \\ z_1 & z_2 & z_3 & z_4 \\ z_1^2 e^{z_1} & z_2^2 e^{z_2} & z_3^2 e^{z_3} & z_4^2 e^{z_4} \\ z_1^3 e^{z_1} & z_2^3 e^{z_2} & z_3^3 e^{z_3} & z_4^3 e^{z_4} \end{bmatrix}}_{\mathbf{Z}} \begin{bmatrix} A_1 \\ A_2 \\ A_3 \\ A_4 \end{bmatrix} = \begin{bmatrix} 0 \\ 0 \\ 0 \\ 0 \end{bmatrix}. \quad (3.6)$$

A non-trivial solution (for ω) of Eq.3.6 is obtained by numerical evaluation of the roots of $\text{Det}(\mathbf{Z}) = 0$. This equation has infinite roots in ω . Substitution of Eq.(3.5) into Eq.(3.3)

yields

$$Y(X, T) = \sum_{n=1}^4 A_n e^{z_n X} e^{i\omega T} = \sum_{n=1}^4 A_n \underbrace{e^{\Re[z_n]X}}_{(i)} \underbrace{e^{i(\Re[z_n]X + \Re[\omega]T)}}_{(ii)} \underbrace{e^{-\Re[\omega]T}}_{(iii)}. \quad (3.7)$$

It can be seen that $Y(X, T)$ is a product of three exponential terms of which the first term is bounded (since X is bounded), and the second term is periodic since the exponent is imaginary. The third term can grow unbounded with time if $\Re[\omega] < 0$ and this represents the onset of flutter instability. The mode and velocity at which the pipe becomes unstable depends on the fluid mass fractions β_i and β_e . The coefficients A_n , $n = 1, 2, 3, 4$, can be computed from the nullspace of the matrix \mathbf{Z} in Eq.3.6, once ω and z_n , $n = 1, 2, 3, 4$, have been determined. These coefficients are needed to estimate the force exerted by the fluid-conveying tube on the surrounding fluid.

3.2.2 Slender body swimming

Fish-like propulsion has been a topic of interest in the academic community for more than 60 years and several robotic platforms have been built [43, 27] to exploit the phenomenon. The mechanism proposed in this communication (see Fig.3.3) is composed of a fluttering fluid-conveying tail providing thrust by both jet and tail action; the tail has the cross-sectional profile of a finned tube like the one shown in Fig.3.2. A similar mechanism was constructed in the 1970s [28] and was found to produce positive thrust only if the phase velocity of the tail displacement was greater than the forward speed of the vessel.

Thrust production via a high phase velocity traveling wave was described first in a paper by Lighthill [23], which used slender body analysis to approximate the thrust produced by

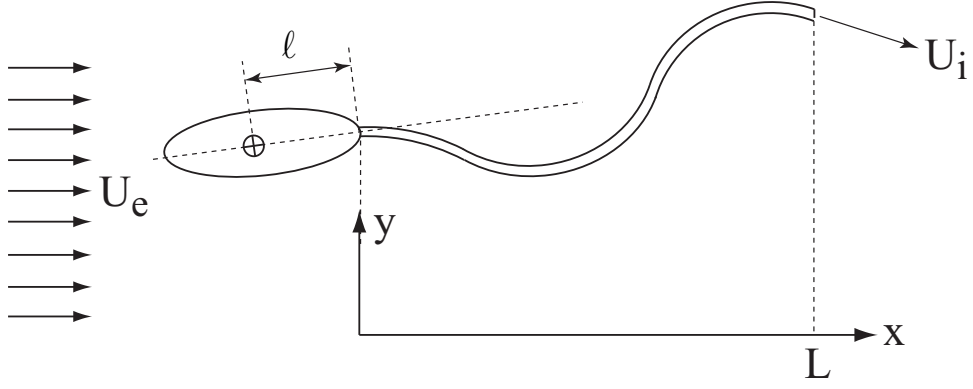


Figure 3.3: The proposed submersible, comprised of a rigid body and a fluid-conveying flexible tail. Note that the tail is assumed to have a finned-tube cross section, as shown in Fig.3.2.

an idealized fish. Lighthill found that a traveling waveform, for example

$$y(x, t) = f(x) \cos(kx + \Omega t) \quad (3.8)$$

can produce positive thrust if $(\Omega/k) > U_e$, where U_e is the speed of the body relative to the external fluid. The quantity Ω/k is known as the phase velocity. The following equation is the dimensional form of Eq.(3.7) for a single waveform

$$y_n(x, t) = A_n e^{\Re[Z_n]x} e^{i(\Re[Z_n]x + \Re[\Omega]t)} e^{-i\Re[\Omega]t}, \quad (3.9)$$

where Z_n and Ω are the dimensional wavenumber and frequency. The waveform described by Eq.(3.9) will result in positive thrust if

$$\frac{\Re[\Omega]}{\Re[Z_n]} > U_e.$$

The above equation can be made non-dimensional, taking the form

$$\frac{\Re[\omega]}{L^2} \left(\frac{EI}{m + M + M_e} \right)^{1/2} \frac{L}{\Re[z_n]} > u_e \left(\frac{EI}{M_e} \right)^{1/2} \frac{1}{L} \quad \Rightarrow \quad \frac{\Re[\omega]}{\Re[z_n]} > \frac{u_e}{\beta^{1/2}}. \quad (3.10)$$

Equation (3.10) gives us a condition under which a waveform will generate positive thrust, where $\Re[\omega]/\Re[z_n]$ is the non-dimensional phase velocity of the waveform.

Paidoussis' described his ichthyoid propulsor [28] as having a single phase velocity, which was measured by direct observation. While a single phase velocity is relatively simple to determine experimentally, determination of positive thrust is not straightforward in the context of Eq.(3.7) since it has four traveling waveforms of different, spatially variable amplitudes and phase velocities. In the context of Eq.(3.7), it is easier to estimate thrust by the method laid out by Lighthill [23] and Wu [44]. In those papers, a slender¹ fish is considered and the time-averaged thrust $\bar{\tau}$ is given by the relation

$$\bar{\tau} = \frac{1}{2} M_e \left[\overline{\left[\left(\frac{\partial y}{\partial t} \right)^2 - \left(U_e \frac{\partial y}{\partial x} \right)^2 \right]}_{x=L} - \overline{\left[\left(\frac{\partial y}{\partial t} \right)^2 - \left(U_e \frac{\partial y}{\partial x} \right)^2 \right]}_{x=0} \right], \quad (3.11)$$

where $y = y(x, t)$ denotes the displacement of the slender body from its neutral position, \dot{y} and y' denote partial derivatives of y with respect to time and x , and overbar refers to a long-term time average. In the above equation, increasing M_e increases the thrust generated; this leads to the design choice of the finned-tube in Fig.3.2. The form of Eq.(3.11) also makes it clear that a higher forward speed U_e requires a higher velocity \dot{y} to sustain it. Both Lighthill (Lighthill, 1960) and Wu (Wu, 1971) derived the expression in Eq.(3.11) without the assumption of harmonic motion. If harmonic motion is assumed, the time average over a

1: A definition of “slender body” can be found in §2 of Wu [44].

single cycle is sufficient. Note that Eq.(3.11) differs slightly from that found in (Wu, 1971)¹. Wu's assumption that no mass is affected at $x = 0$ is relaxed, since we have assumed that the tail has a geometry which is uniform along its length rather than a tapered fish which has zero area at the tip.

A similar expression (Lighthill, 1960) was derived for the average power \overline{P} required to provide the displacements $y(x, t)$

$$\overline{P} = U_e M_e \left[\left[\frac{\partial y}{\partial t} \left(\frac{\partial y}{\partial t} + U_e \frac{\partial y}{\partial x} \right) \right]_{x=L} - \left[\frac{\partial y}{\partial t} \left(\frac{\partial y}{\partial t} + U_e \frac{\partial y}{\partial x} \right) \right]_{x=0} \right], \quad (3.12)$$

which includes the power lost in the vortex wake. Equations (3.11) and (3.12) indicate that a large magnitude of \dot{y} produces greater thrust but also requires higher energy input. This can also be verified from the expression of the Froude efficiency (Lighthill, 1960) of the motion of the slender body

$$\eta = \frac{\overline{\tau} U_e}{\overline{P}}. \quad (3.13)$$

The expression for efficiency in Eq.(3.13) does not account for power lost to internal fluid shearing in the pipe, external drag, or the thrust produced by the fluid expelled from the fluid-conveying tail. The actual efficiency of the submersible will therefore be somewhat lower after these effects are accounted for.

1: Equation (47) in that work.

3.3 Fluid-conveying pipe affixed to a rigid body

3.3.1 Simplified boundary conditions

The complete planar dynamics of a submersible with a fluid-conveying fluttering tail, as shown in Fig.3.3, will be presented in the next chapter. However, a simplified model that permits better understanding of the important parameters governing the motion is desirable.

To this end, we make the following assumptions:

- A1. The rigid body is symmetric about the plane containing the neutral surface of the undeformed beam.
- A2. The rotation of the rigid body, denoted by θ in Fig.3.4, is small. This is in addition to the Euler-Bernoulli beam assumption that the slope of the tail is small everywhere along its length.
- A3. The submersible has zero acceleration in the x direction. This allows us to ignore the “forces” that arise from a non-inertial reference frame.
- A4. The added mass coefficient associated with the rigid body is zero. This assumption simplifies the analysis by allowing us to concentrate on the geometry of the rigid body in the xy plane. This is equivalent to the assumption that the rigid body is a planar lamina in the xy plane.

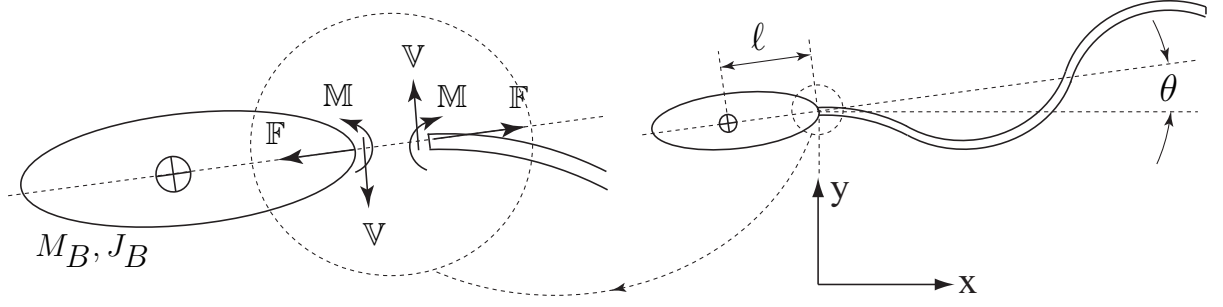


Figure 3.4: Free-body diagrams of the rigid body and tail of the submersible in Fig.3.3.

The above assumptions allow us to write the boundary conditions for the fluid-conveying tail¹ at $x = 0$ as follows:

$$\left[EI \frac{\partial^3 y}{\partial x^3} + M_B \left(\frac{\partial^2 y}{\partial t^2} - \ell \frac{\partial^3 y}{\partial x \partial t^2} \right) \right]_{x=0} = 0, \quad (3.14a)$$

$$\left[EI \frac{\partial^2 y}{\partial x^2} - (J_B + M_B \ell^2) \frac{\partial^3 y}{\partial x \partial t^2} + M_B \ell \frac{\partial^2 y}{\partial t^2} \right]_{x=0} = 0, \quad (3.14b)$$

where M_B is the mass of the rigid body, and J_B is the mass moment of inertia of the rigid body about its center of mass, and ℓ is the distance of the center of mass of the rigid body from the base of the tail. The boundary conditions in Eq.(3.14) can be derived from the free-body diagram of the rigid body in Fig.3.4 as follows

$$-\mathbb{V} = M_B \left[\frac{\partial^2 y}{\partial t^2} - \ell \frac{\partial^3 y}{\partial x \partial t^2} \right]_{x=0}, \quad \mathbb{M} - \ell \mathbb{V} = J_B \left[\frac{\partial^3 y}{\partial x \partial t^2} \right]_{x=0}.$$

It should be pointed out that the variable θ in Fig.3.4 denotes the orientation of the rigid body, which is equal to the slope of the tail at $x = 0$, *i.e.*, $\theta = [\partial y / \partial x]_{x=0}$. Since the rigid body is symmetric about the plane containing the neutral surface of the undeformed beam,

1: The result given here is similar to that in [8] with the exception that they have been derived here at $x = 0$ rather than $x = L$.

the force \mathbb{F} does not affect the boundary conditions.

Using Eq.(3.2), we can obtain the non-dimensional form of Eq.(3.14):

$$\left[\frac{\partial^3 Y}{\partial X^3} + \mu \left(\frac{\partial^2 Y}{\partial T^2} - \lambda \frac{\partial^3 Y}{\partial X \partial T^2} \right) \right]_{X=0} = 0, \quad (3.15a)$$

$$\left[\frac{\partial^2 Y}{\partial X^2} - \mu \left\{ (\psi_B + \lambda^2) \frac{\partial^3 Y}{\partial X \partial T^2} - \lambda \frac{\partial^2 Y}{\partial T^2} \right\} \right]_{X=0} = 0, \quad (3.15b)$$

where

$$\mu = \frac{M_B}{(m + M + M_e)L}, \quad \lambda = \frac{\ell}{L}, \quad \psi_B = \frac{J_B}{M_B L^2},$$

are non-dimensional parameters of the rigid body. Physically, μ is the ratio of its mass to the mass of the rest of the system, λ is a non-dimensional distance, and ψ_B is the square of the non-dimensional radius of gyration. Note that Eq.(3.15) provides the boundary conditions for a free end as $\mu \rightarrow 0$, and that of a clamped end as $\mu \rightarrow \infty$. The free-end conditions can be shown easily whereas the clamped-end conditions can be shown by allowing μ to approach ∞ in Eq.(3.15), which yields:

$$\left[\frac{\partial^2 Y}{\partial T^2} - \lambda \frac{\partial^3 Y}{\partial X \partial T^2} \right]_{X=0} = 0, \quad (3.16a)$$

$$\left[(\psi_B + \lambda^2) \frac{\partial^3 Y}{\partial X \partial T^2} - \lambda \frac{\partial^2 Y}{\partial T^2} \right]_{X=0} = 0. \quad (3.16b)$$

Since $\psi_B \neq 0$, it can be readily shown from the above that $\partial^2 Y / \partial T^2 = \partial^3 Y / \partial X \partial T^2 = 0$ at $X = 0$. Assuming zero initial velocities, *i.e.*, $\partial Y(0,0) / \partial T = \partial^2 Y(0,0) / \partial X \partial T = 0$, we obtain the clamped end conditions $\partial Y(0,T) / \partial T = \partial^2 Y(0,T) / \partial X \partial T = 0$.

3.3.2 Method of analysis

The simplified boundary conditions for a fluid-conveying pipe affixed to a rigid body are investigated in the same manner as that of a cantilever pipe, which was discussed in section 2.1. Using the boundary conditions in Eq.(3.15), we get the following relation that is similar to Eq.(3.6):

$$\begin{bmatrix} \eta_1 & \eta_2 & \eta_3 & \eta_4 \\ \zeta_1 & \zeta_2 & \zeta_3 & \zeta_4 \\ z_1^2 e^{z_1} & z_2^2 e^{z_2} & z_3^2 e^{z_3} & z_4^2 e^{z_4} \\ z_1^3 e^{z_1} & z_2^3 e^{z_2} & z_3^3 e^{z_3} & z_4^3 e^{z_4} \end{bmatrix} \begin{bmatrix} A_1 \\ A_2 \\ A_3 \\ A_4 \end{bmatrix} = \begin{bmatrix} 0 \\ 0 \\ 0 \\ 0 \end{bmatrix}, \quad (3.17)$$

where η_n , ζ_n , $n = 1, 2, 3, 4$, are defined by the relations

$$\begin{aligned} \eta_n &= z_n^2 + \mu\omega^2 \left[(\psi_B + \lambda^2)z_n - \lambda \right], \\ \zeta_n &= z_n^3 - \mu\omega^2(1 - \lambda z_n). \end{aligned}$$

Equation (3.17) leads to a solution of the form given by Eq.(3.7). Since the proposed application of the swimming submersible requires the oscillations of the fluttering tail not to grow with time, the points of neutral stability, *i.e.* $\Re[\omega] = 0$, are sought in the u_i - u_e space.

For a given μ , λ , ψ_B , β_i , β_e , and a given forward velocity u_e , the value of u_i for which $\Re[\omega] = 0$ can be found through analysis of an Argand diagram, an example of which is provided in Fig.3.5. This diagram is constructed [15] by determining the natural frequencies of a set of modes at $u_i = 0$, then gradually incrementing u_i to determine $\Re[\omega]$ and $\Im[\omega]$ for higher values of u_i . The natural frequencies at the onset of flutter instability, ω_{cr} , are the locations where the resultant curves cross the imaginary axis. The velocities at which

this occurs are referred to as critical velocities, u_{cr} . This procedure yields a single neutrally stable point in the u_i - u_e space. Clearly, while it is possible to search the entire u_i - u_e space for these neutrally stable points, this would require construction of a large number of Argand diagrams to obtain an acceptable resolution in u_e , which is prohibitively time-expensive. To mitigate this problem, an automated method similar in character to that discussed above is proposed.

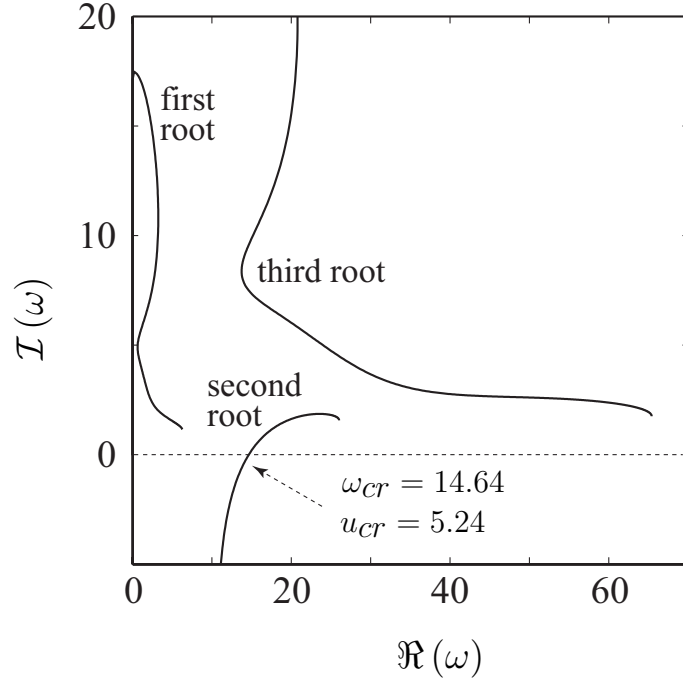


Figure 3.5: Argand diagram for the first three modes of oscillation for $\beta_i = 0.01$, $\beta_e = 0.9$, $\lambda = 1/2$, $\psi_B = 1/12$, $\mu = 2.25$ and $u_e = 1.0$.

In the automated method, the value of u_i required for neutral stability at $u_e = 0$ is first computed by interpolating values of u_i for which $\Re[\omega] \approx 0$. This is repeated once more for $u_e = \epsilon$, where ϵ is a small number. Subsequent points may be found in the following manner, which is explained with the help of Fig.3.6. For a set of two consecutive neutrally stable points already determined, such as the points marked 1 and 2 in Fig.3.6, the next point is guessed to exist at point $3'$ at a distance ϵ_1 from point 2 along the vector \vec{v} drawn from

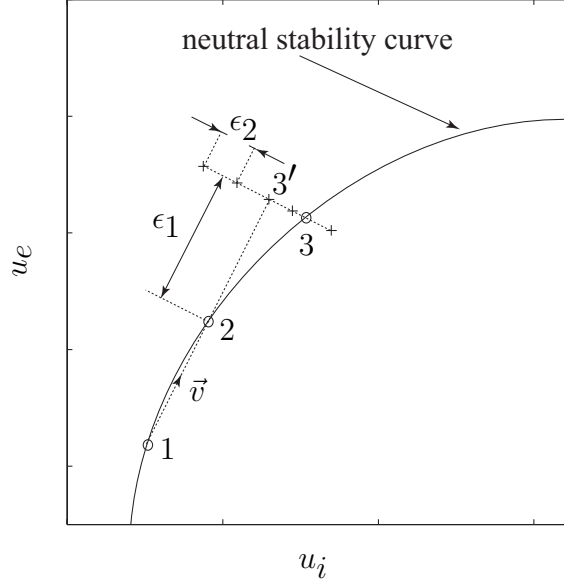


Figure 3.6: Illustration of the procedure used to find the neutral stability curve.

point 1 to point 2. Several points at which to compute ω are then chosen near point $3'$ along a vector perpendicular to \vec{v} . These points are separated from each other by the distance ϵ_2 . The value for ω_{cr} may now be found by interpolation, and computation of the critical values of u_i and u_e follows trivially. This procedure, in which the direction of iteration is nearly perpendicular to the curve, was necessary to navigate some of the sharp turns in the neutral stability curves given in the next section. In general, lower values of ϵ_1 and ϵ_2 are needed for curves with sharper turns, and in the current work, $\epsilon_1 = 0.02$, $\epsilon_2 = 0.002$ were found to suffice. The method was found to be robust as well; while we present results for a single rigid body of variable mass here, changes in other parameters can be easily accommodated.

3.4 Stability, thrust and efficiency

3.4.1 Neutral stability

We obtained neutral stability curves in the u_i - u_e space for a fluid-conveying pipe affixed to a rigid body, using the simplified boundary conditions discussed in the previous section. These neutral stability curves were obtained for various values of μ . The values of the other parameters were chosen as follows:

$$\beta_i = 0.01, \quad \beta_e = 0.9, \quad \lambda = 1/2, \quad \psi_B = 1/12.$$

The values of β_i and β_e used here reflect the finned-tube geometry, shown in Fig.3.2. The nature of this geometry is such that a large amount of external fluid is associated with the oscillations of the tail and this explains the relatively large value of β_e . Likewise, the small value of β_i reflects the small area through which internal fluid is conveyed. The values of λ and ψ_B correspond to a uniform cylinder with length equal to that of the tail.

The neutral stability curves are shown in Fig.3.7. The area inside each curve (towards the origin) represents the region where the tail does not flutter whereas the area outside represents the region where the tail flutters. The difference between the low- μ and high- μ curves is striking. For values of $u_e < 2.9$, the value of u_i required to create flutter decreases with increase in the value of μ . The confluence of all the curves at $u_e \approx 2.9$ is also interesting though no theoretical reason for this confluence is apparent. It should be mentioned that the curves' tendency to pass close to one another is not a unique scenario. Recall that the rigid body can be described by the parameters ψ_J , λ , and μ , of which we have only investigated the latter in detail in this work. Changing the values of ψ_J and λ does not, in our experience,

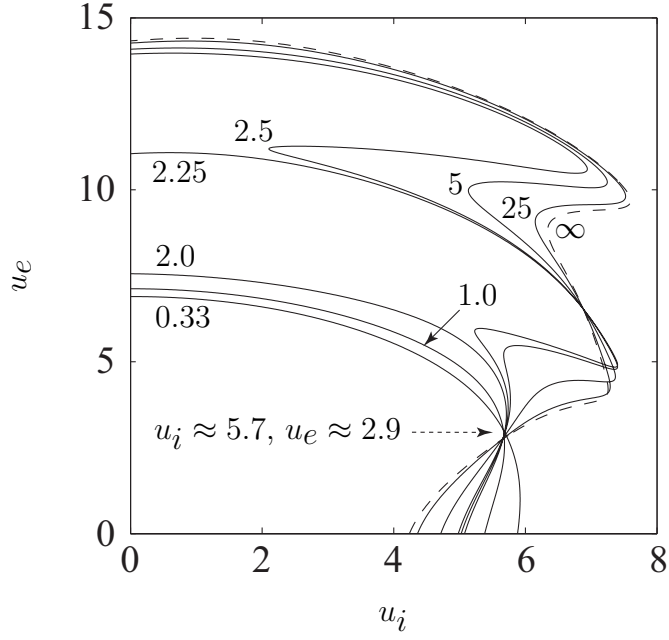


Figure 3.7: Neutral stability curves for different values of μ .

remove this tendency of the curves to intersect at a point, though the point in u_i - u_e space is different.

For values of $u_e > 2.9$, higher values of μ are neutrally stable at a higher value of u_e for a given value of u_i . This implies that for a given flow rate provided by the prime mover, a tail affixed to a hull of larger mass will tend to flutter at higher forward speed. The curves also indicate that higher values of μ are neutrally stable at a higher value of u_i for a given value of u_e . This implies that for a given external flow, a tail affixed to a hull of larger mass will require higher internal flow to flutter.

Figure 3.8 plots the relationship between u_e and ω_{cr} . It can be seen from this figure that for high mass ratios, there exist certain regions of the u_e parameter space where ω_{cr} is sensitive to u_e . This sensitivity may be used to determine a “sweet spot”, where a higher oscillation frequency may be obtained with a minimal change in u_e . This increase in oscillation frequency and concomitant increase in \dot{y} will increase the thrust produced by

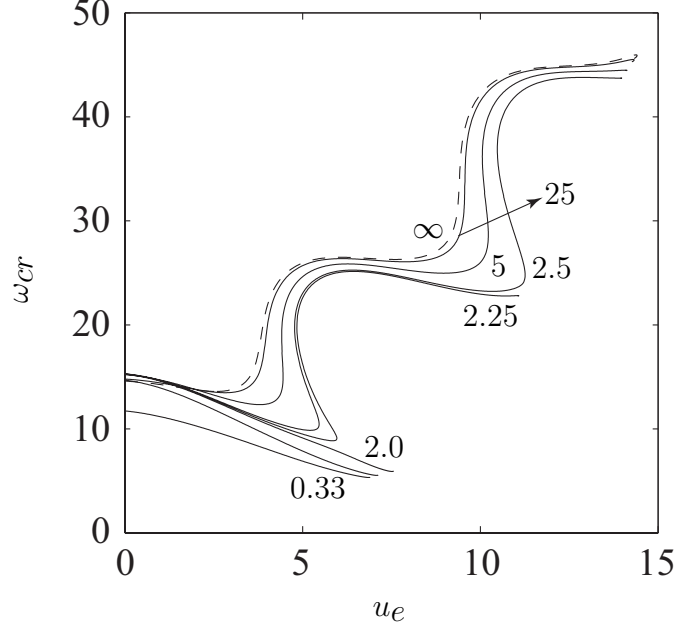


Figure 3.8: Plot showing the relationship between ω_{cr} and u_e for different values of μ .

the beam, per Eq.(3.11), and can be used for designing high-acceleration maneuvers for the submersible. Thrust production and efficiency in the context of Eqs.(3.11) and (3.12) is discussed in the next two sections.

3.4.2 Thrust characteristics

To determine the thrust produced by the fluttering tail of the proposed submersible, we non-dimensionalize Eq.(3.11) and compute the average over one cycle as follows:

$$\tau^* = \frac{\bar{\tau}L^2}{EI} = \frac{\omega_{cr}}{4\pi} \int_0^{2\pi/\omega_{cr}} \left\{ \left[\beta_e \dot{Y}^2 - u_e^2 Y'^2 \right]_{X=1} - \left[\beta_e \dot{Y}^2 - u_e^2 Y'^2 \right]_{X=0} \right\} dT. \quad (3.18)$$

The function $Y(X, T)$ is found by the method presented in section 2.1, and takes the form of Eq.(3.7). Equation (3.7) has both real and imaginary parts; only the real part is physically manifest and contributes to the thrust. Assuming neutral stability ($\Re[\omega] = 0$), the real part

of Eq.(3.7) is

$$Y(X, T) = \sum_{n=1}^4 e^{\Re[z_n]X} \left\{ \Re[A_n] \cos(\Re[z_n]X + \Re[\omega]T) - \Im[A_n] \sin(\Re[z_n]X + \Re[\omega]T) \right\}$$

The coefficients A_n in the above equation are found by computing the nullspace of the matrix in Eq.(3.17). The terms \dot{Y} and Y' in Eq.(3.18) can then be obtained through differentiation.

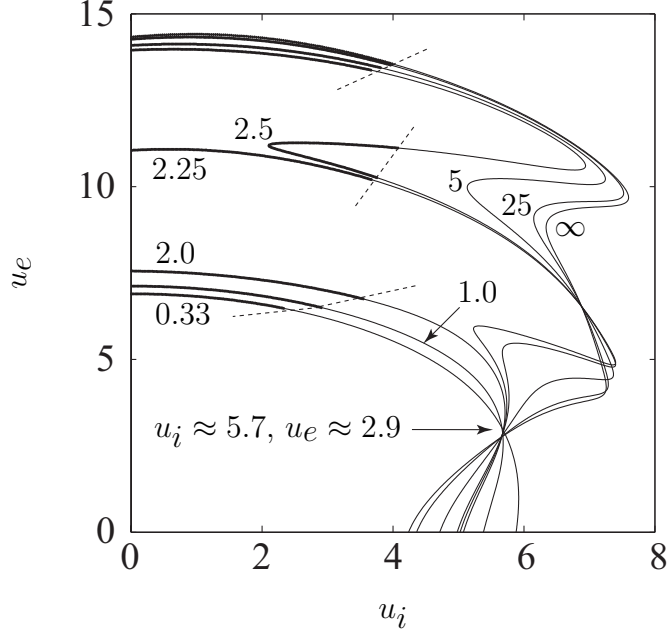


Figure 3.9: The darkened region of each neutral stability curve (left of the dotted lines) depicts the region of negative thrust.

Figure 3.9 reproduces the curves of neutral stability in Fig.3.7 with dark lines depicting the region on each curve where the thrust is negative. Notice that no value of μ allows thrust-producing flutter instability at $u_i = 0$. This matches with our physical intuition that a flapping flag cannot generate thrust. At low values of u_i , the positive hydrodynamic work is predominantly contributed by the external fluid and reduces the energy of that fluid; this phenomenon can be put to use in power generation [41]. It is also interesting to note that systems with lower values of μ can produce thrust at lower values of u_i than systems with

higher values of μ , though the high- μ systems have higher forward speed u_e .

It is important to remember, however, that merely having positive thrust from the tail does not guarantee that a given u_i - u_e point can be reached. The system's drag and the thrust of the fluid jet will also govern the submersible's top speed. Since the drag of the system will, for a neutrally-buoyant vessel, be strongly related to the displacement and mass, we will reserve these concerns for a later work more closely tied to the physical realization of the submersible.

Finally, it should be mentioned that the calculations presented here are purely concerned with the thrust produced by the traveling waveform in the fluttering tail. As such, the thrust produced by the fluid jet is not considered. However, it has been shown through experiments [28] that this loss of thrust can be overcome such that the combined jet and tail action produces a net thrust that is higher than that of a fixed jet.

3.4.3 Hydrodynamic efficiency

Similar to the expression for thrust, Eq.(3.12) can be made non-dimensional and the average over one cycle computed, to give the average non-dimensional power P^* :

$$P^* = \frac{\overline{P} M_e^{1/2} L^3}{(EI)^{3/2}} = \frac{\omega_{cr}}{2\pi} \int_0^{2\pi/\omega_{cr}} \left\{ \left[\beta_e u_e \dot{Y}^2 - u_e^2 \beta_e^{1/2} Y' \dot{Y} \right]_{X=1} - \left[\beta_e u_e \dot{Y}^2 - u_e^2 \beta_e^{1/2} Y' \dot{Y} \right]_{X=0} \right\} dT$$

From Eq.(3.13), the expression for Froude efficiency can be written as

$$\eta = \frac{\overline{\tau} U_e}{\overline{P}} = \frac{\tau^* u_e}{P^*}. \quad (3.19)$$

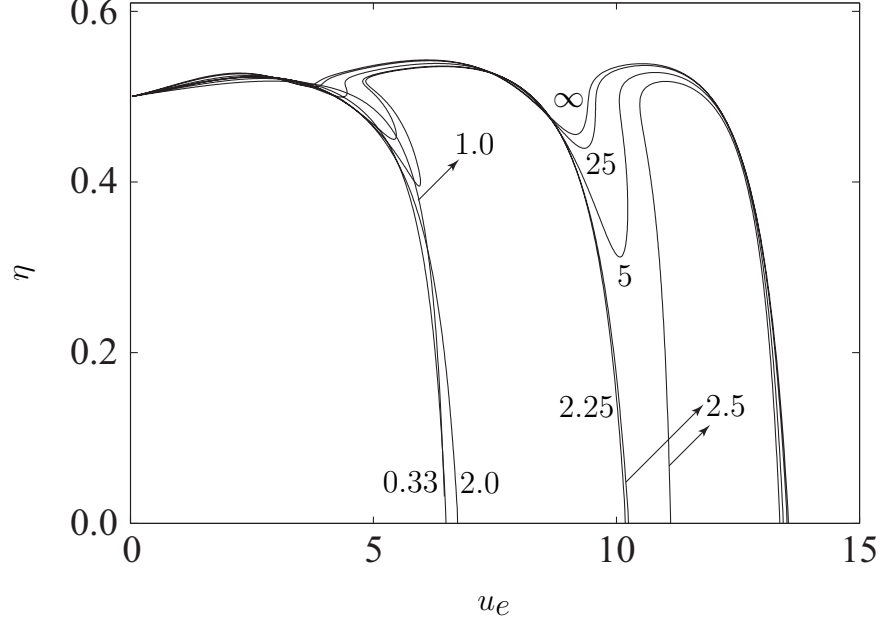


Figure 3.10: Efficiency for neutrally stable points in the u_i - u_e space and for different values of μ . Note that the curve for $\mu = 2.5$ is unique in that it has an interim region of zero efficiency.

Efficiencies computed using Eq.(3.19) are plotted with respect to u_e for various values of μ in Fig.3.10. Each curve plots the efficiency for neutrally stable points in the u_i - u_e space. Per the discussion in [44], Eq.(3.19) has meaning only when the thrust is positive, and therefore, Fig.3.10 plots the efficiency only for neutrally stable points with positive thrust, the non-darkened regions of Fig.3.9.

It is interesting to note that the maximum efficiency is insensitive to the value of μ . This will provide flexibility in submersible design since the mass of the hull can be chosen based on other factors such as power source, drag and buoyancy, rather than hydrodynamic efficiency. For each value of μ , the efficiency remains near its peak value for a wide range of u_e . This trend resembles the efficiency curves for tail-swimming fish which are known to maintain efficiency over a broad range of swimming speeds. Incidentally, this broad peak in efficiency is not characteristic of typical marine propellers, which tend to be most efficient

over a narrow range of velocities.

It should be mentioned that the values of efficiency cited here consider only the power used to generate tail motion in the external pressure field and the thrust provided by the tail. Other factors, such as pipe losses and viscous drag will affect the efficiency of the vehicle when considered as a whole. However, the thrust provided by the fluid jet has also not been considered; a full accounting of the system's efficiency would require further investigation.

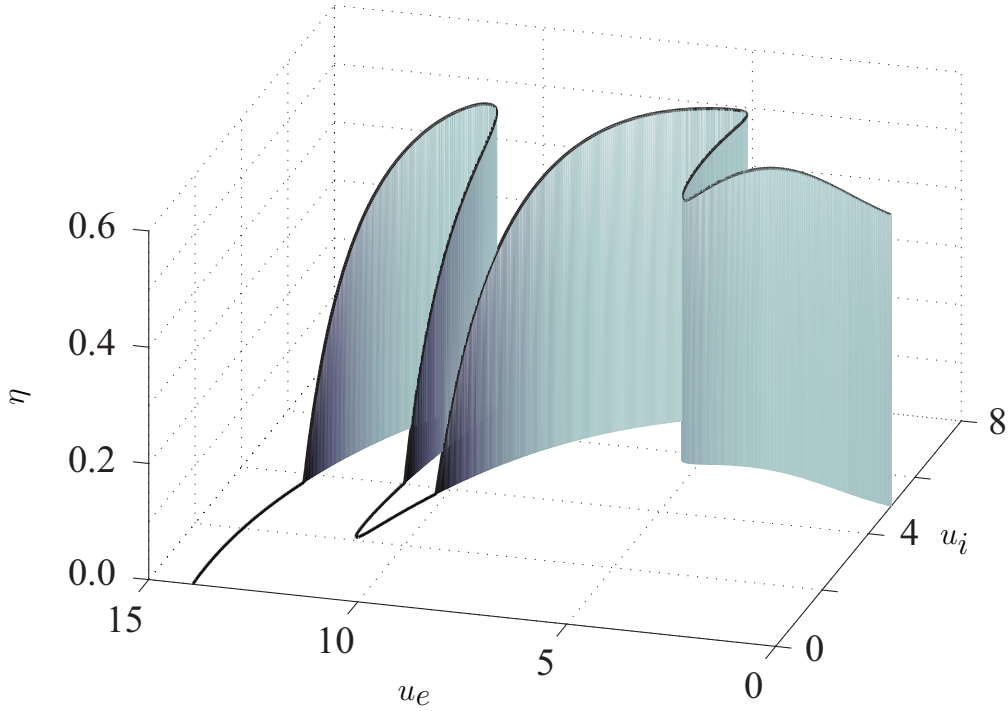


Figure 3.11: Efficiency as a function of u_i and u_e for the mass fraction $\mu = 2.5$.

A combined perspective on Figs.3.9 and 3.10 is presented in Fig.3.11, which depicts the neutral stability curve for $\mu = 2.5$ in three dimensions, with the efficiency shown out of the plane of the page. It is easy to see from this figure that the efficiency of tail motion for a propulsor of this type is dependent on both u_e and u_i . Since a value of zero on the above chart represents a net zero or negative thrust, it should be pointed out that high values of u_e require high values of u_i in order for the tail to oscillate with a thrust-generating waveform.

This result could be reasonably predicted; the limit case of a cantilever perturbed only by an axially flowing external fluid ($u_i = 0$) is not expected to add momentum in the axial direction to the surrounding fluid. Nonetheless, it is good to see this expectation confirmed by analysis.

Chapter 4

General Dynamics of a Fluid-Conveying, Fluid-Immersed Pipe Affixed to a Rigid Body

4.1 Nomenclature

A large number of symbols have been employed in this chapter. A nomenclature has therefore been provided for the reader's convenience.

h	Height of the flexible tail in the z direction, $[m]$
$\hat{i}, \hat{j}, \hat{k}$	Unit vectors along the x , y and z axes, respectively
$k_h^{xx}, k_h^{xy}, k_h^{yx}, k_h^{yy}$	Added mass coefficients associated with accelerations of the rigid head of the submersible in the x and y directions, $[-]$
$k_t^{xx}, k_t^{xy}, k_t^{yx}, k_t^{yy}$	Added mass coefficients associated with accelerations of the flexible tail of the submersible in the x and y directions, $[-]$

$k_h^{\theta\theta}, k_t^{\theta\theta}$	Added mass coefficients associated with angular acceleration of the rigid head and flexible tail of the submersible, $[-]$
m_h, m_t	Mass of the rigid head and flexible tail of the submersible, $[kg]$
m_i	Mass of the fluid within control volume Ω_i , $[kg]$
\hat{n}	The outward-pointing unit vector normal to a surface
\hat{n}_j	The outward-pointing unit vector normal to a control surface Γ_j
$p_2(x), p_4(x)$	Pressure in fluid control volumes Ω_2 and Ω_4 , $[N/m^2]$
q	Shear stress at the wall of the fluid-conveying tube $[N/m^2]$
\vec{r}	Position vector of a point in the xy reference frame, $[m]$
$\dot{\vec{r}}_{xy}$	Time derivative of \vec{r} as seen by an observer in the xy frame, $[m/s]$
$\ddot{\vec{r}}_{xy}$	Time derivative of $\dot{\vec{r}}_{xy}$ as seen by an observer in the xy frame, $[m/s^2]$
\vec{r}_c	Position vector of the center-of-mass of the system comprised of the submersible and fluid control volumes in the xy reference frame, $[m]$
r_{cx}, r_{cy}	x and y components of \vec{r}_c , $[m]$
$\dot{\vec{r}}_{cxy}$	Time derivative of \vec{r}_c as seen by an observer in the xy frame, $[m/s]$
$\dot{r}_{cx}, \dot{r}_{cy}$	x and y components of $\dot{\vec{r}}_{cxy}$, $[m/s]$
$\ddot{\vec{r}}_{cxy}$	Time derivative of $\dot{\vec{r}}_{cxy}$ as seen by an observer in the xy frame, $[m/s^2]$
$\ddot{r}_{cx}, \ddot{r}_{cy}$	x and y components of $\ddot{\vec{r}}_{cxy}$, $[m/s^2]$
xy -frame	Body-fixed reference frame as shown in Fig.4.1
\bar{x}, \bar{y}	x and y coordinates of the center-of-mass of control volume Ω , $[m]$
\bar{x}_h, \bar{y}_h	x and y coordinates of the center-of-mass of the rigid head of the submersible, $[m]$

\bar{x}_t, \bar{y}_t	x and y coordinates of the center-of-mass of the flexible tail of the submersible, $[m]$
\bar{x}_i, \bar{y}_i	x and y coordinates of the center-of-mass of the i -th fluid control volume, $[m]$
$y(x, t)$	Displacement of a point on the flexible tail at a distance of x from the origin of the xy -frame, $[m]$
y_L	$y(L, t)$, $[m]$
$\dot{y}(x, t)$	Time derivative of $y(x, t)$ as seen by an observer in the xy -frame, $[m/s]$
\dot{y}_L	$\dot{y}(L, t)$, $[m/s]$
$y'(x, t)$	First spatial derivative of $y(x, t)$
y'_L	$y'(L, t)$
A_j	Area of the control surface Γ_j , $[m^2]$
$\hat{I}, \hat{J}, \hat{K}$	Unit vectors along the X , Y and Z axes, respectively
\vec{F}_{ext}	External force acting on the submersible, $[N]$
\vec{F}_d	External force on the submersible per unit length due to drag, generated by fluid in the external control volumes, $[N/m]$
F_p	Pressure on the submersible due to non-ambient pressure at the entrance of the internal tube, $[N/m^2]$
F_I	Force magnitude per unit length normal to the wall of the fluid-conveying tube of the flexible tail due to internal flow, $[N/m]$
F_E	Force magnitude per unit length normal to the outer surface of the flexible tail due to external flow, $[N/m]$

J_z	Mass moment of inertia of control volume Ω about the z -axis passing through the origin of the xy -frame, $[kg.m^2]$
J_{zh}, J_{zt}	Mass moment of inertia of the rigid head and flexible tail of the submersible, respectively. Both are computed about the z -axis passing through the origin of the xy -frame, $[kg.m^2]$
J_{zi}	Mass moment of inertia of the i -th fluid control volume about the z -axis passing through the origin of the xy -frame, $[kg.m^2]$
L	Length of the flexible tail in the undeformed configuration, $[m]$
L_h	Length of the rigid head of the submersible along the x axis, $[m]$
M	Bending moment at a cross-section of the flexible tail, $[N.m]$
\vec{M}_{ext}	Moment of \vec{F}_{ext} about the origin of the inertial reference frame, $[N.m]$
P_h, P_t	Perimeters of the head and tail, $[m]$
Q	Shear force magnitude at a cross-section of the flexible tail, $[N]$
\vec{R}	Position vector of a point in the XY frame, $[m]$
\vec{R}_0	Position vector of the origin of the xy reference frame in the XY frame, $[m]$
R_{0x}, R_{0y}	x and y components of \vec{R}_0 , $[m]$
\vec{R}_c	Position vector of the center-of-mass of the system comprised of the submersible and fluid control volumes in the XY frame, $[m]$
S	Internal surface area per unit length of the fluid conveying tube within the flexible tail, $[m^2]$
T	Tension at a cross-section of the flexible tail, $[N]$

U	Speed of the fluid flowing through the flexible tail of the submersible, [m/s]
U_e	Speed of the external fluid in the x direction as seen by an observer in the xy -frame, [m/s]
U_h	Speed of the fluid flowing through the rigid head of the submersible, [m/s]
\vec{V}	Velocity of a particle in the XY reference frame, [m/s]
\vec{V}_r	Velocity of a fluid particle relative to a control surface, [m/s]
\vec{V}_s	Velocity of a point on a control surface, [m/s]
XY -frame	Inertial reference frame as shown in Fig.4.1
X_0, Y_0	X and Y components of \vec{R}_0 , [m]
ρ	Volumetric density, [kg/m ³]
ρ_h, ρ_t	Volumetric density of the rigid head and flexible tail of the submersible, [kg/m ³]
ρ_f	Volumetric density of the fluid, [kg/m ³]
θ	orientation of xy reference frame with respect to the XY frame, [rad]
Γ	Surface, [m ²]
Γ_j	j -th control surface, [m ²]
Ω	Volume, [m ³]
Ω_h, Ω_t	Control volume of the rigid head and flexible tail of the submersible, [m ³]
Ω_i	i -th fluid control volume, [m ³]

4.2 Introduction

In this chapter, we derive and solve the equations of motion for a submersible propelled by a fluttering fluid-conveying tail while relaxing some of the assumptions imposed in the previous chapter. In the previous chapter, it was assumed the rotations and transverse accelerations of the rigid body were small, meaning that the equation of motion of the fluid-conveying flexible tail could be stated within an inertial reference frame. In this more general formulation, the submersible is assumed to have distinctly non-zero acceleration and rotation, which makes it more convenient to write the equations of motion in a non-inertial frame of reference. Note that the equation of motion for a fluid-conveying pipe in a non-inertial frame has yet to appear in the literature as of this writing.

It is perhaps interesting that the equation of motion for a fluid-conveying pipe in a non-inertial frame appears here for the first time, given that an earlier attempt at this type of propulsor was made by Paidoussis and coworkers in the mid-1970's [28, 29]¹. There are two likely reasons for this. First, those works are primarily experimental in nature and provide very little in the way of theory to begin with; as will be shown in this chapter, the equations of motion in a non-inertial frame are not trivial, and do not lend themselves to being “thrown in” to an experimental work. Also, while no dimensions have been published for the surface ship-type hull described by [28], the figures provided in that work and the related patent [29] imply that the hull is large relative to the tail. A sufficiently large hull is of course insensitive to the time-dependent transverse loads and moments imposed by a fluttering tail, and the testing method employed in those works was not sensitive to the transient in forward acceleration.

1: An earlier cited work is an undergraduate thesis [36], which is difficult to find.

This chapter is organized as follows. Section 4.3 states the assumptions made for derivation of the equations of motion of the fluid-conveying flexible tail submersible. In section 4.4, the derivation method is laid out, and the terms for the momentum and external forces are described for the various components of the submersible. Section 4.5 describes the equations of motion of a fluid-conveying tail or pipe within a non-inertial reference frame. The simulation procedure used to solve the equations presented in sections 4.4 and 4.5 is presented in section 4.6, along with the results of those simulations.

This chapter makes use of many variable names, only some of which will be recognizable from prior sections - a nomenclature for this chapter is therefore provided in Appendix A.

4.3 Assumptions

Consider the fluid-conveying submersible shown in Fig.4.1. It is propelled by the combined action of a fluid jet exiting from its flexible tail and the fluttering action of the tail. XY denotes the inertial reference frame, xy is a body-fixed reference frame, and θ is the orientation of the xy frame with respect to the inertial frame. The equations of motion of the submersible are derived using the following simplifying assumptions:

- A1. The submersible is comprised of a head, which is a rigid body, and a flexible tail clamped to the head. The submersible is neutrally buoyant and its motion is confined to the XY plane. The xy -frame is fixed to the head at the base of the tail such that the neutral axis of the undeformed tail is congruent with the x -axis. The head is symmetric with respect to the xz and xy planes and is uniform along its length. In its undeformed configuration, the flexible tail has a rectangular projection in the xz plane. A corollary to this assumption is that both the head and tail have three planes

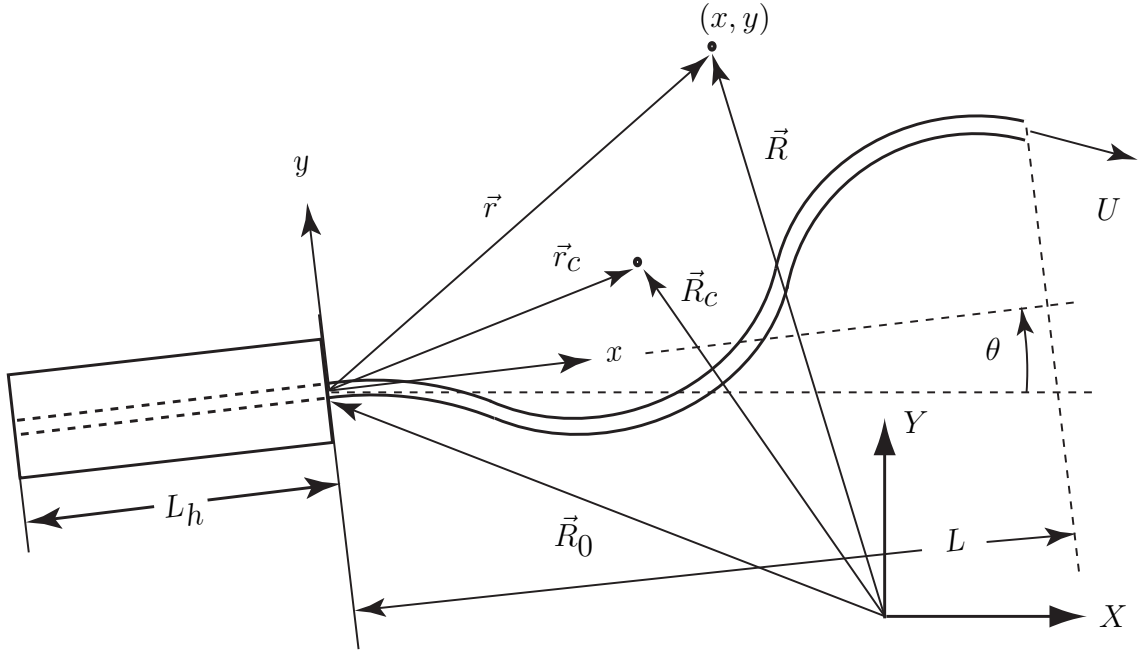


Figure 4.1: A submersible with a fluid-conveying flexible tail. The submersible is propelled by the combined action of the fluid jet and fluttering tail. In this figure, the deflection of the tail has been exaggerated.

of symmetry. The projection of the head and the undeformed tail in the xy plane is slender.

- A2. An internal cylindrical fluid-conveying tube runs along the length of the rigid head and the flexible tail. The axis of the cylindrical tube is congruent with the neutral axis of the flexible tail and with the x -axis along the length of the head.
- A3. The flexible tail behaves like an Euler-Bernoulli beam. This implies that all points along the length of the tail move in the y direction only, *i.e.*, without foreshortening. Furthermore, the displacement and slope of the tail with respect to the x -axis are small.
- A4. The flow in the internal cylindrical tube is steady and has a uniform tube-axial velocity profile. Secondary flows resulting from the curvature of the tube have been neglected.

- A5. The fluid conveyed through the internal cylindrical tube is the same as the fluid surrounding the submersible. The submersible is far from any free or solid surfaces.

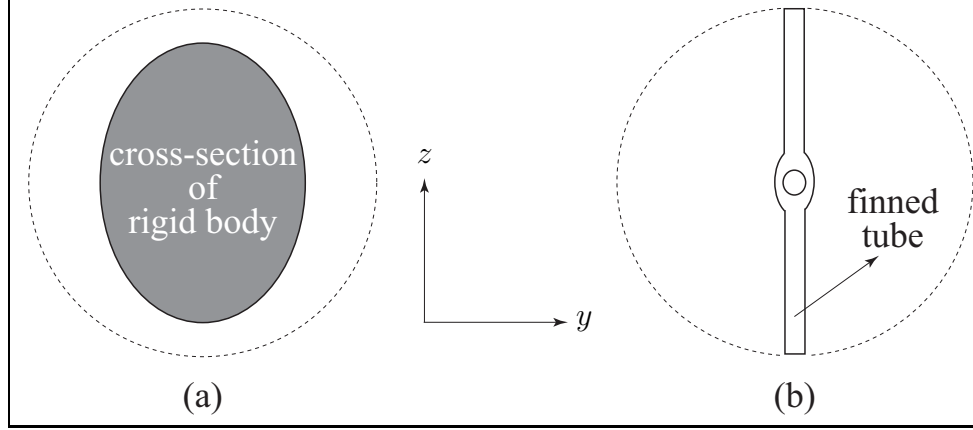


Figure 4.2: The cross-section of (a) the rigid head of the submersible at some point along its length, and (b) the flexible tail of the submersible, which is a finned tube. In both figures, the dotted circle describes the area responsible for the added fluid mass in the y direction.

The following assumptions are made in regards to the external fluid:

- A6. *Geometry*: The fluid control volumes around the head and tail of the submersible, which are defined in the next section, have identical motion as that of the submersible. The control volume around the head has identical axes of symmetry as those of the head. The control volume around the tail is symmetric about the neutral axis of the tail.
- A7. *Inertial Effects*: Each of the external control volumes contain the fluid associated with “added mass” [9]; note that the added-mass volumes may be different for the x , y and θ coordinates. A cross-section of the added mass volume for the y coordinate is shown in Fig.4.2 for both the rigid head and the flexible tail. The fluid within these volumes is inviscid.

- A8. *Drag Effects:* The “drag force” experienced by the head and tail of the submersible is reflected within the surrounding control volumes of fluid as a momentum deficit within that fluid. Instead of approximating this momentum deficit, the drag force on the body will be computed directly, via separate analysis.
- A9. *Inlet Pressure:* There is a non-ambient pressure at the entrance of the internal tube which results from drawing surrounding fluid into the head of the submersible. This pressure will be computed via analysis of the captured streamtube.

The internal fluid affects the dynamics of the submersible in the following way:

- A10. *Inertial Effects:* The fluid control volumes inside the head and tail of the submersible are subjected to the same acceleration as that of the head and tail of the submersible, respectively.

4.4 Dynamic Model - Newtonian Formulation

4.4.1 Force and Moment Equations

The equations of motion of the submersible are derived using the standard control volume approach. The fluid control volumes in and around the rigid head and flexible tail of the submersible are shown in Fig.4.3 along with their control surfaces. The names of the control volumes and control surfaces are listed in Table 4.1. The equations presented in this section are concerned with the motion of the xy -frame assuming a general function $y(x, t)$ for the motion of the tail. The tail’s dynamics are developed separately in a later section. The

translational motion of the xy -frame can be obtained from Newton's second law of motion

$$\vec{F}_{\text{fluid}} = \frac{d}{dt} \int_{\Omega_h(t)} \rho_h \vec{V} d\Omega + \frac{d}{dt} \int_{\Omega_t} \rho_t \vec{V} d\Omega \quad (4.1)$$

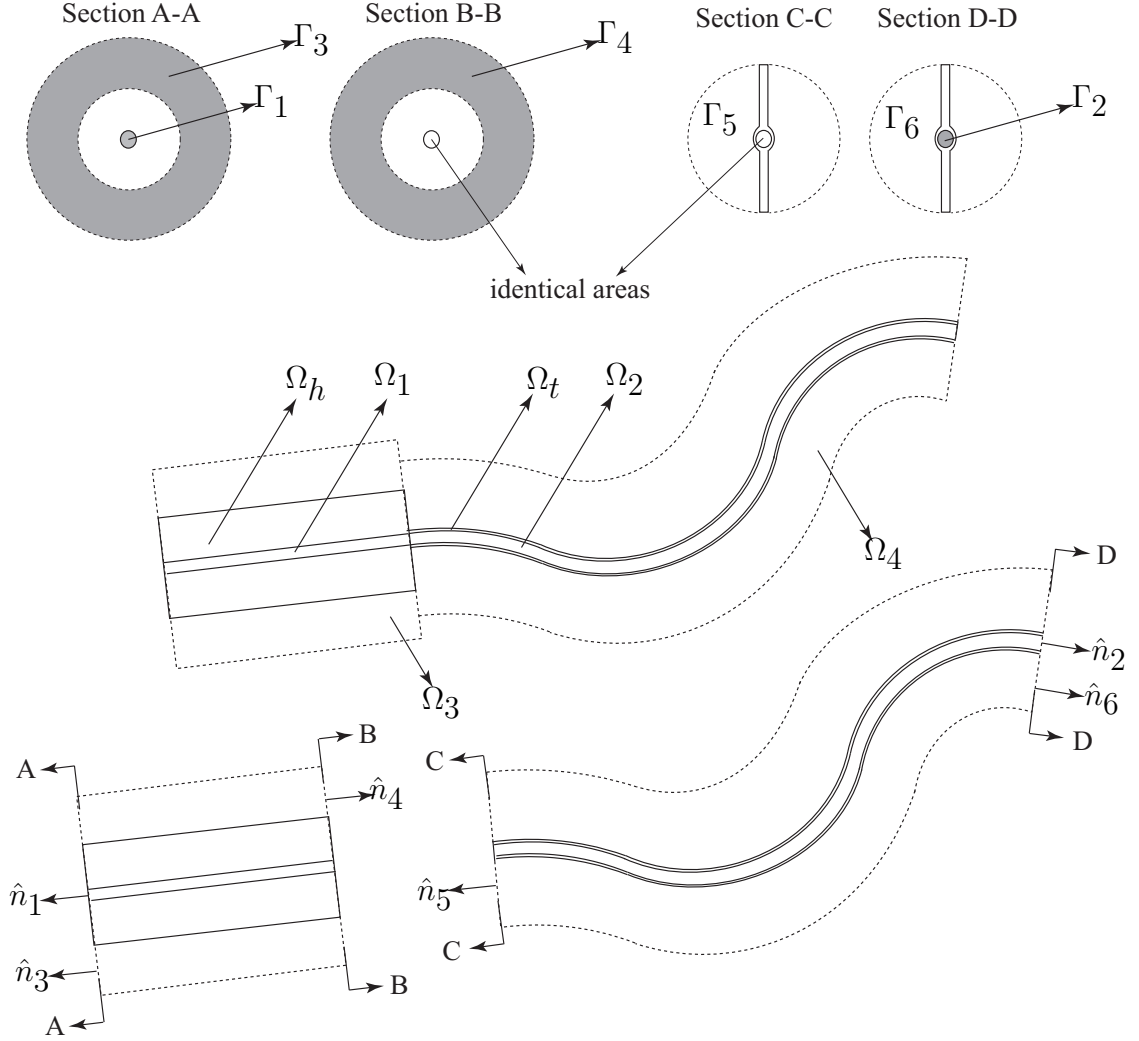


Figure 4.3: Depiction of control volumes Ω_h , Ω_t , and Ω_i , $i = 1, 2, 3, 4$; and control surfaces Γ_j , $j = 1, 2, 3, 4, 5, 6$, along with their outward normals.

The fluid forces on the left hand side of Eq.(4.1) are comprised of inertial forces associated with the fluid control volumes (assumptions A7 and A10), drag forces (assumption A8), and the force generated by the non-ambient pressure at the entrance of the internal tube

Table 4.1: Names of different fluid control volumes and control surfaces. Note that there is no need for a “head internal outlet” and “tail internal inlet”, since these surfaces are the same.

Control Volumes		Control Surfaces	
Ω_h	Rigid Head	Γ_1	Jet Inlet
Ω_t	Flexible Tail	Γ_2	Jet Outlet
Ω_1	Head Internal Fluid	Γ_3	External Flow Head Inlet
Ω_2	Tail Internal Fluid	Γ_4	External Flow Head Outlet
Ω_3	Head External Fluid	Γ_5	External Flow Tail Inlet
Ω_4	Tail External Fluid	Γ_6	External Flow Tail Outlet

(assumption A9). The inertial forces are comprised of volume and surface terms obtained from Reynolds’ transport theorem [33] and therefore the external forces can be written as

$$\begin{aligned}
\vec{F}_{\text{fluid}} = & - \sum_{i=1}^4 \left[\frac{d}{dt} \int_{\Omega_i(t)} \rho_f \vec{V} d\Omega \right] - \sum_{j=1}^6 \left[\int_{\Gamma_j(t)} \rho_f \vec{V} (\vec{V}_r \cdot \hat{n}_j) d\Gamma \right] \\
& + \int_{\Omega_h, \Omega_t} \vec{F}_d dx + \int_{\Gamma_1(t)} \vec{F}_p d\Gamma
\end{aligned} \tag{4.2}$$

Substitution of the above equation into Eq.(4.1) yields

$$\begin{aligned}
\int_{\Omega_h, \Omega_t} \vec{F}_d dx + \int_{\Gamma_1(t)} \vec{F}_p d\Gamma = & \frac{d}{dt} \left[\int_{\Omega_h(t)} \rho_h \vec{V} d\Omega + \int_{\Omega_t} \rho_t \vec{V} d\Omega + \sum_{i=1}^4 \int_{\Omega_i(t)} \rho_f \vec{V} d\Omega \right] \\
& + \sum_{j=1}^6 \left[\int_{\Gamma_j(t)} \rho_f \vec{V} (\vec{V}_r \cdot \hat{n}_j) d\Gamma \right]
\end{aligned} \tag{4.3}$$

The volume integral terms of Eq.(4.3) may be simplified using Liebniz’ rule, written in Eq.(4.4) for a general control volume $\Omega(t)$ with control surface $\Gamma(t)$. Note that Liebniz’ rule applies only to the volume integral term on the left-hand side of Eq.(4.4); the surface integral which arises from the application of Liebniz rule can be combined with the surface integral

since $\vec{V}_s + \vec{V}_r = \vec{V}$.

$$\begin{aligned}
& \frac{d}{dt} \int_{\Omega(t)} \rho \vec{V} d\Omega + \int_{\Gamma(t)} \rho \vec{V} (\vec{V}_r \cdot \hat{n}) d\Gamma \\
&= \int_{\Omega(t)} \frac{\partial}{\partial t} (\rho \vec{V}) d\Omega + \int_{\Gamma(t)} \rho \vec{V} (\vec{V}_s \cdot \hat{n}) d\Gamma + \int_{\Gamma(t)} \rho \vec{V} (\vec{V}_r \cdot \hat{n}) d\Gamma, \\
&= \int_{\Omega(t)} \frac{\partial}{\partial t} (\rho \vec{V}) d\Omega + \int_{\Gamma(t)} \rho \vec{V} (\vec{V} \cdot \hat{n}) d\Gamma
\end{aligned} \tag{4.4}$$

Using Liebniz' rule as written above, Eq.(4.3) can be rewritten as follows

$$\begin{aligned}
\int_{\Omega_h, \Omega_t} \vec{F}_d dx + \int_{\Gamma_1(t)} \vec{F}_p d\Gamma &= \int_{\Omega_h} \frac{\partial}{\partial t} (\rho_h \vec{V}) d\Omega + \int_{\Omega_t} \frac{\partial}{\partial t} (\rho_t \vec{V}) d\Omega + \sum_{i=1}^4 \int_{\Omega_i} \frac{\partial}{\partial t} (\rho_f \vec{V}) d\Omega \\
&+ \sum_{j=1}^4 \int_{\Gamma_j} \rho_f \vec{V} (\vec{V} \cdot \hat{n}_j) d\Gamma
\end{aligned} \tag{4.5}$$

An equation for the rotational motion of the submersible may be obtained by equating the sum of external moments about the inertial origin to the rate of change of angular momentum

$$\int_{\Omega_h, \Omega_t} \vec{M}_{\text{ext}} d\Omega = \frac{d}{dt} \int_{\Omega_h} [\vec{R} \times \rho_h \vec{V}] d\Omega + \frac{d}{dt} \int_{\Omega_t} [\vec{R} \times \rho_t \vec{V}] d\Omega \tag{4.6}$$

where $\vec{V} = \dot{\vec{R}}$. Similar to the external forces, the external moments on the left hand side of Eq.(4.6) are comprised of inertial moments, drag moments, and pressure moments. The inertial moments are comprised of volume and surface terms obtained from Reynolds' transport

theorem [33] and therefore the external moments can be written as

$$\begin{aligned} \int_{\Omega_h, \Omega_t} \vec{M}_{\text{ext}} d\Omega = & - \sum_{i=1}^4 \left[\frac{d}{dt} \int_{\Omega_i(t)} (\vec{R} \times \rho_f \vec{V}) d\Omega \right] - \sum_{j=1}^6 \left[\int_{\Gamma_j(t)} (\vec{R} \times \rho_f \vec{V}) (\vec{V}_r \cdot \hat{n}_j) d\Gamma \right] \\ & + \int_{\Omega_h, \Omega_t} \vec{R} \times \vec{F}_d dx + \int_{\Gamma_1(t)} \vec{R} \times \vec{F}_p d\Gamma \end{aligned}$$

where, as with Eq.(4.3), Liebniz' rule may be applied to move the time derivative inside the integral:

$$\begin{aligned} \int_{\Omega_h, \Omega_t} \vec{M}_{\text{ext}} d\Omega = & - \sum_{i=1}^4 \left[\int_{\Omega_i(t)} \frac{\partial}{\partial t} (\vec{R} \times \rho_f \vec{V}) d\Omega \right] - \sum_{j=1}^6 \left[\int_{\Gamma_j(t)} (\vec{R} \times \rho_f \vec{V}) (\vec{V} \cdot \hat{n}_j) d\Gamma \right] \\ & + \int_{\Omega_h, \Omega_t} \vec{R} \times \vec{F}_d dx + \int_{\Gamma_1(t)} \vec{R} \times \vec{F}_p d\Gamma \end{aligned} \quad (4.7)$$

Similar to the linear momentum equations, the equation above may be combined with Eqs.(4.6) to form:

$$\begin{aligned} \int_{\Omega_h, \Omega_t} \vec{R} \times \vec{F}_d dx + \int_{\Gamma_1(t)} \vec{R} \times \vec{F}_p d\Gamma = & \int_{\Omega_h} \vec{R} \times \frac{\partial}{\partial t} [\rho_h \vec{V}] d\Omega + \int_{\Omega_t} \vec{R} \times \frac{\partial}{\partial t} [\rho_t \vec{V}] d\Omega \\ & \sum_{i=1}^4 \left[\int_{\Omega_i(t)} \vec{R} \times \frac{\partial}{\partial t} [\rho_f \vec{V}] d\Omega \right] - \sum_{j=1}^6 \left[\int_{\Gamma_j(t)} (\vec{R} \times \rho_f \vec{V}) (\vec{V} \cdot \hat{n}_j) d\Gamma \right] \end{aligned} \quad (4.8)$$

using the simplification

$$\frac{\partial}{\partial t} (\vec{R} \times \rho \vec{V}) = \vec{R} \times \frac{\partial}{\partial t} (\rho \vec{V}) + \vec{V} \times \rho \vec{V} = \vec{R} \times \frac{\partial}{\partial t} (\rho \vec{V})$$

It is useful to rewrite Eq.(4.8) by taking moments and defining the angular momentum about the center of mass of the submersible and its attached control volumes. Using Eqs.(4.5) and

(4.8) yields the expressions

$$\begin{aligned}
& \int_{\Omega_h, \Omega_t} (\vec{R} - \vec{R}_c) \times \vec{F}_d dx + \int_{\Gamma_1(t)} (\vec{R} - \vec{R}_c) \times \vec{F}_p d\Gamma = \\
& \int_{\Omega_h} \frac{\partial}{\partial t} [(\vec{R} - \vec{R}_c) \times \rho_h \vec{V}] d\Omega + \int_{\Omega_t} \frac{\partial}{\partial t} [(\vec{R} - \vec{R}_c) \times \rho_t \vec{V}] d\Omega \\
& \sum_{i=1}^4 \left[\int_{\Omega_i(t)} \frac{\partial}{\partial t} [(\vec{R} - \vec{R}_c) \times \rho_f \vec{V}] d\Omega \right] + \sum_{j=1}^6 \left[\int_{\Gamma_j(t)} [(\vec{R} - \vec{R}_c) \times \rho_f \vec{V}] (\vec{V} \cdot \hat{n}_j) d\Gamma \right]
\end{aligned} \tag{4.9}$$

4.4.2 Added Mass

When a body is accelerated through a fluid, a volume of fluid surrounding the body is accelerated together with the body. The time rate of change of the momentum of this surrounding fluid results from a force to that fluid by the body, and an equal and opposite force is applied by that fluid to the body. This force is known as the added mass effect, and is modeled as the product of the acceleration of the body and a directionally dependent “added mass” related to the geometry of the body [9]. The directional dependence is reflected by rewriting the terms associated with external flow in Eqs.(4.5) and (4.9). Let $\vec{\alpha}_h$ and $\vec{\alpha}_t$ be defined as follows:

$$\begin{aligned}
\vec{\alpha}_h &= \int_{\Omega_3} \frac{\partial}{\partial t} (\rho_f \vec{V}) d\Omega + \int_{\Gamma_3, \Gamma_4} \rho_f \vec{V} (\vec{V} \cdot \hat{n}_j) d\Gamma \\
\vec{\alpha}_t &= \int_{\Omega_4} \frac{\partial}{\partial t} (\rho_f \vec{V}) d\Omega + \int_{\Gamma_{5,6}} \rho_f \vec{V} (\vec{V} \cdot \hat{n}_j) d\Gamma
\end{aligned}$$

The following replacements may now be made in Eq.(4.5):

$$\begin{aligned}
\text{Replace: } & \int_{\Omega_3} \frac{\partial}{\partial t} (\rho_f \vec{V}) d\Omega + \int_{\Gamma_3, \Gamma_4} \rho_f \vec{V} (\vec{V} \cdot \hat{n}_j) d\Gamma \\
\text{With: } & k_h^{xx} [\vec{\alpha}_h \cdot \hat{i}] \hat{i} + k_h^{xy} [\vec{\alpha}_h \cdot \hat{i}] \hat{j} + k_h^{yx} [\vec{\alpha}_h \cdot \hat{j}] \hat{i} + k_h^{yy} [\vec{\alpha}_h \cdot \hat{j}] \hat{j}
\end{aligned}$$

$$\begin{aligned}
\text{Replace: } & \int_{\Omega_4} \frac{\partial}{\partial t} (\rho_f \vec{V}) d\Omega + \int_{\Gamma_5, \Gamma_6} \rho_f \vec{V} (\vec{V} \cdot \hat{n}_j) d\Gamma \\
\text{With: } & k_t^{xx} [\vec{\alpha}_t \cdot \hat{i}] \hat{i} + k_t^{xy} [\vec{\alpha}_t \cdot \hat{i}] \hat{j} + k_t^{yx} [\vec{\alpha}_t \cdot \hat{j}] \hat{i} + k_t^{yy} [\vec{\alpha}_t \cdot \hat{j}] \hat{j}
\end{aligned}$$

where the coefficients k^{xx} and k^{xy} scale the momentum imparted to the external fluid in the x and y directions by acceleration in the x direction. Likewise, k^{yx} , and k^{yy} scale the momentum imparted to the external fluid in the x and y directions by accelerations in the y direction. The volume Ω_3 is equal in size to that of the head [9] and is assumed to surround the head with uniform thickness. The boundary of volume Ω_4 is a cylinder which circumscribes the finned tube tail [9]. As per assumption A1, both the head and tail have three planes of symmetry and assumption A7 states that the velocity field of the fluid surrounding the tail is adequately modeled by potential flow theory. Thus the replacements above simplify to [9]:

$$\begin{aligned}
\text{Replace: } & \int_{\Omega_3} \frac{\partial}{\partial t} (\rho_f \vec{V}) d\Omega + \int_{\Gamma_3, \Gamma_4} \rho_f \vec{V} (\vec{V} \cdot \hat{n}_j) d\Gamma \\
\text{With: } & k_h^{xx} [\vec{\alpha}_h \cdot \hat{i}] \hat{i} + k_h^{yy} [\vec{\alpha}_h \cdot \hat{j}] \hat{j}
\end{aligned} \tag{4.10}$$

$$\begin{aligned}
\text{Replace: } & \int_{\Omega_4} \frac{\partial}{\partial t} (\rho_f \vec{V}) d\Omega + \int_{\Gamma_5, \Gamma_6} \rho_f \vec{V} (\vec{V} \cdot \hat{n}_j) d\Gamma \\
\text{With: } & k_t^{xx} [\vec{\alpha}_t \cdot \hat{i}] \hat{i} + k_t^{yy} [\vec{\alpha}_t \cdot \hat{j}] \hat{j}
\end{aligned} \tag{4.11}$$

Using the substitutions in Eqs.(4.10) and (4.11), Eq.(4.5) can now be rewritten as follows

$$\begin{aligned}
& \int_{\Omega_h, \Omega_t} \vec{F}_d dx + \int_{\Gamma_1(t)} \vec{F}_p d\Gamma = \int_{\Omega_h} \rho_h \frac{\partial \vec{V}}{\partial t} d\Omega + \int_{\Omega_t} \rho_t \frac{\partial \vec{V}}{\partial t} d\Omega + \int_{\Omega_1, \Omega_2} \rho_f \frac{\partial \vec{V}}{\partial t} d\Omega \\
& + \int_{\Gamma_1, \Gamma_2} \rho_f \vec{V} [\vec{V} \cdot \hat{n}_j] d\Gamma + \left[\left(k_h^{xx} \int_{\Omega_3} \rho_f \frac{\partial \vec{V}}{\partial t} d\Omega + k_t^{xx} \int_{\Omega_4} \rho_f \frac{\partial \vec{V}}{\partial t} d\Omega \right) \cdot \hat{i} \right] \hat{i} \\
& + \left[\left(k_h^{yy} \int_{\Omega_3} \rho_f \frac{\partial \vec{V}}{\partial t} d\Omega + k_t^{yy} \int_{\Omega_4} \rho_f \frac{\partial \vec{V}}{\partial t} d\Omega \right) \cdot \hat{j} \right] \hat{j} \\
& + \left[\left(k_h^{xx} \int_{\Gamma_3, \Gamma_4} \rho_f \vec{V} [\vec{V} \cdot \hat{n}_j] d\Gamma + k_t^{xx} \int_{\Gamma_5, \Gamma_6} \rho_f \vec{V} [\vec{V} \cdot \hat{n}_j] d\Gamma \right) \cdot \hat{i} \right] \hat{i} \\
& + \left[\left(k_h^{yy} \int_{\Gamma_3, \Gamma_4} \rho_f \vec{V} [\vec{V} \cdot \hat{n}_j] d\Gamma + k_t^{yy} \int_{\Gamma_5, \Gamma_6} \rho_f \vec{V} [\vec{V} \cdot \hat{n}_j] d\Gamma \right) \cdot \hat{j} \right] \hat{j}
\end{aligned} \tag{4.12}$$

A replacement similar to Eqs.(4.10) and (4.11) can be performed on analogous terms in Eq.(4.9):

$$\begin{aligned}
\text{Replace: } & \int_{\Omega_3} \frac{\partial}{\partial t} [(\vec{R} - \vec{R}_c) \times \rho_f \vec{V}] d\Omega + \int_{\Gamma_3, \Gamma_4} (\vec{R} - \vec{R}_c) \times \rho_f \vec{V} (\vec{V} \cdot \hat{n}_j) d\Gamma \\
\text{With: } & k_h^{\theta\theta} \left(\int_{\Omega_3} \frac{\partial}{\partial t} [(\vec{R} - \vec{R}_c) \times \rho_f \vec{V}] d\Omega + \int_{\Gamma_3, \Gamma_4} (\vec{R} - \vec{R}_c) \times \rho_f \vec{V} (\vec{V} \cdot \hat{n}_j) d\Gamma \right)
\end{aligned} \tag{4.13}$$

$$\text{Replace: } \int_{\Omega_4} \frac{\partial}{\partial t} [(\vec{R} - \vec{R}_c) \times \rho_f \vec{V}] d\Omega + \int_{\Gamma_5, \Gamma_6} \rho_f \vec{V} (\vec{V} \cdot \hat{n}_j) d\Gamma \quad (4.14)$$

$$\text{With: } k_t^{\theta\theta} \left(\int_{\Omega_4} \frac{\partial}{\partial t} [(\vec{R} - \vec{R}_c) \times \rho_f \vec{V}] d\Omega + \int_{\Gamma_5, \Gamma_6} (\vec{R} - \vec{R}_c) \times \rho_f \vec{V} (\vec{V} \cdot \hat{n}_j) d\Gamma \right)$$

Using the substitutions in Eqs.(4.13) and (4.14) and replacing $(\vec{R} - \vec{R}_c)$ with $(\vec{r} - \vec{r}_c)$, which can be verified from Fig.4.1, Eq.(4.9) can now be rewritten as follows

$$\begin{aligned} & \int_{\Omega_h, \Omega_t} (\vec{r} - \vec{r}_c) \times \vec{F}_d dx + \int_{\Gamma_1(t)} (\vec{r} - \vec{r}_c) \times \vec{F}_p d\Gamma = \\ & \int_{\Omega_h} \frac{\partial}{\partial t} [(\vec{r} - \vec{r}_c) \times \rho_h \vec{V}] d\Omega + \int_{\Omega_t} \frac{\partial}{\partial t} [(\vec{r} - \vec{r}_c) \times \rho_t \vec{V}] d\Omega \\ & + \int_{\Omega_1, \Omega_2} \frac{\partial}{\partial t} [(\vec{r} - \vec{r}_c) \times \rho_f \vec{V}] d\Omega + \int_{\Gamma_1, \Gamma_2} [(\vec{r} - \vec{r}_c) \times \rho_f \vec{V}] (\vec{V} \cdot \hat{n}_j) d\Gamma \\ & + k_h^{\theta\theta} \int_{\Omega_3} \frac{\partial}{\partial t} [(\vec{r} - \vec{r}_c) \times \rho_f \vec{V}] d\Omega + k_t^{\theta\theta} \int_{\Omega_4} \frac{\partial}{\partial t} [(\vec{r} - \vec{r}_c) \times \rho_f \vec{V}] d\Omega \\ & + k_h^{\theta\theta} \int_{\Gamma_3, \Gamma_4} [(\vec{r} - \vec{r}_c) \times \rho_f \vec{V}] (\vec{V} \cdot \hat{n}_j) d\Gamma + k_t^{\theta\theta} \int_{\Gamma_5, \Gamma_6} [(\vec{r} - \vec{r}_c) \times \rho_f \vec{V}] (\vec{V} \cdot \hat{n}_j) d\Gamma \end{aligned} \quad (4.15)$$

To account for the effect of added mass, \vec{r}_c in the above equation is defined as follows:

$$\begin{aligned} \vec{r}_c &= r_{cx} \hat{i} + r_{cy} \hat{j}, \\ r_{cx} &= \frac{m_h \bar{x}_h + m_t \bar{x}_t + m_1 \bar{x}_1 + m_2 \bar{x}_2 + k_h^{\theta\theta} m_3 \bar{x}_3 + k_t^{\theta\theta} m_4 \bar{x}_4}{m_h + m_t + m_1 + m_2 + k_h^{\theta\theta} m_3 + k_t^{\theta\theta} m_4} \\ r_{cy} &= \frac{m_h \bar{y}_h + m_t \bar{y}_t + m_1 \bar{y}_1 + m_2 \bar{y}_2 + k_h^{\theta\theta} m_3 \bar{y}_3 + k_t^{\theta\theta} m_4 \bar{y}_4}{m_h + m_t + m_1 + m_2 + k_h^{\theta\theta} m_3 + k_t^{\theta\theta} m_4} \end{aligned} \quad (4.16)$$

where \bar{y}_h , \bar{y}_1 and \bar{y}_3 are zero due to Assumptions A1, A2 and A6.

4.4.3 Expansion of a General Volume Term

This section contains expansion of the volume terms in Eqs.(4.12) and (4.15), which are the force and moment equations, respectively. From Fig.4.1, the position, velocity and acceleration of an arbitrary particle is

$$\begin{aligned}\vec{R} &= \vec{R}_0 + \vec{r} & \vec{V} &= \dot{\vec{R}} = \dot{\vec{R}}_0 + \dot{\vec{r}}_{xy} + (\dot{\theta}\hat{k} \times \vec{r}) \\ \dot{\vec{V}} &= \ddot{\vec{R}} = \ddot{\vec{R}}_0 + \ddot{\vec{r}}_{xy} + (\ddot{\theta}\hat{k} \times \vec{r}) + (2\dot{\theta}\hat{k} \times \dot{\vec{r}}_{xy}) + (\dot{\theta}\hat{k} \times (\dot{\theta}\hat{k} \times \vec{r}))\end{aligned}\quad (4.17)$$

where the particle's velocity and acceleration have been obtained through differentiation. The volume terms in Eq.(4.12) are expanded via Eq.(4.17), and are integrated separately to give rise to physically intuitive terms:

$$\begin{aligned}\int_{\Omega} \rho \frac{\partial \vec{V}}{\partial t} d\Omega &= \int_{\Omega} \rho \left[\ddot{\vec{R}}_0 + \ddot{\vec{r}}_{xy} + (\ddot{\theta}\hat{k} \times \vec{r}) + (2\dot{\theta}\hat{k} \times \dot{\vec{r}}_{xy}) + (\dot{\theta}\hat{k} \times (\dot{\theta}\hat{k} \times \vec{r})) \right] d\Omega \\ &= \int_{\Omega} \rho (\ddot{\vec{R}}_0 + \ddot{\vec{r}}_{xy}) d\Omega + \ddot{\theta}\hat{k} \times \int_{\Omega} \rho \vec{r} d\Omega + 2\dot{\theta}\hat{k} \times \int_{\Omega} \rho \dot{\vec{r}}_{xy} d\Omega - \dot{\theta}^2 \int_{\Omega} \rho \vec{r} d\Omega \\ &= \int_{\Omega} \rho (\ddot{\vec{R}}_0 + \ddot{\vec{r}}_{xy}) d\Omega + m\ddot{\theta}(\bar{x}\hat{j} - \bar{y}\hat{i}) + 2\dot{\theta}\hat{k} \times \int_{\Omega} \rho \dot{\vec{r}}_{xy} d\Omega - m\dot{\theta}^2(\bar{x}\hat{i} + \bar{y}\hat{j})\end{aligned}\quad (4.18)$$

where

$$\int_{\Omega} \rho \vec{r} d\Omega = m(\bar{x}\hat{i} + \bar{y}\hat{j}) \quad (4.19)$$

The volume terms in Eq.(4.15) are likewise expanded via Eq.(4.17) and integrated to give

rise to the following terms

$$\begin{aligned}
\int_{\Omega} \frac{\partial}{\partial t} [(\vec{r} - \vec{r}_c) \times \rho \vec{V}] d\Omega &= \int_{\Omega} \frac{\partial}{\partial t} \left[(\vec{r} - \vec{r}_c) \times \rho \underbrace{(\dot{\vec{R}} - \dot{\vec{R}}_c)}_{=(\dot{\vec{r}} - \dot{\vec{r}}_c)} \right] d\Omega + \int_{\Omega} \frac{\partial}{\partial t} [(\vec{r} - \vec{r}_c) \times \rho \dot{\vec{R}}_c] d\Omega \\
&= \int_{\Omega} \left[(\vec{r} - \vec{r}_c) \times \rho \underbrace{(\ddot{\vec{R}} - \ddot{\vec{R}}_c)}_{=(\ddot{\vec{r}} - \ddot{\vec{r}}_c)} \right] d\Omega + \underbrace{\int_{\Omega} [(\vec{r} - \vec{r}_c) \times \rho \ddot{\vec{R}}_c] d\Omega}_{=0} + \underbrace{\int_{\Omega} [(\dot{\vec{r}} - \dot{\vec{r}}_c) \times \rho \dot{\vec{R}}_c] d\Omega}_{=0} \\
&= \int_{\Omega} (\vec{r} - \vec{r}_c) \times \rho \left[(\ddot{\vec{r}}_{xy} - \ddot{\vec{r}}_{cxy}) + \dot{\theta} \hat{k} \times (\vec{r} - \vec{r}_c) + 2\dot{\theta} \hat{k} \times (\ddot{\vec{r}}_{xy} - \ddot{\vec{r}}_{cxy}) \right. \\
&\quad \left. + \dot{\theta} \hat{k} \times (\dot{\theta} \hat{k} \times (\vec{r} - \vec{r}_c)) \right] d\Omega \\
&= \int_{\Omega} (\vec{r} - \vec{r}_c) \times \rho \ddot{\vec{r}}_{xy} d\Omega + \dot{\theta} \hat{k} \left[J_z - m(\bar{x}^2 + \bar{y}^2) \right] + 2\dot{\theta} \hat{k} \int_{\Omega} (\vec{r} - \vec{r}_c) \cdot \rho \dot{\vec{r}}_{xy} d\Omega \quad (4.20)
\end{aligned}$$

In the above equation, the following simplifications were employed:

$$\int_{\Omega} (\vec{r} - \vec{r}_c) \times \rho \ddot{\vec{r}}_{cxy} d\Omega = \int_{\Omega} \rho (\vec{r} - \vec{r}_c) d\Omega \times \ddot{\vec{r}}_{cxy} = 0$$

$$\int_{\Omega} [(\vec{r} - \vec{r}_c) \times \dot{\theta} \hat{k} \times \rho (\vec{r} - \vec{r}_c)] d\Omega = \dot{\theta} \hat{k} \int_{\Omega} \rho [(\vec{r} - \vec{r}_c) \cdot (\vec{r} - \vec{r}_c)] d\Omega = \dot{\theta} \hat{k} \left[J_z - m(\bar{x}^2 + \bar{y}^2) \right]$$

$$\begin{aligned}
&\int_{\Omega} (\vec{r} - \vec{r}_c) \times \rho \left[2\dot{\theta} \hat{k} \times (\dot{\vec{r}}_{xy} - \dot{\vec{r}}_{cxy}) \right] d\Omega \\
&= 2\dot{\theta} \hat{k} \int_{\Omega} \rho [(\vec{r} - \vec{r}_c) \cdot \dot{\vec{r}}_{xy}] d\Omega - 2\dot{\theta} \hat{k} \int_{\Omega} \rho [(\vec{r} - \vec{r}_c) \cdot \dot{\vec{r}}_{cxy}] d\Omega
\end{aligned}$$

$$\int_{\Omega} (\vec{r} - \vec{r}_c) \times \rho \left[\dot{\theta} \hat{k} \times (\dot{\theta} \hat{k} \times (\vec{r} - \vec{r}_c)) \right] d\Omega = 0$$

4.4.4 Individual Volume Terms

In this section, the expansions in Eqs.(4.18) and (4.20) were used to compute the volume terms in Eqs.(4.12) and (4.15). In particular, the integrals for the volumes Ω_h , Ω_t , and Ω_i , $i = 1, 2, 3, 4$ were evaluated.

4.4.4.1 Rigid Head: Ω_h

All the particles in the rigid head of the submersible are fixed with respect to the xy -frame and therefore

$$\ddot{\vec{r}}_{xy} = 0, \quad \bar{x} = \bar{x}_h, \quad \bar{y} = 0, \quad \dot{\vec{r}}_{xy} = 0, \quad J_z = J_{zh}$$

The volume terms in Eq.(4.12), expanded via Eq.(4.18), take the form

$$\int_{\Omega_h} \rho_h \frac{\partial \vec{V}}{\partial t} d\Omega = m_h \left[\ddot{\vec{R}}_0 + \ddot{\theta} \bar{x}_h \hat{j} - \dot{\theta}^2 \bar{x}_h \hat{i} \right] \quad (4.21)$$

The volume terms in Eq.(4.15), expanded via Eq.(4.20), take the form

$$\int_{\Omega_h} \frac{\partial}{\partial t} \left[(\vec{r} - \vec{r}_c) \times \rho_h \vec{V} \right] d\Omega = m_h \left[\ddot{\theta} \left(\frac{J_{zh}}{m_h} - \bar{x}_h^2 \right) \right] \hat{k} \quad (4.22)$$

4.4.4.2 Flexible Tail: Ω_t

For the particles in the flexible tail of the submersible, the following relations hold:

$$\ddot{\vec{r}}_{xy} = \ddot{y} \hat{j}, \quad \bar{x} = \bar{x}_t, \quad \bar{y} = \frac{1}{L} \int_0^L y dx, \quad \dot{\vec{r}}_{xy} = \dot{y} \hat{j}, \quad J_z = m_t \left(\frac{L^2}{3} + \frac{1}{L} \int_0^L y^2 dx \right)$$

The volume terms in Eq.(4.12), expanded via Eq.(4.18), take the form

$$\begin{aligned} \int_{\Omega_t} \rho_t \frac{\partial \vec{V}}{\partial t} d\Omega = m_t \left[\ddot{\vec{R}}_0 + \frac{1}{L} \int_0^L \ddot{y} dx \hat{j} + \ddot{\theta} \left(\bar{x}_t \hat{j} - \frac{1}{L} \int_0^L y dx \hat{i} \right) \right. \\ \left. - 2\dot{\theta} \frac{1}{L} \int_0^L \dot{y} dx \hat{i} - \dot{\theta}^2 \left(\bar{x}_t \hat{i} + \frac{1}{L} \int_0^L y dx \hat{j} \right) \right] \end{aligned} \quad (4.23)$$

The volume terms in Eq.(4.15), expanded via Eq.(4.20), take the form

$$\begin{aligned} \int_{\Omega_t} \frac{\partial}{\partial t} \left[(\vec{r} - \vec{r}_c) \times \rho_t \vec{V} \right] d\Omega = \\ m_t \left[\frac{1}{L} \int_0^L (x - r_{cx}) \ddot{y} dx + \ddot{\theta} \left(\frac{L^2}{3} + \frac{1}{L} \int_0^L y^2 dx - \bar{x}_t^2 - \left[\frac{1}{L} \int_0^L y dx \right]^2 \right) \right. \\ \left. + 2\dot{\theta} \frac{1}{L} \int_0^L (y - r_{cy}) \dot{y} dx \right] \hat{k} \end{aligned} \quad (4.24)$$

4.4.4.3 Head Internal Fluid: Ω_1

The fluid within the head flows with steady velocity U_h , per assumption A4. The conduit through which it flows is fixed within the head of the submersible, and therefore

$$\ddot{r}_{xy} = 0, \quad \bar{x} = \bar{x}_1, \quad \bar{y} = 0, \quad \dot{r}_{xy} = U_h \hat{i}, \quad J_z = m_1 \frac{L_h^2}{3}$$

The volume terms in Eq.(4.12), expanded via Eq.(4.18), take the form

$$\int_{\Omega_1} \rho_f \frac{\partial \vec{V}}{\partial t} d\Omega = m_1 \left[\ddot{\vec{R}}_0 + \ddot{\theta} \bar{x}_1 \hat{j} + 2\dot{\theta} U_h \hat{j} - \dot{\theta}^2 \bar{x}_1 \hat{i} \right] \quad (4.25)$$

The volume terms in Eq.(4.15), expanded via Eq.(4.20), take the form

$$\int_{\Omega_1} \frac{\partial}{\partial t} [(\vec{r} - \vec{r}_c) \times \rho_f \vec{V}] d\Omega = m_1 \left[\ddot{\theta} \left(\frac{L_h^2}{3} - \bar{x}_1^2 \right) dx + 2\dot{\theta} \frac{1}{L_h} \int_{-L_h}^0 (x - r_{cx}) U_h dx \right] \hat{k} \quad (4.26)$$

4.4.4.4 Tail Internal Fluid: Ω_2

For the particles in this control volume, the following relations hold:

$$\begin{aligned} \ddot{r}_{xy} &= (\ddot{y} + 2U\dot{y}' + U^2 y'') \hat{j}, & \bar{x} &= \bar{x}_2 & \bar{y} &= \frac{1}{L} \int_0^L y dx, \\ \dot{r}_{xy} &= U \hat{i} + (\dot{y} + Uy') \hat{j}, & J_z &= m_2 \left(\frac{L^2}{3} + \frac{1}{L} \int_0^L y^2 dx \right) \end{aligned}$$

The volume terms in Eq.(4.12), expanded via Eq.(4.18), take the form

$$\begin{aligned} \int_{\Omega_2} \rho_f \frac{\partial \vec{V}}{\partial t} d\Omega &= m_2 \left[\ddot{\vec{R}}_0 + \frac{1}{L} \int_0^L (\ddot{y} + 2U\dot{y}' + U^2 y'') dx \hat{j} + \ddot{\theta} \left(\bar{x}_2 \hat{j} - \frac{1}{L} \int_0^L y dx \hat{i} \right) \right. \\ &\quad \left. + 2\dot{\theta} \left(U \hat{j} - \frac{1}{L} \int_0^L [\dot{y} + Uy'] dx \hat{i} \right) - \dot{\theta}^2 \left(\bar{x}_2 \hat{i} + \frac{1}{L} \int_0^L y dx \hat{j} \right) \right] \quad (4.27) \end{aligned}$$

The volume terms in Eq.(4.15), expanded via Eq.(4.20), take the form

$$\begin{aligned} \int_{\Omega_2} \frac{\partial}{\partial t} [(\vec{r} - \vec{r}_c) \times \rho_f \vec{V}] d\Omega &= m_2 \left[\frac{1}{L} \int_0^L (x - r_{cx}) (\ddot{y} + 2U\dot{y}' + U^2 y'') dx \right. \\ &\quad \left. + \ddot{\theta} \left(\frac{L^2}{3} + \frac{1}{L} \int_0^L y^2 dx - \bar{x}_2^2 - \left[\frac{1}{L} \int_0^L y dx \right]^2 \right) \right. \\ &\quad \left. + 2\dot{\theta} \frac{1}{L} \int_0^L (x - r_{cx}) U + (y - r_{cy}) (\dot{y} + Uy') dx \right] \hat{k} \quad (4.28) \end{aligned}$$

4.4.4.5 Head External Fluid: Ω_3

The fluid in this control volume flows past the rigid head of the submersible with an unsteady velocity U_e . For particles in this control volume, the following relations therefore hold

$$\ddot{\vec{r}}_{xy} = \dot{U}_e \hat{i}, \quad \bar{x} = \bar{x}_3 \quad \bar{y} = 0, \quad \dot{\vec{r}}_{xy} = U_e \hat{i} \quad J_z = k_h^{\theta\theta} m_3 \frac{L_h^2}{3}$$

The volume terms in Eq.(4.12), expanded via Eq.(4.18), take the form

$$\begin{aligned} \int_{\Omega_3} \rho_f \left[k_h^{xx} \left(\frac{\partial \vec{V}}{\partial t} \cdot \hat{i} \right) \hat{i} + k_h^{yy} \left(\frac{\partial \vec{V}}{\partial t} \cdot \hat{j} \right) \hat{j} \right] d\Omega = \\ m_3 k_h^{xx} \left[\ddot{R}_{0x} + \dot{U}_e - \dot{\theta}^2 \bar{x}_3 \right] \hat{i} + m_3 k_h^{yy} \left[\ddot{R}_{0y} + \ddot{\theta} \bar{x}_3 + 2\dot{\theta} U_e \right] \hat{j} \end{aligned} \quad (4.29)$$

The volume terms in Eq.(4.15), expanded via Eq.(4.20), take the form

$$k_h^{\theta\theta} \int_{\Omega_3} \frac{\partial}{\partial t} \left[(\vec{r} - \vec{r}_c) \times \rho_f \vec{V} \right] d\Omega = m_3 k_h^{\theta\theta} \left[r_{cy} \dot{U}_e + \ddot{\theta} \left(\frac{L_h^2}{3} - \bar{x}_3^2 \right) + 2\dot{\theta}(x - r_{cx}) U_e \right] \hat{k} \quad (4.30)$$

4.4.4.6 Tail External Fluid: Ω_4

The fluid in this control volume flows past the flexible tail of the submersible with an unsteady velocity U_e . For particles in this control volume, the following relations therefore hold

$$\begin{aligned} \ddot{\vec{r}}_{xy} = \dot{U}_e \hat{i} + (\ddot{y} + 2U_e \dot{y}' + U_e^2 y'' + \dot{U}_e y') \hat{j}, \quad \bar{x} = \bar{x}_4, \quad \bar{y} = \frac{1}{L} \int_0^L y \, dx, \\ \dot{\vec{r}}_{xy} = U_e \hat{i} + (\dot{y} + U_e y') \hat{j}, \quad J_z = k_t^{\theta\theta} m_4 \left(\frac{L^2}{3} + \frac{1}{L} \int_0^L y^2 \, dx \right) \end{aligned}$$

The volume terms in Eq.(4.12), expanded via Eq.(4.18), take the form

$$\begin{aligned}
& \int_{\Omega_4} \rho_f \left[k_t^{xx} \left(\frac{\partial \vec{V}}{\partial t} \cdot \hat{i} \right) \hat{i} + k_t^{yy} \left(\frac{\partial \vec{V}}{\partial t} \cdot \hat{j} \right) \hat{j} \right] d\Omega = \\
& m_4 k_t^{xx} \left[\ddot{R}_{0x} + \dot{U}_e - \ddot{\theta} \frac{1}{L} \int_0^L y dx - 2\dot{\theta} \frac{1}{L} \int_0^L (\dot{y} + U_e y') dx - \dot{\theta}^2 \bar{x}_4 \right] \hat{i} + \\
& m_4 k_t^{yy} \left[\ddot{R}_{0y} + \frac{1}{L} \int_0^L (\ddot{y} + 2U_e \dot{y}' + U_e^2 y'' + \dot{U}_e y') dx + \ddot{\theta} \bar{x}_4 + 2\dot{\theta} U_e - \dot{\theta}^2 \frac{1}{L} \int_0^L y dx \right] \hat{j}
\end{aligned} \tag{4.31}$$

The volume terms in Eq.(4.15), expanded via Eq.(4.20), take the form

$$\begin{aligned}
& m_4 k_t^{\theta\theta} \int_{\Omega_4} \frac{\partial}{\partial t} \left[(\vec{r} - \vec{r}_c) \times \rho_f \vec{V} \right] d\Omega = \\
& m_4 k_t^{\theta\theta} \left[\frac{1}{L} \int_0^L \left\{ (x - r_{cx})(\ddot{y} + 2U_e \dot{y}' + U_e^2 y'' + \dot{U}_e y') - (y - r_{cy})\dot{U}_e \right\} dx + \right. \\
& \left. \ddot{\theta} \left(\frac{L^2}{3} + \frac{1}{L} \int_0^L y^2 dx - \bar{x}_4^2 - \left[\frac{1}{L} \int_0^L y dx \right]^2 \right) \right. \\
& \left. + 2\dot{\theta} \frac{1}{L} \int_0^L \left\{ (x - r_{cx})U_e + (y - r_{cy})(\dot{y} + U_e y') \right\} dx \right] \hat{k}
\end{aligned} \tag{4.32}$$

4.4.5 Individual Surface Terms

4.4.5.1 Jet Inlet: Γ_1

The jet inlet is located at the tip of the head as shown in Fig.4.3. At this location,

$$\begin{aligned}
\vec{r} &= -L_h \hat{i}, & \hat{n}_1 &= -\hat{i}, & \vec{V}_s &= \dot{\vec{R}}_0 + \dot{\theta} \hat{k} \times -L_h \hat{i}, & \vec{V}_r &= U_h \hat{i}, \\
\vec{V} &= (\vec{V}_s + \vec{V}_r) = \dot{\vec{R}}_0 + U_h \hat{i} - \dot{\theta} L_h \hat{j}, & \vec{V} \cdot \hat{n}_1 &= -\dot{R}_{0x} - U_h
\end{aligned}$$

The surface terms in Eq.(4.12) have the form

$$\int_{\Gamma_1} \rho_f \vec{V} [\vec{V} \cdot \hat{n}_1] d\Gamma = \rho_f A_1 \left(\dot{\vec{R}}_0 + U_h \hat{i} - \dot{\theta} L_h \hat{j} \right) (-\dot{R}_{0x} - U_h) \quad (4.33)$$

The surface terms in Eq.(4.15) have the form

$$\begin{aligned} \int_{\Gamma_1} (\vec{r} - \vec{r}_c) \times \left(\rho_f \vec{V} [\vec{V} \cdot \hat{n}_1] \right) d\Gamma = \\ \rho_f A_1 \left[(-L_h - r_{cx}) \dot{R}_{0y} + r_{cy} (\dot{R}_{0x} + U_h) + \dot{\theta} (L_h^2 + L_h r_{cx}) \right] [-\dot{R}_{0x} - U_h] \hat{k} \end{aligned} \quad (4.34)$$

4.4.5.2 Jet Outlet: Γ_2

At the outlet of the jet,

$$\begin{aligned} \vec{r} &= L \hat{i} + y(L) \hat{j}, \quad \hat{n}_2 \approx \hat{i} + y'(L) \hat{j}, \quad \vec{V}_s = \dot{\vec{R}}_0 + \dot{y}(L) \hat{j} + \dot{\theta} \hat{k} \times [L \hat{i} + y(L) \hat{j}], \\ \vec{V}_r &= U \hat{n}_2, \quad \vec{V} = (\vec{V}_s + \vec{V}_r) = \dot{\vec{R}}_0 + \dot{y}(L) \hat{j} + U \hat{i} + U y'(L) \hat{j} + \dot{\theta} [L \hat{j} - y(L) \hat{i}], \\ \vec{V} \cdot \hat{n}_2 &= [\dot{R}_{0x} + U - \dot{\theta} y(L)] + y'(L) [\dot{R}_{0y} + \dot{y}(L) + \dot{\theta} L + U y'(L)] \end{aligned}$$

The surface terms in Eq.(4.12) have the form

$$\begin{aligned} \int_{\Gamma_2} \rho_f \vec{V} [\vec{V} \cdot \hat{n}_2] d\Gamma = \\ \rho_f A_2 \left[\dot{\vec{R}}_0 + \dot{y}(L) \hat{j} + U \hat{i} + U y'(L) \hat{j} + \dot{\theta} \{ L \hat{j} - y(L) \hat{i} \} \right] \times \\ \left[\{ \dot{R}_{0x} + U - \dot{\theta} y(L) \} + y'(L) \{ \dot{R}_{0y} + \dot{y}(L) + \dot{\theta} L + U y'(L) \} \right] \end{aligned} \quad (4.35)$$

The surface terms in Eq.(4.15) have the form

$$\begin{aligned} \int_{\Gamma_2} (\vec{r} - \vec{r}_c) \times \left(\rho_f \vec{V} [\vec{V} \cdot \hat{n}_2] \right) d\Gamma = \rho_f A_2 \left[(L - r_{cx}) \{ \dot{R}_{0y} + \dot{y}(L) + \dot{\theta}L + Uy'(L) \} \right. \\ \left. - \{ y(L) - r_{cy} \} \{ \dot{R}_{0x} + U - \dot{\theta}y(L) \} + \dot{\theta} \left\{ L^2 + y^2(L) - Lr_{cx} - y(L)r_{cy} \right\} \right] \times \\ \left[\{ \dot{R}_{0x} + U - \dot{\theta}y(L) \} + y'(L) \{ \dot{R}_{0y} + \dot{y}(L) + \dot{\theta}L + Uy'(L) \} \right] \hat{k} \quad (4.36) \end{aligned}$$

4.4.5.3 External Flow Head Inlet: Γ_3

For this surface, shown in Fig.4.3,

$$\begin{aligned} \vec{r} = -L_h \hat{i}, \quad \hat{n}_3 = -\hat{i}, \quad \vec{V}_s = \dot{\vec{R}}_0 + \dot{\theta} \hat{k} \times -L_h \hat{i}, \quad \vec{V}_r = U_e \hat{i}, \\ \vec{V} = (\vec{V}_s + \vec{V}_r) = \dot{\vec{R}}_0 + U_e \hat{i} - \dot{\theta} L_h \hat{j}, \quad \vec{V} \cdot \hat{n}_3 = -\dot{R}_{0x} - U_e \end{aligned}$$

The surface terms in Eq.(4.12) have the form

$$\begin{aligned} \int_{\Gamma_3} \rho_f \left(k_h^{xx} \left[\vec{V} \cdot \hat{i} \right] \hat{i} + k_h^{yy} \left[\vec{V} \cdot \hat{j} \right] \hat{j} \right) [\vec{V} \cdot \hat{n}_3] d\Gamma = \\ \rho_f A_3 \left(k_h^{xx} \left\{ \dot{R}_{0x} + U_e \right\} \hat{i} + k_h^{yy} \left\{ \dot{R}_{0y} - \dot{\theta} L_h \right\} \hat{j} \right) [-\dot{R}_{0x} - U_e] \quad (4.37) \end{aligned}$$

The surface terms in Eq.(4.15) have the form

$$\begin{aligned} k_h^{\theta\theta} \int_{\Gamma_3} (\vec{r} - \vec{r}_c) \times \left(\rho_f \vec{V} [\vec{V} \cdot \hat{n}_3] \right) d\Gamma = \\ \rho_f A_3 k_h^{\theta\theta} \left(\{ -L_h - r_{cx} \} \dot{R}_{0y} + r_{cy} \left\{ \dot{R}_{0x} + U_e \right\} + \dot{\theta} \left\{ L_h^2 + L_h r_{cx} \right\} \right) [-\dot{R}_{0x} - U_e] \hat{k} \quad (4.38) \end{aligned}$$

4.4.5.4 External Flow Head Outlet: Γ_4

This surface, shown in Fig.4.3, is located at the base of the flexible tail. For this surface, the following relations hold:

$$\begin{aligned}\vec{r} &= 0, & \hat{n}_4 &= \hat{i}, & \vec{V}_s &= \dot{\vec{R}}_0, & \vec{V}_r &= U_e \hat{i}, \\ \vec{V} &= (\vec{V}_s + \vec{V}_r) = \dot{\vec{R}}_0 + U_e \hat{i}, & \vec{V} \cdot \hat{n}_4 &= \dot{R}_{0x} + U_e\end{aligned}$$

The surface terms in Eq.(4.12) have the form

$$\begin{aligned}& \int_{\Gamma_4} \rho_f \left(k_h^{xx} \left\{ \vec{V} \cdot \hat{i} \right\} \hat{i} + k_h^{yy} \left\{ \vec{V} \cdot \hat{j} \right\} \hat{j} \right) [\vec{V} \cdot \hat{n}_4] d\Gamma = \\ & \rho_f A_4 \left(k_h^{xx} \left\{ \dot{R}_{0x} + U_e \right\} \hat{i} + k_h^{yy} \dot{R}_{0y} \hat{j} \right) [\dot{R}_{0x} + U_e]\end{aligned}\tag{4.39}$$

The surface terms in Eq.(4.15) have the form

$$\begin{aligned}& k_h^{\theta\theta} \int_{\Gamma_4} (\vec{r} - \vec{r}_c) \times \left(\rho_f \vec{V} [\vec{V} \cdot \hat{n}_4] \right) d\Gamma = \\ & \rho_f A_4 k_h^{\theta\theta} \left(-r_{cx} \dot{R}_{0y} + r_{cy} \left\{ \dot{R}_{0x} + U_e \right\} \right) [\dot{R}_{0x} + U_e] \hat{k}\end{aligned}\tag{4.40}$$

4.4.5.5 External Flow Tail Inlet: Γ_5

This surface also lies at the base of the flexible tail. Although its normal \hat{n}_5 is opposite to that of Γ_4 , the net momentum flux through these surfaces is not zero, since their areas and

added mass coefficients are not equal. For this surface,

$$\begin{aligned}\vec{r} &= 0, & \hat{n}_5 &= -\hat{i}, & \vec{V}_s &= \dot{\vec{R}}_0, & \vec{V}_r &= U_e \hat{i}, \\ \vec{V} &= (\vec{V}_s + \vec{V}_r) = \dot{\vec{R}}_0 + U_e \hat{i}, & \vec{V} \cdot \hat{n}_5 &= -\dot{R}_{0x} - U_e\end{aligned}$$

The surface terms in Eq.(4.12) have the form

$$\begin{aligned}& \int_{\Gamma_5} \rho_f \left(k_t^{xx} \left\{ \vec{V} \cdot \hat{i} \right\} \hat{i} + k_t^{yy} \left\{ \vec{V} \cdot \hat{j} \right\} \hat{j} \right) [\vec{V} \cdot \hat{n}_5] d\Gamma = \\ & \rho_f A_5 \left(k_t^{xx} \left\{ \dot{R}_{0x} + U_e \right\} \hat{i} + k_t^{yy} \dot{R}_{0y} \hat{j} \right) [-\dot{R}_{0x} - U_e]\end{aligned}\tag{4.41}$$

The surface terms in Eq.(4.15) have the form

$$\begin{aligned}& k_t^{\theta\theta} \int_{\Gamma_5} (\vec{r} - \vec{r}_c) \times \left(\rho_f \vec{V} [\vec{V} \cdot \hat{n}_5] \right) d\Gamma = \\ & \rho_f A_5 k_t^{\theta\theta} \left(-r_{cx} \dot{R}_{0y} + r_{cy} \left\{ \dot{R}_{0x} + U_e \right\} \right) [-\dot{R}_{0x} - U_e] \hat{k}\end{aligned}\tag{4.42}$$

4.4.5.6 External Flow Tail Outlet: Γ_6

This surface lies at the tip of the tail and has the same normal as that of Γ_2 . For this surface,

$$\begin{aligned}\vec{r} &= L\hat{i} + y(L)\hat{j}, & \hat{n}_6 &\approx \hat{i} + y'(L)\hat{j}, & \vec{V}_s &= \dot{\vec{R}}_0 + \dot{y}(L)\hat{j} + \dot{\theta}\hat{k} \times L\hat{i}, \\ \vec{V}_r &= U_e \hat{n}_6, & \vec{V} &= (\vec{V}_s + \vec{V}_r) = \dot{\vec{R}}_0 + \dot{y}(L)\hat{j} + U_e \hat{i} + U_e y'(L)\hat{j} + \dot{\theta} [L\hat{j} - y(L)\hat{i}], \\ \vec{V} \cdot \hat{n}_6 &= \left[\dot{R}_{0x} + U_e - \dot{\theta} y(L) \right] + y'(L) \left[\dot{R}_{0y} + \dot{y}(L) + \dot{\theta} L + U_e y'(L) \right]\end{aligned}$$

The surface terms in Eq.(4.12) have the form

$$\begin{aligned}
& \int_{\Gamma_6} \rho_f \left(k_t^{xx} \left\{ \vec{V} \cdot \hat{i} \right\} \hat{i} + k_t^{yy} \left\{ \vec{V} \cdot \hat{j} \right\} \hat{j} \right) [\vec{V} \cdot \hat{n}_6] d\Gamma = \\
& \rho_f A_6 \left(k_t^{xx} \left\{ \dot{R}_{0x} + U_e - \dot{\theta}y(L) \right\} \hat{i} + k_t^{yy} \left\{ \dot{R}_{0y} + \dot{\theta}L + \dot{y}(L) + U_e y'(L) \right\} \hat{j} \right) \times \\
& \left[\dot{R}_{0x} + U_e - \dot{\theta}y(L) + y'(L) \left\{ \dot{R}_{0y} + \dot{y}(L) + \dot{\theta}L + U_e y'(L) \right\} \right] \quad (4.43)
\end{aligned}$$

The surface terms in Eq.(4.15) have the form

$$\begin{aligned}
& k_t^{\theta\theta} \int_{\Gamma_6} (\vec{r} - \vec{r}_c) \times \left(\rho_f \vec{V} [\vec{V} \cdot \hat{n}_6] \right) d\Gamma = \rho_f A_6 k_t^{\theta\theta} \left[(L - r_{cx}) \left\{ \dot{R}_{0y} + \dot{y}(L) + \dot{\theta}L + U_e y'(L) \right\} \right. \\
& \left. - \left\{ y(L) - r_{cy} \right\} \left\{ \dot{R}_{0x} + U_e - \dot{\theta}y(L) \right\} + \dot{\theta} \left\{ L^2 + y(L)^2 - Lr_{cx} - y(L)r_{cy} \right\} \right] \times \\
& \left[\dot{R}_{0x} + U_e - \dot{\theta}y(L) + y'(L) \left\{ \dot{R}_{0y} + \dot{y}(L) + \dot{\theta}L + U_e y'(L) \right\} \right] \hat{k} \quad (4.44)
\end{aligned}$$

4.4.6 Combined Scalar Equations

The expressions in sections 4.4.4 and 4.4.5 are substituted back into Eqs.(4.12) and (4.15) to obtain the equations of motion for translation in x and y , and rotation in θ . These equations, which are given subsequently, use the following terms:

$$\begin{aligned}
m_{Tx} &= \left(m_h + m_t + m_1 + m_2 + k_h^{xx} m_3 + k_t^{xx} m_4 \right) \\
m_{Ty} &= \left(m_h + m_t + m_1 + m_2 + k_h^{yy} m_3 + k_t^{yy} m_4 \right)
\end{aligned}$$

$$\begin{aligned}
m_h &= \int_{\Omega_h} \rho_h d\Omega, & \bar{x}_h \hat{i} + \bar{y}_h \hat{j} &= \frac{1}{m_h} \int_{\Omega_h} \rho_h \vec{r} d\Omega \\
m_t &= \int_{\Omega_t} \rho_t d\Omega, & \bar{x}_t \hat{i} + \bar{y}_t \hat{j} &= \frac{1}{m_t} \int_{\Omega_t} \rho_t \vec{r} d\Omega \\
m_i &= \int_{\Omega_i} \rho_f d\Omega, & \bar{x}_i \hat{i} + \bar{y}_i \hat{j} &= \frac{1}{m_i} \int_{\Omega_i} \rho_f \vec{r} d\Omega, \quad i = 1, 2, 3, 4
\end{aligned}$$

Translation in x :

$$\begin{aligned}
& \left(\int_{\Omega_h, \Omega_t} \vec{F}_d dx + \int_{\Gamma_1(t)} \vec{F}_p d\Gamma \right) \cdot \hat{i} = \\
& m_{Tx} \ddot{R}_{0x} + \left(k_h^{xx} m_3 + k_t^{xx} m_4 \right) \dot{U}_e - \ddot{\theta} \left[(m_t + m_2 + m_4 k_t^{xx}) \frac{1}{L} \int_0^L y dx \right] \\
& - 2\dot{\theta} \left[(m_t + m_2 + m_4 k_t^{xx}) \frac{1}{L} \int_0^L \dot{y} dx + (m_2 U + m_4 k_t^{xx} U_e) \frac{y(L)}{L} \right] \\
& - \dot{\theta}^2 \left[m_h \bar{x}_h + m_t \bar{x}_t + m_1 \bar{x}_1 + m_2 \bar{x}_2 + m_3 k_h^{xx} \bar{x}_3 + m_4 k_t^{xx} \bar{x}_4 \right] - \rho_f A_1 \left(\dot{R}_{0x} + U_h \right)^2 \\
& + \rho_f A_2 \left[\dot{R}_{0x} + U - \dot{\theta} y(L) \right] \left[\dot{R}_{0x} + U - \dot{\theta} y(L) + y'(L) \left\{ \dot{R}_{0y} + \dot{y}(L) + \dot{\theta} L + U y'(L) \right\} \right] \\
& - \rho_f A_3 k_h^{xx} \left(\dot{R}_{0x} + U_e \right)^2 + \rho_f (k_h^{xx} A_4 - k_t^{xx} A_5) \left(\dot{R}_{0x} + U_e \right)^2 \\
& + \rho_f A_6 k_t^{xx} \left[\dot{R}_{0x} + U_e - \dot{\theta} y(L) \right] \left[\dot{R}_{0x} + U_e - \dot{\theta} y(L) + y'(L) \left\{ \dot{R}_{0y} + \dot{y}(L) + \dot{\theta} L + U_e y'(L) \right\} \right]
\end{aligned} \tag{4.45}$$

Translation in y :

$$\begin{aligned}
& \left(\int_{\Omega_h, \Omega_t} \vec{F}_d dx + \int_{\Gamma_1(t)} \vec{F}_p d\Gamma \right) \cdot \hat{j} = \\
& m_{Ty} \ddot{R}_{0y} + (m_t + m_2 + m_4 k_t^{yy}) \frac{1}{L} \int_0^L \ddot{y} dx + m_2 \frac{1}{L} \int_0^L (2U \dot{y}' + U^2 y'') dx \\
& + m_4 k_t^{yy} \frac{1}{L} \int_0^L (2U_e \dot{y}' + U_e^2 y'' + \dot{U}_e y') dx \\
& + \ddot{\theta} \left[m_h \bar{x}_h + m_t \bar{x}_t + m_1 \bar{x}_1 + m_2 \bar{x}_2 + m_3 k_h^{yy} \bar{x}_3 + m_4 k_t^{yy} \bar{x}_4 \right] \\
& + 2\dot{\theta} \left[m_1 U_h + m_2 U + (m_3 k_h^{yy} + m_4 k_t^{yy}) U_e \right] \\
& - \dot{\theta}^2 \left[(m_t + m_2 + m_4 k_t^{xx}) \frac{1}{L} \int_0^L y dx \right] + \rho_f A_1 \left(\dot{R}_{0y} - \dot{\theta} L_h \hat{j} \right) (-\dot{R}_{0x} - U_h) \\
& + \rho_f A_2 \left[\dot{R}_{0y} + \dot{y}(L) + \dot{\theta} L + U y'(L) \right] \left[\dot{R}_{0x} + U - \dot{\theta} y(L) \right. \\
& \quad \left. + y'(L) \left\{ \dot{R}_{0y} + \dot{y}(L) + \dot{\theta} L + U y'(L) \right\} \right] \\
& + \rho_f A_3 k_h^{yy} \left(\dot{R}_{0y} - \dot{\theta} L_h \right) [-\dot{R}_{0x} - U_e] + \rho_f (k_h^{yy} A_4 - k_t^{yy} A_5) \dot{R}_{0y} \left[\dot{R}_{0x} + U_e \right] \\
& + \rho_f A_6 k_t^{yy} \left[\dot{R}_{0y} + \dot{\theta} L + \dot{y}(L) + U_e y'(L) \right] \left[\dot{R}_{0x} + U_e - \dot{\theta} y(L) \right. \\
& \quad \left. + y'(L) \left\{ \dot{R}_{0y} + \dot{y}(L) + \dot{\theta} L + U_e y'(L) \right\} \right] \tag{4.46}
\end{aligned}$$

Rotation in θ :

$$\begin{aligned}
& \int_{\Omega_h, \Omega_t} (\vec{r} - \vec{r}_c) \times \vec{F}_d dx + \int_{\Gamma_1} (\vec{r} - \vec{r}_c) \times \vec{F}_p d\Gamma = \frac{(m_t + m_2 + m_4 k_t^{\theta\theta})}{L} \int_0^L (x - r_{cx}) \ddot{y} dx \\
& + \frac{m_2}{L} \int_0^L (x - r_{cx}) (2U \dot{y}' + U^2 y'') dx + \frac{m_4 k_t^{\theta\theta}}{L} \int_0^L (x - r_{cx}) (2U_e \dot{y}' + U_e^2 y'' + \dot{U}_e y') dx \\
& + \dot{U}_e \left[m_3 k_h^{\theta\theta} r_{cy} - \frac{m_4 k_t^{\theta\theta}}{L} \int_0^L (y - r_{cy}) dx \right] + \ddot{\theta} \left\{ J_{zh} + (m_1 + m_3 k_h^{\theta\theta}) \frac{L_h^2}{3} \right. \\
& + (m_t + m_2 + m_4 k_t^{\theta\theta}) \left[\frac{L^2}{3} + \frac{1}{L} \int_0^L y^2 dx \right] - (m_t + m_2 + m_4 k_t^{\theta\theta}) \left[\frac{1}{L} \int_0^L y dx \right]^2 \\
& \left. - \left[m_h \bar{x}_h^2 + m_t \bar{x}_t^2 + m_1 \bar{x}_1^2 + m_2 \bar{x}_2^2 + m_3 k_h^{\theta\theta} \bar{x}_3^2 + m_4 k_t^{\theta\theta} \bar{x}_4^2 \right] \right\} \\
& + 2\dot{\theta} \left[\frac{m_1 U_h + m_3 k_h^{\theta\theta} U_e}{L_h} \int_{-L_h}^0 (x - r_{cx}) dx + \frac{m_2 U + m_4 k_t^{\theta\theta} U_e}{L} \int_0^L (x - r_{cx}) dx \right. \\
& \left. + \frac{m_t + m_2 + m_4 k_t^{\theta\theta}}{L} \int_0^L (y - r_{cy}) \dot{y} dx + \frac{m_2 U + m_4 U_e k_t^{\theta\theta}}{L} \int_0^L (y - r_{cy}) y' dx \right] \\
& + \rho_f A_1 \left[(-L_h - r_{cx}) \dot{R}_{0y} + r_{cy} (\dot{R}_{0x} + U_h) + \dot{\theta} (L_h^2 + L_h r_{cx}) \right] [-\dot{R}_{0x} - U_h] \\
& + \rho_f A_2 \left[(L - r_{cx}) \left\{ \dot{R}_{0y} + \dot{y}(L) + \dot{\theta} L + U y'(L) \right\} \right. \\
& \quad \left. - \{y(L) - r_{cy}\} \{ \dot{R}_{0x} + U - \dot{\theta} y(L) \} + \dot{\theta} \left\{ L^2 + y^2(L) - L r_{cx} - y(L) r_{cy} \right\} \right] \times \\
& \quad \left[\left\{ \dot{R}_{0x} + U - \dot{\theta} y(L) \right\} + y'(L) \left\{ \dot{R}_{0y} + \dot{y}(L) + \dot{\theta} L + U y'(L) \right\} \right] \\
& + \rho_f A_3 k_h^{\theta\theta} \left(\{-L_h - r_{cx}\} \dot{R}_{0y} + r_{cy} \left\{ \dot{R}_{0x} + U_e \right\} + \dot{\theta} \left\{ L_h^2 + L_h r_{cx} \right\} \right) [-\dot{R}_{0x} - U_e] \\
& + \rho_f (A_4 k_h^{\theta\theta} - A_5 k_t^{\theta\theta}) \left(-r_{cx} \dot{R}_{0y} + r_{cy} \left\{ \dot{R}_{0x} + U_e \right\} \right) [\dot{R}_{0x} + U_e] \\
& + \rho_f A_6 k_t^{\theta\theta} \left[(L - r_{cx}) \left\{ \dot{R}_{0y} + \dot{y}(L) + \dot{\theta} L + U_e y'(L) \right\} \right. \\
& \quad \left. - \{y(L) - r_{cy}\} \left\{ \dot{R}_{0x} + U_e - \dot{\theta} y(L) \right\} + \dot{\theta} \left\{ L^2 + y(L)^2 - L r_{cx} - y(L) r_{cy} \right\} \right] \times \\
& \quad \left[\dot{R}_{0x} + U_e - \dot{\theta} y(L) + y'(L) \left\{ \dot{R}_{0y} + \dot{y}(L) + \dot{\theta} L + U_e y'(L) \right\} \right] \hat{k} \tag{4.47}
\end{aligned}$$

4.4.7 Pressure and Drag Forces

In this section, expressions for the pressure and drag forces, \vec{F}_p and \vec{F}_d that appear on the left side of Eqs.(4.45), (4.46) and (4.47) are provided. The force exerted by the pressure acting at the inlet is computed via analysis of a captured quasi-steady streamtube:

$$\int_{\Gamma_1} \vec{F}_p dA = -A_1 \rho_f U_h (U_h - U_e) \hat{i} \quad (4.48)$$

On the left side of the scalar equations in the previous section, the pressure \vec{F}_p is integrated over the surface of the inlet Γ_1 . It is assumed to be uniform over this area.

An expression for the drag force is obtained by first writing the components of the velocity of the rigid head and flexible tail in the normal and tangential directions (V_h^N , V_h^T , V_t^N , V_t^T):

$$\begin{aligned} V_h^N &= \dot{R}_{0y} + \dot{\theta}x & V_t^N &= \dot{R}_{0y} + \dot{y} + \dot{\theta}x - (\dot{R}_{0x} - \dot{\theta}y)y' \\ V_h^T &= \dot{R}_{0x} & V_t^T &= \dot{R}_{0x} - \dot{\theta}y + (\dot{R}_{0y} + \dot{y} + \dot{\theta}x)y' \end{aligned} \quad (4.49)$$

Using a model similar to that proposed by [42]¹, the distributed drag forces on the rigid head and flexible tail in the normal and tangential directions (D_h^N , D_h^T , D_t^N , D_t^T) are written as

$$\begin{aligned} D_h^N &= -\rho_f P_h (C_h^N V_h^T V_h^N + c_h V_h^N) & D_t^N &= -\rho_f h (C_t^N V_t^T V_t^N + c_t V_t^N) \\ D_h^T &= -\rho_f P_h C_h^T V_h^T |V_h^T| & D_t^T &= -\rho_f P_t C_t^T V_t^T |V_t^T| \end{aligned} \quad (4.50)$$

where P_h , P_t are the perimeters of the head and tail in the yz plane. The coefficients C_h^N , C_t^N , C_h^T and C_t^T are empirical drag coefficients in the normal and tangential directions;

1: While terms similar to $c_h V_h^N$ or $c_t V_t^N$ do not appear in [42], later workers recognized the need for a linear correction. Some of these works can be found in [31].

and c_h and c_t are linear damping coefficients.

The above expressions for drag are used to derive the components of drag in the x and y directions (D_h^x , D_h^y , D_t^x , D_t^y):

$$\begin{aligned} D_h^x &= D_h^T & D_t^x &= D_t^T - D_t^N y' \\ D_h^y &= D_h^N & D_t^y &= D_t^N + D_t^T y' \end{aligned} \quad (4.51)$$

Substitution of Eqs.(4.49) and (4.50) into (4.51) yields

$$\begin{aligned} D_h^x &= -\rho_f P_h \left[C_h^T \dot{R}_{0x} \left| \dot{R}_{0x} \right| \right] \\ D_h^y &= -\rho_f P_h \left[C_h^N \dot{R}_{0x} \left(\dot{R}_{0y} + \dot{\theta} x \right) + c_h \left(\dot{R}_{0y} + \dot{\theta} x \right) \right] \end{aligned} \quad (4.52)$$

and

$$\begin{aligned} D_t^x &= -\rho_f P_t \left[C_t^T \left\{ \dot{R}_{0x} - \dot{\theta} y + \left(\dot{R}_{0y} + \dot{y} + \dot{\theta} x \right) y' \right\} \left| \dot{R}_{0x} - \dot{\theta} y + \left(\dot{R}_{0y} + \dot{y} + \dot{\theta} x \right) y' \right| \right] \\ &\quad + \rho_f h \left[C_t^N \left\{ \dot{R}_{0x} - \dot{\theta} y + \left(\dot{R}_{0y} + \dot{y} + \dot{\theta} x \right) y' \right\} \left\{ \dot{R}_{0y} + \dot{y} + \dot{\theta} x - \left(\dot{R}_{0x} - \dot{\theta} y \right) y' \right\} \right. \\ &\quad \left. + c_t \left\{ \dot{R}_{0y} + \dot{y} + \dot{\theta} x - \left(\dot{R}_{0x} - \dot{\theta} y \right) y' \right\} \right] y' \\ D_t^y &= -\rho_f h \left[C_t^N \left\{ \dot{R}_{0x} - \dot{\theta} y + \left(\dot{R}_{0y} + \dot{y} + \dot{\theta} x \right) y' \right\} \left\{ \dot{R}_{0y} + \dot{y} + \dot{\theta} x - \left(\dot{R}_{0x} - \dot{\theta} y \right) y' \right\} \right. \\ &\quad \left. + c_t \left\{ \dot{R}_{0y} + \dot{y} + \dot{\theta} x - \left(\dot{R}_{0x} - \dot{\theta} y \right) y' \right\} \right] \\ &\quad - \rho_f P_t \left[C_t^T \left\{ \dot{R}_{0x} - \dot{\theta} y + \left(\dot{R}_{0y} + \dot{y} + \dot{\theta} x \right) y' \right\} \left| \dot{R}_{0x} - \dot{\theta} y + \left(\dot{R}_{0y} + \dot{y} + \dot{\theta} x \right) y' \right| \right] y' \end{aligned} \quad (4.53)$$

In addition to these distributed viscous forces, the low pressure region at the blunt trailing end of a slender body is an additional source of drag. Consistent with the literature [31],

this communication refers to this as a drag force, rather than a pressure force. These forces, commonly referred to as base drag, are given by the following expressions:

$$D_h^b = -\frac{\rho f}{2} A_h C_h^b \left[V_h^T \middle| V_h^T \right]_{x=0}, \quad D_t^b = -\frac{\rho f}{2} A_t C_t^b \left[V_t^T \middle| V_t^T \right]_{x=L} \quad (4.54)$$

where A_h , A_t are the cross-sectional areas of the head and tail in the yz plane, and C_h^b , C_t^b are the base drag coefficients of the head and tail. Using Eqs.(4.52), (4.53) and (4.54), the drag force \vec{F}_d in Eqs.(4.45), (4.46), and (4.47) is written in component form as follows

$$\begin{aligned} \int_{\Omega_h, \Omega_t} \vec{F}_d dx \cdot \hat{i} &= \int_{\Omega_h} D_h^x d\Omega + \int_{\Omega_t} D_t^x d\Omega + D_h^b + D_t^b \\ \int_{\Omega_h, \Omega_t} \vec{F}_d dx \cdot \hat{j} &= \int_{\Omega_h} D_h^y d\Omega + \int_{\Omega_t} D_t^y d\Omega + D_t^b y'(L) \end{aligned}$$

4.5 Dynamics of the Flexible Tail

4.5.1 Equations of Motion

In section 4.4 a generic function $y(x, t)$ was used to describe the motion of the flexible tail. In this section, we will derive the equation of motion of the tail such that $y(x, t)$ can be computed. To this end, Fig.4.4 presents the free-body diagrams of differential elements within control volumes Ω_2 , Ω_t and Ω_4 . A balance of forces for each element in the x and y directions is provided below:

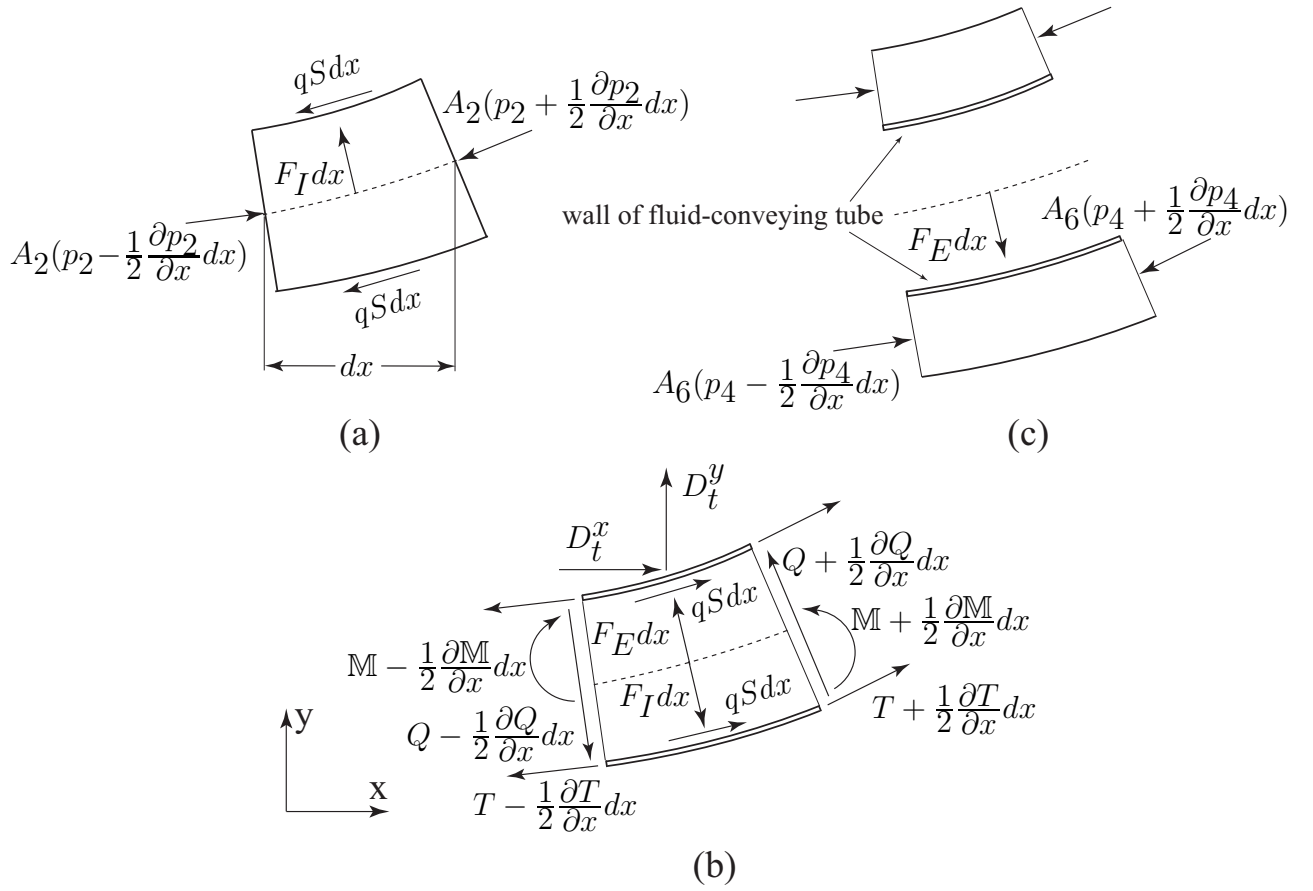


Figure 4.4: Free-body diagrams of (a) a differential element of Ω_2 (tail internal fluid), (b) a differential element of Ω_t (flexible tail), and (c) a differential element of Ω_4 (tail external fluid).

Tail Internal Fluid:

$$\left[-A_2 \frac{\partial p_2}{\partial x} - qS - F_I \frac{\partial y}{\partial x} \right] \hat{i} + \left[F_I - A_2 \frac{\partial}{\partial x} \left(\frac{\partial p_2}{\partial x} \frac{\partial y}{\partial x} \right) - qS \frac{\partial y}{\partial x} \right] \hat{j} = \frac{m_2}{L} \frac{d\vec{V}}{dt} \quad (4.55)$$

where

$$\frac{\partial \vec{V}}{\partial t} = \ddot{\vec{R}}_0 + \left[\ddot{y} + 2U\dot{y}' + U^2 y'' \right] \hat{j} + \ddot{\theta} \left[x \hat{j} - y \hat{i} \right] + 2\dot{\theta} \left[U \hat{j} - (\dot{y} + Uy') \hat{i} \right]$$

Flexible Tail:

$$\begin{aligned} & \left[\frac{\partial T}{\partial x} + qS + F_I \frac{\partial y}{\partial x} - Q \frac{\partial^2 y}{\partial x^2} - F_E \frac{\partial y}{\partial x} + D_t^x \right] \hat{i} + \\ & \left[-F_I + \frac{\partial Q}{\partial x} + \frac{\partial}{\partial x} \left(\frac{\partial T}{\partial x} \frac{\partial y}{\partial x} \right) + qS \frac{\partial y}{\partial x} + F_E + D_t^y \right] \hat{j} = \frac{m_t}{L} \frac{\partial \vec{V}}{\partial t} \end{aligned} \quad (4.56)$$

where

$$\frac{\partial \vec{V}}{\partial t} = \ddot{\vec{R}}_0 + \ddot{y} \hat{j} + \ddot{\theta} \left[x \hat{j} - y \hat{i} \right] - 2\dot{\theta} \dot{y} \hat{i} - \dot{\theta}^2 \left[x \hat{i} + y \hat{j} \right]$$

Tail External Fluid:

$$\begin{aligned} & \left[-A_6 \frac{\partial p_4}{\partial x} + F_E \frac{\partial y}{\partial x} \right] \hat{i} - \left[F_E + A_6 \frac{\partial}{\partial x} \left(\frac{\partial p_4}{\partial x} \frac{\partial y}{\partial x} \right) \right] \hat{j} = \\ & \frac{m_4}{L} \left[\left(k_t^{xx} \frac{\partial \vec{V}}{\partial t} \cdot \hat{i} \right) \hat{i} + \left(k_t^{yy} \frac{\partial \vec{V}}{\partial t} \cdot \hat{j} \right) \hat{j} \right] \end{aligned} \quad (4.57)$$

where

$$\begin{aligned} \frac{\partial \vec{V}}{\partial t} = & \ddot{\vec{R}}_0 + \left[\ddot{y} + 2U_e \dot{y}' + U_e^2 y'' + \dot{U}_e y' \right] \hat{j} + \dot{U}_e \hat{i} + \ddot{\theta} \left[x \hat{j} - y \hat{i} \right] + 2\dot{\theta} \left[U \hat{j} - (\dot{y} + U y') \hat{i} \right] \\ & - \dot{\theta}^2 \left[x \hat{i} + y \hat{j} \right] \end{aligned}$$

By combining the x -components of Eqs.(4.55), (4.56) and (4.57), we obtain the following expression which will be used to simplify the expression that will be obtained by summation of the y components:

$$\frac{\partial T}{\partial x} - A_2 \frac{\partial p_2}{\partial x} - A_6 \frac{\partial p_4}{\partial x} = \left(\frac{m_t + m_2 + m_4 k_t^{xx}}{L} \right) a_x + \frac{m_4 k_t^{xx}}{L} \dot{U}_e - D_t^x \quad (4.58)$$

where

$$a_x = \ddot{\vec{R}}_0 \cdot \hat{i} - \ddot{\theta} y - 2\dot{\theta} \left[\dot{y} + \frac{m_2}{m_t + m_2 + m_4 k_t^{xx}} U \frac{\partial y}{\partial x} + \frac{m_4 k_t^{xx}}{m_t + m_2 + m_4 k_t^{xx}} U_e \frac{\partial y}{\partial x} \right] - \dot{\theta}^2 x \quad (4.59)$$

Summation of the y -components of Eqs.(4.55), (4.56) and (4.57) gives:

$$\begin{aligned} D_t^y - EI \frac{\partial^4 y}{\partial x^4} + \frac{\partial}{\partial x} \left[(T - A_2 p_2 - A_6 p_4) \frac{\partial y}{\partial x} \right] = & \left[\frac{m_2}{L} U^2 + \frac{m_4 k_t^{yy}}{L} U_e^2 \right] \frac{\partial^2 y}{\partial x^2} \\ & + 2 \left[\frac{m_2}{L} U + \frac{m_4 k_t^{yy}}{L} U_e \right] \frac{\partial^2 y}{\partial x \partial t} + \frac{m_4 k_t^{yy}}{L} \dot{U}_e \frac{\partial y}{\partial x} + \frac{m_t + m_2 + m_4 k_t^{yy}}{L} \left(\frac{\partial^2 y}{\partial t^2} + a_y \right) \end{aligned} \quad (4.60)$$

where

$$a_y = \ddot{\vec{R}}_0 \cdot \hat{j} + \ddot{\theta}x + 2\dot{\theta} \left[\frac{m_2}{m_t + m_2 + m_4 k_t^{yy}} U + \frac{m_4 k_t^{yy}}{m_t + m_2 + m_4 k_t^{yy}} U_e \right] - \dot{\theta}^2 y \quad (4.61)$$

The combined tension-pressure gradient term in Eq.(4.60) can be rewritten as:

$$\frac{\partial}{\partial x} \left[(T - A_2 p_2 - A_6 p_4) \frac{\partial y}{\partial x} \right] = \left(\frac{\partial T}{\partial x} - A_2 \frac{\partial p_2}{\partial x} - A_6 \frac{\partial p_4}{\partial x} \right) \frac{\partial y}{\partial x} + (T - A_2 p_2 - A_6 p_4) \frac{\partial^2 y}{\partial x^2}$$

Using Eq.(4.58), terms on the right hand side of the above equation can be written as

$$\begin{aligned} \left(\frac{\partial T}{\partial x} - A_2 \frac{\partial p_2}{\partial x} - A_6 \frac{\partial p_4}{\partial x} \right) &= \frac{m_t + m_2 + m_4 k_t^{xx}}{L} a_x + \frac{m_4 k_t^{xx}}{L} \dot{U}_e - D_t^x \\ (T - A_2 p_2 - A_6 p_4) &= - \int_x^L \frac{\partial}{\partial x} (T - A_2 p_2 - A_6 p_4) dx + \underbrace{T(L) - A_2 p(L) - A_6 p_4(L)}_{=D_t^b} \end{aligned}$$

Note that the final term in the above equation represents the low pressure region at the blunt trailing edge of the tail, which is commonly termed the base drag. Substitution of the above expressions into Eq.(4.60), yields the equation of motion for transverse vibration of the flexible tail:

$$\begin{aligned} EI \frac{\partial^4 y}{\partial x^4} &+ \left[\frac{m_2}{L} U^2 + \frac{m_4 k_t^{yy}}{L} U_e^2 \right. \\ &+ \int_x^L \left(\frac{m_t + m_2 + m_4 k_t^{xx}}{L} a_x + \frac{m_4 k_t^{xx}}{L} \dot{U}_e - D_t^x \right) dx - D_t^b \left. \right] \frac{\partial^2 y}{\partial x^2} \\ &+ \left[- \frac{m_t + m_2 + m_4 k_t^{xx}}{L} a_x - \left(\frac{m_4 k_t^{xx} - m_4 k_t^{yy}}{L} \right) \dot{U}_e + D_t^x \right] \frac{\partial y}{\partial x} \\ &+ 2 \left[\frac{m_2}{L} U + \frac{m_4 k_t^{yy}}{L} U_e \right] \frac{\partial^2 y}{\partial x \partial t} + \frac{m_t + m_2 + m_4 k_t^{yy}}{L} \left(\frac{\partial^2 y}{\partial t^2} + a_y \right) - D_t^y = 0 \quad (4.62) \end{aligned}$$

The boundary conditions for the flexible tail are the familiar expressions for a cantilever:

$$y(0, t) = 0 \quad \frac{\partial y(0, t)}{\partial x} = 0 \quad \frac{\partial^2 y(L, t)}{\partial x^2} = 0 \quad \frac{\partial^3 y(L, t)}{\partial x^3} = 0 \quad (4.63)$$

Note that while the system presented here is similar to that derived in [19], the boundary condition at $x = 0$ is not the same; in that work, the authors used an inertial frame at $x = 0$, and allowed the rigid head to move in the y -direction. In contrast, since the boundary conditions for the present system are written in a non-inertial frame which is fixed to the undeformed neutral axis of the tail, the simple equations for a cantilever are used.

4.5.2 Discretization

A finite-difference scheme was used to discretize the PDE in Eq.(4.62), in which the continuous function $y(x, t)$ is considered to have discrete values y_1, y_2, \dots, y_N at the locations x_1, x_2, \dots, x_N . The five-point stencils in Eq.(4.64) were used to approximate the required spatial derivatives at the i -th point:

$$\frac{\partial y_i}{\partial x} = \frac{1}{12\Delta} [y_{i-2} - 8y_{i-1} + 8y_{i+1} - y_{i+2}], \quad (4.64a)$$

$$\frac{\partial^2 y_i}{\partial x^2} = \frac{1}{12\Delta^2} [-y_{i-2} + 16y_{i-1} - 30y_i + 16y_{i+1} - y_{i+2}], \quad (4.64b)$$

$$\frac{\partial^3 y_i}{\partial x^3} = \frac{1}{2\Delta^3} [-y_{i-2} + 2y_{i-1} - 2y_{i+1} + y_{i+2}], \quad (4.64c)$$

$$\frac{\partial^4 y_i}{\partial x^4} = \frac{1}{\Delta^4} [y_{i-2} - 4y_{i-1} + 6y_i - 4y_{i+1} + y_{i+2}], \quad (4.64d)$$

where Δ is the spacing between the points x_{i+1} and x_i . The central difference relationships provided in Eq.(4.64) were used for all points on the flexible tail; “mirror” conditions were used to handle the edge values and implement the boundary conditions. In this method, additional points are created at $x < 0$ and $x > L$ such that evaluating the stencils in Eq.(4.64) yields the boundary conditions of Eq.(4.63). The boundary condition $\partial y / \partial x(0) = 0$ is implemented by creating the points y_0 and y_{-1} :

$$y_0 = y_2 \quad y_{-1} = y_3$$

The condition $y(0) = 0$ is implemented by simply setting $y_1 = 0$. The two conditions at $x = L$ are created by rearranging the expressions for $\partial^2 y / \partial x^2 = 0$ and $\partial^3 y / \partial x^3 = 0$ yields:

$$\begin{aligned} -y_{(N-2)} + 16y_{(N-1)} - 30y_N &= -16y_{(N+1)} + y_{(N+2)} \\ -y_{(N-2)} + 2y_{(N-1)} &= 2y_{(N+1)} - y_{(N+2)} \end{aligned}$$

which can be solved for the values $y_{(N+1)}$ and $y_{(N+2)}$:

$$y_{(N+1)} = \frac{15y_N - 9y_{(N-1)} + y_{(N-2)}}{7}, \quad y_{(N+2)} = \frac{-30y_N + 32y_{(N-1)} + 9y_{(N-2)}}{7}$$

The scalar equations, Eqs.(4.45), (4.46) and (4.47) also require integration of $y(x, t)$; to approximate these integrals, a discrete trapezoidal approximation is used, such that

$$\int_0^L y \, dx \approx \left[y_1 + y_N + \frac{1}{2} \sum_{i=2}^{N-1} y_i \right] \Delta \quad (4.65)$$

After applying these discrete approximations to the integrodifferential terms, $N + 3$ ordinary

differential equations corresponding to the three scalar equations remain: Eqs.(4.45), (4.46) and (4.47) and the N equations that result from discretization of Eq.(4.62). These $N + 3$ equations are second-order in time, and are transformed into a system of $2N + 6$ first order equations. These equations are solved with a fourth-order Runge-Kutta algorithm.

4.6 Numerical Simulations

4.6.1 Simulation Parameters and Procedure

Simulations were conducted using three different configurations for the tail: a flexible tail with a finned-tube geometry as shown in Fig.4.5, a rigid tail with identical geometry to that of the flexible tail, and a rigid tube which does not have the vertical fins which exist on the other two configurations. The two configurations of the submersible with rigid tail structures were simulated to provide baseline measures of performance which were compared to the performance of the submersible with the flexible fluttering tail. Experimental studies of the rigid configurations were used to obtain good estimates of the viscous drag coefficients used in the simulations. The values of the parameters used for the flexible tube configuration in these simulations are provided in Table 4.2. All values are the same for the rigid tail configuration, except that the Young's modulus E is irrelevant since the tail does not oscillate.

4.6.2 Estimation of Drag Coefficients

The second-order drag coefficients C_h^T , C_t^T , C_h^N , C_t^N , C_h^b , and C_t^b , and the linear coefficients c_h and c_t have been estimated using a combination of analysis of experimental results and extrapolation of published correlations. The tangential and base drag coefficients are

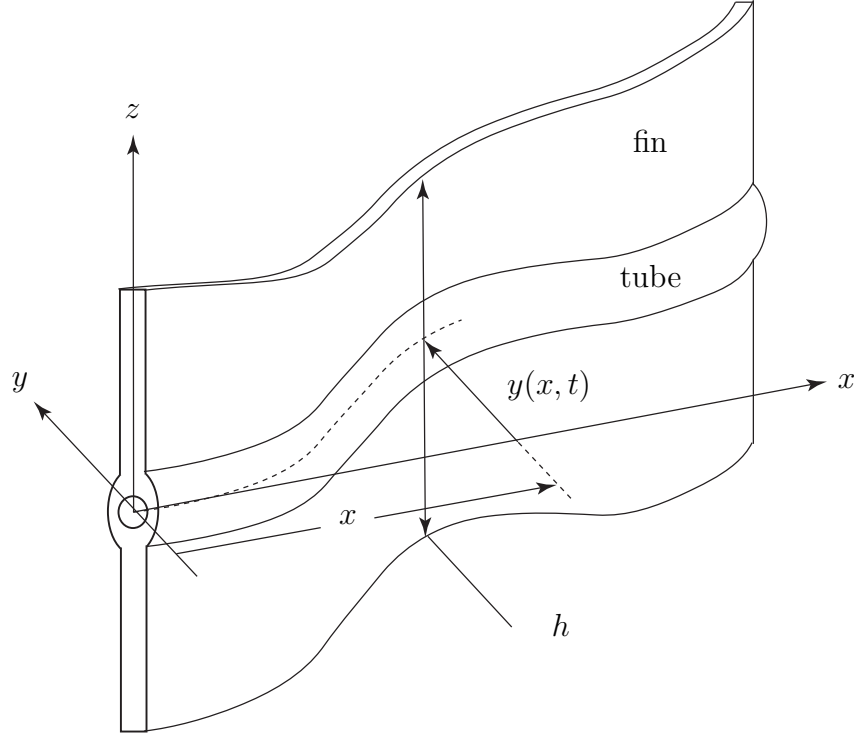


Figure 4.5: A fluid-conveying beam in the form of a finned-tube with fin height h .

calculated by analyzing the speeds of the rigid tube and rigid tail configurations. For these configurations, the thrust is well-known, since it comes only from the jet. The rigid state of the system means that an expression for the balance of forces on the submersible in the x -direction can be easily expressed as:

$$A_1 \rho_f U_h (U_h - U_e) = \rho_f \left(\frac{C_h^b A_h}{2} + \frac{C_t^b A_t}{2} + C_h^T P_h L_h + C_t^T P_t L \right) U_e^2 \quad (4.66)$$

Equation (4.66) can be written for both the case of the rigid tail and the rigid tube using values of external velocity U_e which are determined experimentally. Two additional equations

Table 4.2: Parameters used in simulations

Masses (kg)							
m_h	m_t	m_1	m_2	m_3	m_4		
4.200	0.045	0.020	0.017	1.800	1.600		
Added mass coefficients							
k_{xx}^h	k_{xx}^t	k_{yy}^h	k_{yy}^t	$k_{\theta\theta}^h$	$k_{\theta\theta}^t$		
0.10	0.10	1.00	1.00	1.00	1.00		
Center of mass locations (m)							
\bar{x}_h	\bar{x}_t	\bar{x}_1	\bar{x}_2	\bar{x}_3	\bar{x}_4		
−0.20	0.17	−0.20	0.17	−0.20	0.17		
Lengths (m)							
L_h	L	P_h	P_t	h			
0.390	0.340	0.239	0.163	0.067, 0.072, 0.077			
Miscellaneous (SI units)							
U_h	U	ρ_f	J_{zh}	I	E		
4.0	4.0	1000	0.217	5.65×10^{-10}	1.30×10^6		
Areas $\times 10^{-4}$ (m ²)							
A_h	A_t	A_1	A_2	A_3	A_4	A_5	A_6
45.60	0.495	0.500	0.500	45.60	45.60	46.80	46.80
Drag coefficients							
C_h^N	C_t^N	C_h^T	C_t^T	C_h^b	C_t^b	$c_h(m/s)$	$c_t(m/s)$
0.0118	0.0039	0.0060	0.0020	0.0830	0.0790	0.116	0.116

from [21]¹ relate the tangential and base drag coefficients:

$$C_h^b = \frac{0.029}{\sqrt{C_h^T P_h L_h / A_h}} \quad C_t^b = \frac{0.135}{\sqrt[3]{(C_h^T S_h + C_t^T P_t L) / A_t}} \quad (4.67)$$

1: Chapter 3 in that work.

In the above equations, the denominator is a measure of the tangential drag on the “fore-body” of the body in question, *i.e.* the portion of the submersible that is ahead of the base. The different forms of the expressions for C_h^b and C_t^b reflect the flat aspect ratio of the tail’s cross-section relative to that of the head; the two-dimensional form of the correlation found in [21] has been used for the tail. Equations (4.66) and (4.67) may now be solved for the tangential and base coefficients C_h^T and C_t^T , and C_h^b and C_t^b . The second-order normal coefficients have been set as $C_h^N = 2.0 C_h^T$ and $C_t^N = 2.0 C_t^T P_t/h$, per the discussion in [31]. The additional P_t/h scaling on C_t^N is to account for the different length scaling for the tail in the tangential and normal directions.

The linear coefficients c_h and c_t can be estimated by using a procedure similar to that employed by [6]. In that work, Batchelor analytically derived an estimate for the viscous drag produced by the boundary layer on an oscillating cylinder; this result provides an estimate for c_h . Batchelor’s method [6] can be extended to produce an estimate for the drag coefficient c_t on an oscillating flat plate, that approximates the tail. This procedure yields estimates of $c_t = 0.0065 \text{ m/s}$ and $c_h = 0.0108 \text{ m/s}$. It should be mentioned that Batchelor’s procedure estimates the velocity and velocity gradient at the surface using a method more appropriate to flow with very low Reynolds number, and the coefficients cited in Table 4.2 have been found to produce oscillations more similar in magnitude to those of the physical device.

4.6.3 Simulation Results

Using the methods and parameters given above, the equations of motion have been solved for the flexible tail, rigid tail and rigid tube cases. The forward speed of the submersible

using each of these configurations is shown in Fig.4.6, along with the deflection of the tip of the tail ($x = L$) and orientation of the rigid head for the flexible tail configuration. The maximum speed of the flexible tail configuration exceeds that of the rigid tail configuration, indicating that the fluttering motion of the tail generates a net thrust. A large increase in the amplitude of oscillation of the tail tip is observed near $t = 10$ sec - this coincides with an increase in the speed of the submersible with the flexible tail configuration.

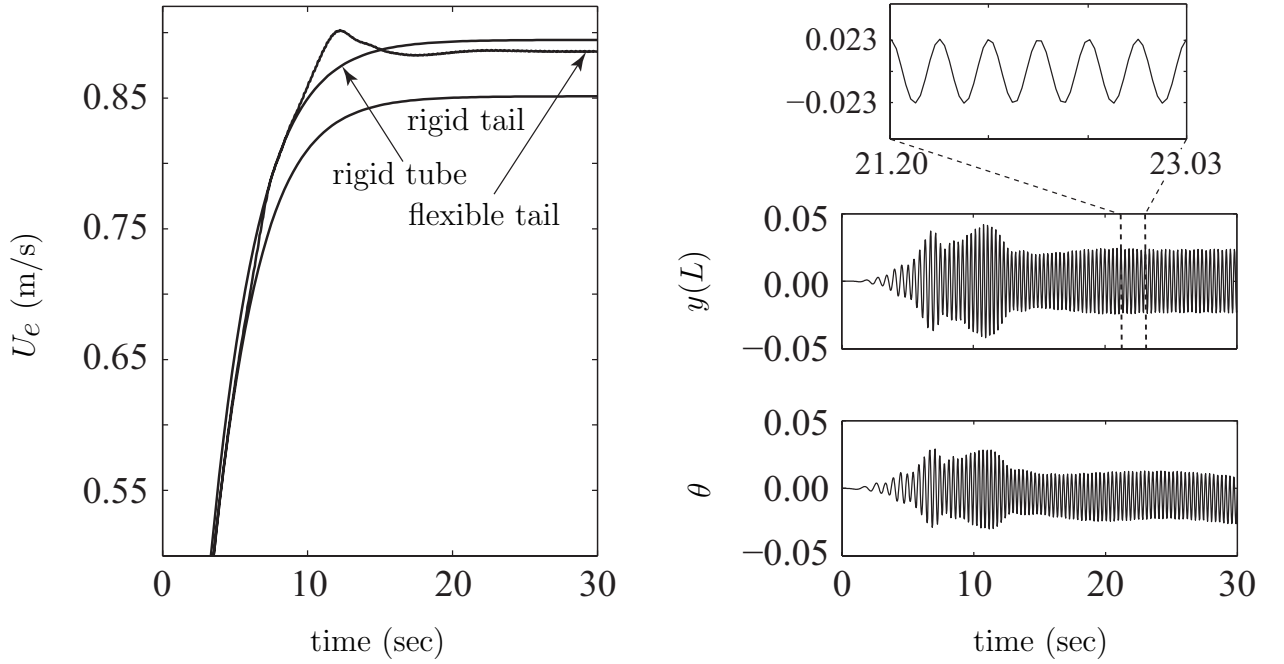


Figure 4.6: The subplot on the left shows the forward speed of the submersible with flexible tail, rigid tail, and rigid tube configurations. On the right, the displacement of the tail tip $y(L)$ and orientation θ of the rigid head of the submersible are given for the flexible tail configuration.

The steady-state speed of the flexible tail configuration is somewhat faster than the dimensionally identical rigid tail and somewhat slower than the finless rigid tube; this trend is consistent with experimental trials conducted on these configurations presented in section 5.4. The lower speed of the flexible and rigid tail configurations is the result of the drag created by the fins affixed to the tube. The additional thrust created by the fluttering action

of the flexible tail is not sufficient to overcome this drag for the geometry simulated in Fig.4.6. A fluttering tail configuration can however exceed the speed of a rigid tube - this is shown later in this section.

As an aside, note that the oscillations of the tail tip shown in Fig.4.6 become bounded as time increases. This would not be expected in an unstable linear system, in which perturbations grow unbounded as $t \rightarrow \infty$. The system simulated is indeed non-linear, unlike the systems presented in Chapters 2 and 3. The non-linear terms responsible for the bounded behavior of the tail are the quadratic drag terms presented in section 4.4.7, *e.g.*, $V_t^T \left| V_t^T \right|$. Since these terms are quadratic with respect to the speed of the tail, increasing the tail's amplitude causes a large increase in drag, effectively bounding the tail's motion.

The traveling wave nature of the flexible tail's motion is made clear in Fig.4.7, which provides a set of images of the submersible over one cycle of oscillation. The dynamic coupling between the tail's motion and the rigid head is evident from these images where it is observed that the angle of the rigid head is not constant throughout the cycle. The period of oscillation for the tail of 0.3 sec is very similar to the experimentally observed value of ≈ 0.33 sec.

Additional simulations have been performed using different tail geometries. To conform to assumption A1, all simulated tails have rectangular planforms. Figure 4.8 presents the forward speeds of three flexible tails with $h = 0.077$ and lengths $L = 0.30, 0.34$ and 0.38 . The speed achieved with the $L = 0.30$ tail is comparable to that achieved with the rigid tail shown in Fig.4.6. This is because the $L = 0.30$ tail is on the border of flutter instability - this can be verified from the amplitude of tail oscillation shown in Fig.4.8. The $L = 0.34$ tail exhibits the highest forward speed of these configurations, although the behavior of the

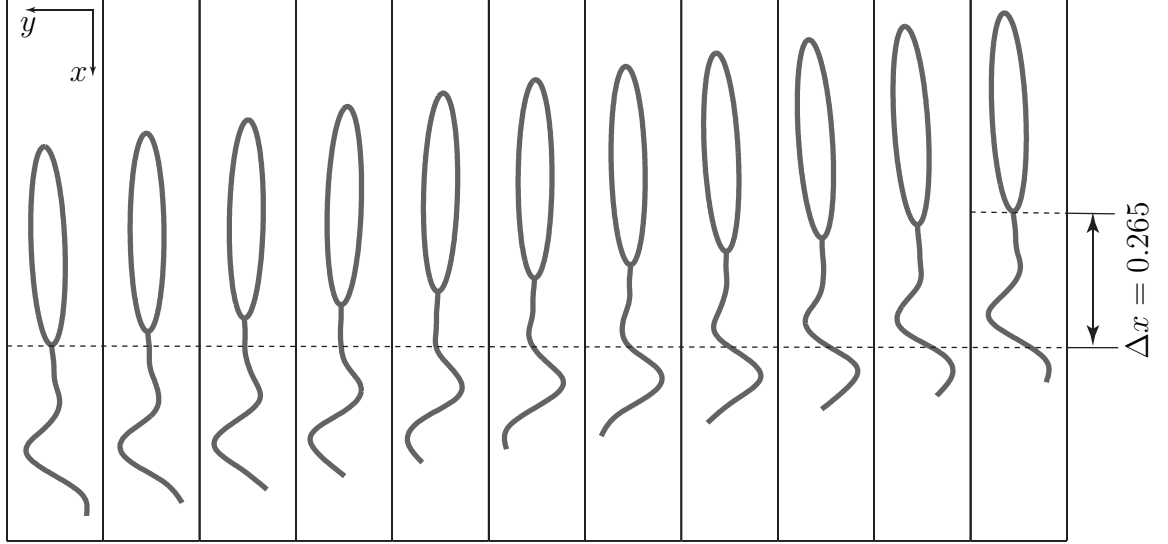


Figure 4.7: Sequence of images of the submersible with the flexible tail. The scaling for the y axis has been adjusted to make the tail oscillations more visible.

$L = 0.38$ tail also indicates thrust production by fluttering action. The oscillations in the forward speed of the $L = 0.38$ tail are the result of that tail temporarily stabilizing. An analytical treatment of a simplified version of the submersible showed similar stabilization behavior (Hellum et al., 2010).

In Fig.4.9, the forward speeds of three $L = 0.34$ tails are presented; the heights of the tails are different and equal to $h = 0.067$, 0.072 , and 0.077 . A tail height of $h = 0.082$ was also simulated. The data for this configuration is not shown in Fig.4.9 since it did not exhibit flutter instability; its forward speed is presented in Table 4.3. The $h = 0.072$ tail exhibits the highest forward speed of these configurations, although the behavior of both the 0.067 and 0.077 tails also indicate thrust production by fluttering action. Note that the steady state speed of the $h = 0.072$ tail is $U_e = 0.933$, meaning that this geometry is faster than the rigid tube configuration.

A summary of the data in this section is provided in Table 4.3. It is interesting that the two flexible tail configurations with minimal oscillations, $(h, L) = (0.077, 0.30)$ and

Table 4.3: Different tail geometries and their forward speeds and steady-state oscillation amplitudes.

Illustration	Configuration	L	h	$y(L)$	U_e
Fig.4.6	Flexible Tail	0.34	0.077	0.023	0.889
	Rigid Tail	0.34	0.077	-	0.851
	Rigid Tube	0.34	-	-	0.894
Fig.4.8	Flexible Tail	0.30	0.077	0.001	0.857
	Flexible Tail	0.34	0.077	0.023	0.889
	Flexible Tail	0.38	0.077	0.020	0.876
Fig.4.9	Flexible Tail	0.34	0.067	0.025	0.874
	Flexible Tail	0.34	0.072	0.044	0.933
	Flexible Tail	0.34	0.077	0.023	0.889
	Flexible Tail	0.34	0.082	0	0.849

$(h, L) = (0.082, 0.34)$ have forward speeds which are close to, but not equal to, that of the rigid tail configuration with $(h, L) = (0.077, 0.34)$. This is because of the change in surface area and associated drag of these two configurations relative to the rigid tail.

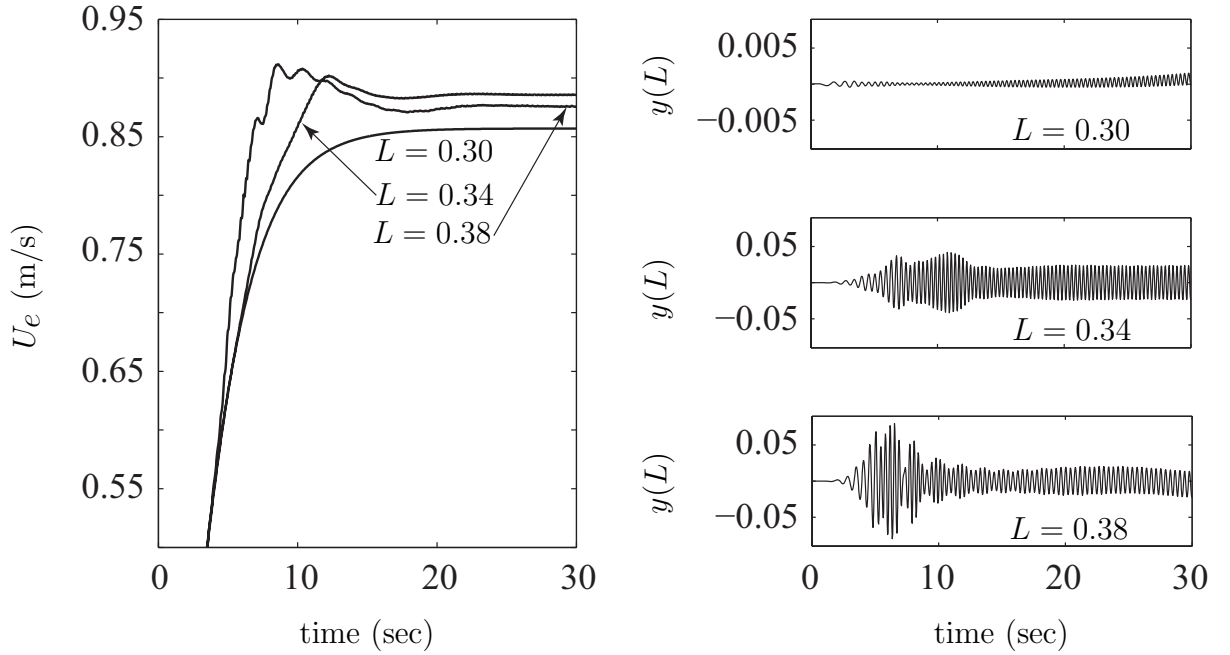


Figure 4.8: The subplot on the left shows the forward speed of the submersible with $L = 0.30$, 0.34 and 0.38 where $h = 0.077$. On the right, the displacement of the tail tip $y(L)$ is shown for these tail configurations.

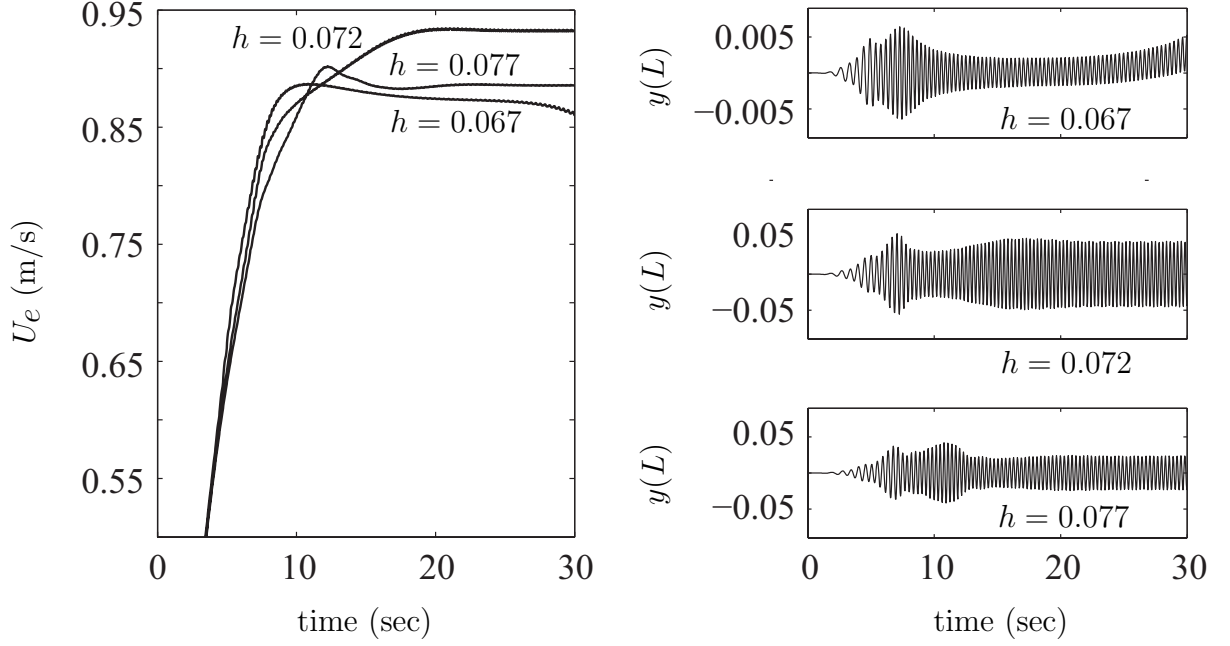


Figure 4.9: The subplot on the left shows the forward speed of the submersible with $h = 0.067$, 0.072 and 0.077 where $L = 0.34$. On the right, the deflection of the tail tip $y(L)$ is shown for these tail configurations.

4.7 Validation

The most robust form of simulation validation is comparison to experimental data, which will be presented in the following section. While the complexity of the equations presented in this chapter precludes comparison to an analytical solution, it is possible to compare a numerical solution of a simplified version of the system to a analytical solution of that simplified system. This approach cannot provide validation of system's full dynamics, but can at least provide assurance that the numerical method and base terms are correct. Here, a comparison between the numerical and analytical solutions of a cantilever will be undertaken.

The analytical method used will be the same as that presented in Chapter 2. The tail simulated will be the same as the “baseline” case from the configuration study in the prior section ($h = 0.772$ m, $L = 0.34$ m). Consistent with the modeling from Chapter 2, the

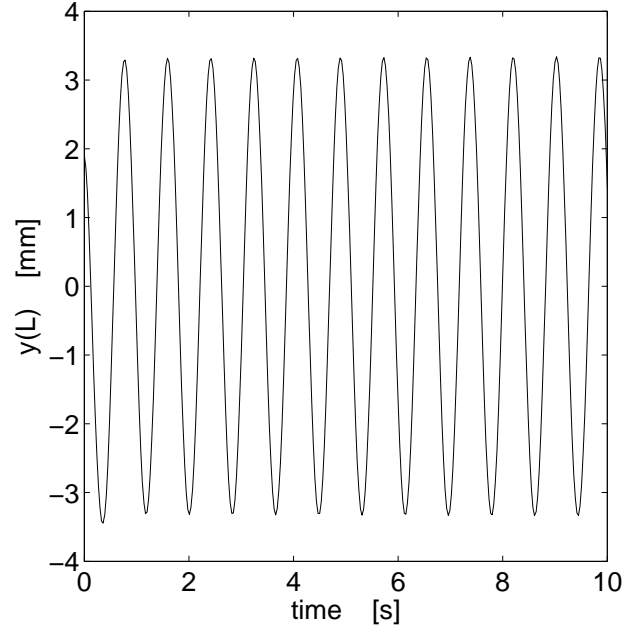


Figure 4.10: Displacement of the tail tip $y(L)$ in mm for a cantilever, $U = U_{cr} = 2.372$ m/s. Neutral stability is evident, since the oscillations of the tail are neither growing nor shrinking over time.

effects of the external flow will be neglected. For this system, the non-dimensional mass ratio, critical velocity, and critical frequency are

$$\begin{aligned}\beta &= \frac{m_2}{m_t + m_2} = 0.274 \\ u_{cr} &= \left(\frac{m_2}{LEI} \right)^{1/2} LU_{cr} = 6.619 \\ \omega_{cr} &= \left(\frac{m_t + m_2}{LEI} \right)^{1/2} \Omega_{cr} L^2 = 13.801\end{aligned}$$

where U_{cr} is the internal velocity at the onset of instability, and Ω_{cr} is the radian frequency of oscillation at the onset of instability. For this system, the equations above predict $U_{cr} = 2.372$ m/s. The full equations of motion were constrained such that the rigid head was held stationary, and solved with $U = U_{cr}$.

Figure 4.10 shows the displacement of the tail tip $y(L)$ of the simulated tail. Notice that the amplitude is constant over the length of the trial; since the system being simulated has no energy dissipation (drag), a constant amplitude of oscillation means that the simulation predicts a neutrally-stable system for $u = 6.619$. The period of oscillation is 0.827 sec., which yields a critical frequency value of $\omega_{cr} = 13.79$, which agrees with analytical predictions to within 0.1 percent. This agreement, coupled with the experimental comparisons presented in the next chapter, provides some confidence in the simulation method presented in this chapter.

Chapter 5

Experimental Studies and Control

5.1 Introduction

Devices which moved like fish have been produced by the academic community since the 1930's, with a series of results by James Gray. Gray, using mechanical [13] and electric/galvanic means [14], was able to induce swimming motions in the bodies of dead eels. A great deal of more recent work has been done in the Draper Laboratories at MIT, which produced the well-known RoboTuna [5, 43]. RoboTuna and its sister RoboPike use articulated tails covered by flexible sheaths. The tails of these vessels are individually actuated such that the resulting waveforms closely resemble those of living fish, a technique known as "biomimicry".

Articulated systems comprise the bulk of the experimental platforms; a non-biomimetic articulated system was built by McMasters and coworkers [27] which used a novel geared mechanism to produce a fish-like motion using only a single servomotor. Saimek and Li [35] designed a two-link tail with a motor at the base of the first link to achieve heave and

pitch motion similar to that described in Anderson, et al. [2]. Yu, et al. [45] constructed an articulated system and designed tail motion for three types of turning behaviors. The work on articulated systems has not been confined to “traditional” servomotor transmissions; Guo, et al. [16] and Chen, et al. [10] used electrically active polymers for actuation.

An alternate approach was taken by Alvarado and Youcef-Toumi [1], who described a system which used a flexible tail excited with a single actuator at the base. Paidoussis’ work [28] on a system similar to the one proposed in this communication also falls into this class of “underactuated” tails. An intermediate form between the infinitely continuous beam-like tails and discrete systems was described by Harper et al.[18], who constructed an articulated tail which was actuated in series with lateral and torsional springs. A properly designed underactuated tail has natural dynamics which are similar to the desired tail waveform, which allows the use of a lower bandwidth apparatus. Underactuated systems are also likely to have lower transmission losses, since there are unactuated degrees of freedom. Helpful natural dynamics and unactuated degrees of freedom do lead to certain other difficulties, however. A flexible tail which naturally vibrates with a good waveform for straight-line swimming will need to resist those dynamics in order to maneuver. Control of unactuated degrees of freedom is likewise more difficult, since the system’s natural dynamics must be taken into consideration.

This chapter is organized as follows. Section 5.2 describes an experimental platform designed at Michigan State University, and provides some preliminary results from that device. Section 5.3 extends the analysis provided in the previous chapter to include time-variable internal flow. A method which can be used to turn the submersible is described.

5.2 Experiments

A series of tests has been performed in the diving well of Michigan State University’s intramural pool with an experimental realization of the submersible described in the previous chapter. This prototype is shown in Fig.5.1. The submersible’s speed was determined for the flexible tail, rigid tail and rigid tube configurations which are described in the previous section. The presence of the tube, as opposed to simply removing all attachments from the tail barb, was required in order to stabilize the vehicle; it was found that removing the tube led to a pitch instability of the hull. Note that the simulations of the rigid tube configuration described in the previous section account for the drag on this tube, as opposed to simply simulating the “no tail” case, as might seem natural.

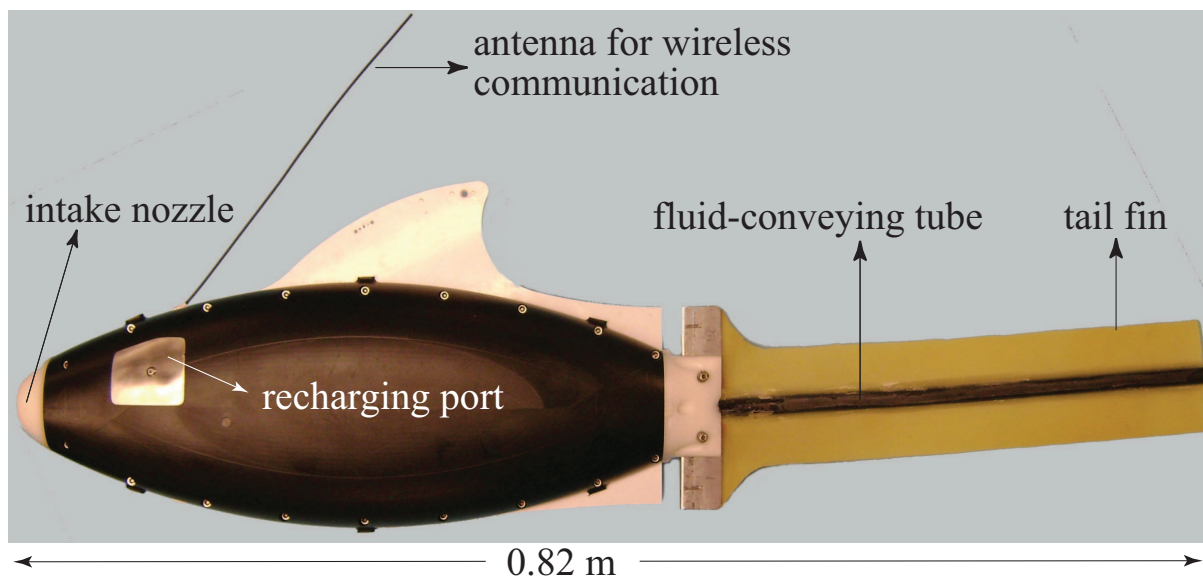


Figure 5.1: Exterior of the current prototype SPI, with marked features of interest. For interpretation of the references to color in this and all other figures, the reader is referred to the electronic version of this dissertation.

The prototype’s ellipsoidal Delrin hull is sealed via an integral silicone gasket; the hull is of monocoque construction, in that there is no separate “frame” upon which internal

components are mounted. The intake nozzle is also made of Delrin, and has an elliptical profile to reduce losses. The fluid is expelled from the hull through a hose barb upon which the tails are fitted. The prime mover is a Rule inline bilge pump rated at 500 gallons per hour. We have found that the major and minor losses of the flow system limit the flow rate to approximately 40% of this rated value. This prime mover and the control electronics are powered by 20 NiMH AA cells. The control electronics consist of an ATmega1284 microcontroller which provides a PWM signal to the prime mover's driving circuitry and receives wireless communications from the surface; this communication method requires that testing occur at or near the surface. The hull was designed to be excessively buoyant with these components; to achieve nearly neutral buoyancy, sticks of lead are added to the interior. This allows us to move the center of mass of the hull away from the centerline to counteract roll moments. The center of mass can also be moved fore and aft, in order to change the pitch of the submersible.

The submersible's flexible tail ($L = 0.34$ m) is made of two 1/20 inch thick latex sheets bonded to a latex tube (5/16 inch ID, 3/8 inch OD) using waterproof silicone RTV. The specific gravity of the latex is ≈ 0.96 , and is approximately neutrally buoyant. The tail's geometry is that of a finned tube, as shown in Fig.4.5, and the height of the tail is $h = 0.077$ m. The rigid tail, which has identical span and length, is made of an identical latex tube as that of the flexible case, bonded to two sheets of polypropylene with waterproof silicone RTV. The polypropylene has a specific gravity of ≈ 0.95 and is nearly neutrally buoyant. The rigid tube is made of a polycarbonate tube (3/8 inch ID, 7/16 inch OD) which has been found to fit over the barbed fitting at the rear of the submersible without leaks. A small aluminum nozzle (5/16 inch ID) has been fitted into the end of the rigid tube to ensure that

the exit velocity of this configuration is the same as the flexible and rigid tail cases.

The SPI prototype described here was designed primarily by Mr. Paul Streffling, and his M.S thesis [40] contains additional details regarding its construction.

5.2.1 SPI Performance



Figure 5.2: High-speed images of the submersible with the flexible tail acquired over a period of 1 sec, soon after it started from rest in the MSU swimming pool. The average speed of the submersible in these images was $\approx 0.4 \text{ BL/s}$, less than the maximum speed of $\approx 1.15 \text{ BL/s}$. Note the large deflections of the tail which occur during acceleration.

Figure 5.2 is sequence of images taken over 1 sec of operation; these images were acquired while the submersible was accelerating from rest, during which time pictures could be taken more normal to the free surface to reduce glare. The reduced forward speed during acceleration also leads to a longer period of oscillation of the tail; Fig.5.2 indicates a period of 0.8 seconds, compared to a period of $\approx 0.33 \text{ sec.}$ observed when the submersible is at top speed.

The prototype currently lacks control surfaces, which required the trials to be conducted using a guide string. This string runs through a tube affixed to the dorsal fin; there is considerable play in the interface between the tube and string, and small rotations of the rigid hull are visible during operation in the pitch, roll and yaw axes. The average speed

of the submersible is measured by analyzing 30 frame/sec video taken during operation; the guide string has been marked at two locations 9.14 *m* apart, and the times at which the submersible crosses these marks can be determined, and the speed calculated. The tests were conducted relatively near the surface of the pool, to enable wireless control of the throttle at the start of the run. In order to limit the loss of energy due to free surface effects, the mass and center of mass of the rigid head were adjusted such that the measured portion of the run was entirely below the surface.

The average speed of each configuration is given in Table 5.1. The reader will note that only the speed for each configuration is cited, rather than individually listing the thrust and drag of each configuration. This is consistent with the approach taken in the prior chapter; for a self-propelled swimming body the sources of drag and thrust cannot be conveniently separated, unlike a conventional propeller-driven craft.

Table 5.1: Mean speeds of the three configurations in experiments

Configuration	Trials	Speed [m/s]	Speed [BL/s]
Rigid Tube	5	0.918	1.176
Rigid Tail	10	0.878	1.126
Flexible Tail	4	0.889	1.139

The relatively low number of trials is the result of selecting trials for which the prototype is traveling in a relatively straight line, and not interacting with the guide string; these runs can be determined after the fact, by using the video data. Figure 5.3 provides essentially the same data as Table 5.1 with included error bars. It is clear that the general trend found in simulation (Fig.4.6) is verified by experiment; a fluttering flexible tail has superior performance to a rigid tail of identical dimension, but does not necessarily exceed the performance of a rigid tube. The speed of each configuration in simulation is also similar to the value

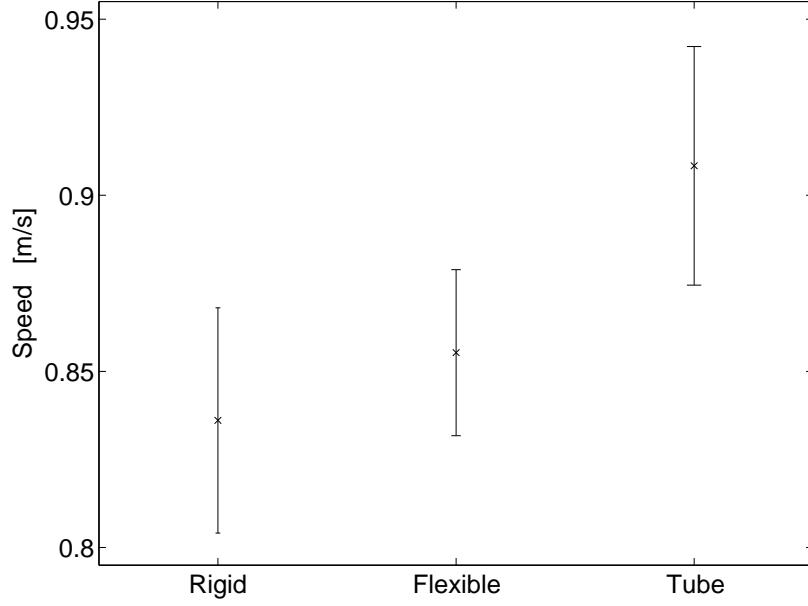


Figure 5.3: Mean speeds of the configurations listed in Table 5.1. The error bars express the 95% confidence intervals.

found by experiment, though this is to be expected, since experimental values were used to calibrate the drag coefficients used in simulations. The ≈ 0.33 sec. period of oscillation varies slightly from the 0.306 sec. period found in simulation. However, the shape of the tail is similar, in that the tail appears to conform to a second mode waveform. Note also that the experimental period is difficult to determine precisely from the relatively slow video used in these experiments.

5.3 Effect of Time-Varying Internal Fluid Velocity

5.3.1 Additional Terms

The equations of motion can be modified to account for a time-variable conveyed fluid velocity. The following changes will be made in the derivation presented in Section 4.4:

Head Internal Fluid: Ω_1

$$\text{Replace: } \ddot{\vec{r}}_{xy} = 0 \quad \text{With: } \ddot{\vec{r}}_{xy} = \dot{U}_h \hat{i}$$

Tail Internal Fluid: Ω_2

$$\text{Replace: } \ddot{\vec{r}}_{xy} = (\ddot{y} + 2U\dot{y}' + U^2 y'') \hat{j} \quad \text{With: } \ddot{\vec{r}}_{xy} = \dot{U} \hat{i} + (\ddot{y} + 2U\dot{y}' + U^2 y'' + \dot{U} y') \hat{j}$$

Expanded per Eqs.(4.18) and (4.20), the above replacements require that the following terms be added to the scalar equations of motion, Eqs.(4.45), (4.46) and (4.47):

$$\begin{aligned} \text{Eq.(4.45) :} & \quad m_1 \dot{U}_h + m_2 \dot{U} \\ \text{Eq.(4.46) :} & \quad m_2 \dot{U} \frac{y(L)}{L} \\ \text{Eq.(4.47) :} & \quad m_1 r_{cy} \dot{U}_h + \frac{m_2}{L} \dot{U} \int_0^L \left[(x - r_{cx}) y' - (y - r_{cy}) \right] dx \end{aligned}$$

The equation of motion for the flexible beam must also be expanded to account for the time-variable internal fluid velocity. The rate of change of momentum used in Eq.(4.55) is therefore:

$$\frac{\partial \vec{V}}{\partial t} = \ddot{\vec{R}}_0 + \dot{U} \hat{i} + \left[\ddot{y} + 2U\dot{y}' + U^2 y'' + \dot{U} y' \right] \hat{j} + \ddot{\theta} \left[x \hat{j} - y \hat{i} \right] + 2\dot{\theta} \left[U \hat{j} - (\dot{y} + U y') \hat{i} \right]$$

With the addition of these terms, Eq.(4.58) is replaced with the following expression:

$$\frac{\partial T}{\partial x} - A_2 \frac{\partial p_2}{\partial x} - A_6 \frac{\partial p_4}{\partial x} = \left(\frac{m_t + m_2 + m_4 k_t^{xx}}{L} \right) a_x + \frac{m_2}{L} \dot{U} + \frac{m_4 k_t^{xx}}{L} \dot{U}_e - D_t^x$$

Equation (4.60) is replaced by

$$D_t^y - EI \frac{\partial^4 y}{\partial x^4} + \frac{\partial}{\partial x} \left[(T - A_2 p_2 - A_6 p_4) \frac{\partial y}{\partial x} \right] = \left[\frac{m_2}{L} U^2 + \frac{m_4 k_t^{yy}}{L} U_e^2 \right] \frac{\partial^2 y}{\partial x^2} \quad (5.1)$$

$$+ 2 \frac{m_2 U + m_4 k_t^{yy} U_e}{L} \frac{\partial^2 y}{\partial x \partial t} + \frac{m_2 \dot{U} + k_t^{yy} m_4 \dot{U}_e}{L} \frac{\partial y}{\partial x} + \frac{m_t + m_2 + m_4 k_t^{yy}}{L} \left(\frac{\partial^2 y}{\partial t^2} + a_y \right)$$

where the tension-pressure gradient term in Eq.(5.1) is replaced by:

$$\frac{\partial}{\partial x} \left[\left(\frac{\partial T}{\partial x} - A_2 \frac{\partial p_2}{\partial x} - A_6 \frac{\partial p_4}{\partial x} \right) \frac{\partial y}{\partial x} \right] =$$

$$\left[\frac{m_t + m_2 + m_4 k_t^{xx}}{L} a_x + \frac{m_2}{L} \dot{U} + \frac{m_4 k_t^{xx}}{L} \dot{U}_e - D_t^x \right] \frac{\partial y}{\partial x}$$

$$\left[- \int_x^L \left[\frac{m_t + m_2 + m_4 k_t^{xx}}{L} a_x + \frac{m_2}{L} \dot{U} + \frac{m_4 k_t^{xx}}{L} \dot{U}_e - D_t^x \right] dx + D_t^b \right] \frac{\partial^2 y}{\partial x^2} \quad (5.2)$$

Substitution of Eq.(4.58) into Eq.(5.1) yields the modified equation of motion:

$$EI \frac{\partial^4 y}{\partial x^4} + \left[\frac{m_2}{L} U^2 + \frac{m_4 k_t^{yy}}{L} U_e^2 \right.$$

$$\left. + \int_x^L \left(\frac{m_t + m_2 + m_4 k_t^{xx}}{L} a_x + \frac{m_2}{L} \dot{U} + \frac{m_4 k_t^{xx}}{L} \dot{U}_e - D_t^x \right) dx - D_t^b \right] \frac{\partial^2 y}{\partial x^2}$$

$$+ \left[- \frac{m_t + m_2 + m_4 k_t^{xx}}{L} a_x - \frac{m_4 (k_t^{xx} - k_t^{yy})}{L} \dot{U}_e + D_t^x \right] \frac{\partial y}{\partial x}$$

$$+ 2 \left[\frac{m_2}{L} U + \frac{m_4 k_t^{yy}}{L} U_e \right] \frac{\partial^2 y}{\partial x \partial t} + \frac{m_t + m_2 + m_4 k_t^{yy}}{L} \left(\frac{\partial^2 y}{\partial t^2} + a_y \right) - D_t^y = 0 \quad (5.3)$$

It is interesting to note that no analog of the $\dot{U}_e \frac{\partial y}{\partial x}$ term appears for \dot{U} . This is consistent with a previous derivation of the equation of a fluid-conveying with time variable internal flow [32]. For internal flow, there is no difference between the effective mass acting in the x

and y directions, meaning that the $(k_t^{xx} - k_t^{yy})$ term is effectively zero for internal flow.

5.3.2 Numerical Simulations

Addition of the terms associated with \dot{U} and \dot{U}_h requires that two additional states be added to the discretized equations of motion, such that

$$\begin{aligned}\dot{U} &= f_u(X_0, Y_0, \theta, y_i, \dot{X}_0, \dot{Y}_0, \dot{\theta}, \dot{y}_i, t) \\ \dot{U}_h &= f_h(X_0, Y_0, \theta, y_i, \dot{X}_0, \dot{Y}_0, \dot{\theta}, \dot{y}_i, t)\end{aligned}$$

Note that if \dot{U} and \dot{U}_h are explicit functions of only time, no additional states need to be added to the discretized equations, since U and U_h can be computed *a priori*. We will also make another assumption:

A10. At any time, the mass flux through the inlet Γ_1 is equal to that through the control surface at the tip of the tail, Γ_2 . This precludes fluid storage within the rigid head of the submersible, and implies that $\dot{U}_h = (A_2/A_1)\dot{U}$.

The functional description of \dot{U} is as follows:

$$\dot{U} = \alpha \dot{y}(kL) \quad U(0) = 4.0 \quad (5.4)$$

where α is a scaling parameter, and $\dot{y}(kL)$ is the velocity of a given point on the flexible tail. Functions of this type have several favorable properties, not least of which is the ease of implementation within the simulation. While we have yet to do so, it is also easy to experimentally implement the sensing required for this type of function, since it requires a single point measurement at a point on the beam. This is in contrast to a function requiring

knowledge of one or more *spatial* derivatives, or an approximation of the integral of the beam position.

It is easy to understand why a function in this form can cause the vehicle to turn; since $\dot{y}(kL)$ is signed, the thrust from the jet may be unbalanced with respect to the centerline of the vehicle. The degree of imbalance is related to the point k at which the measurement is taken, because of the traveling nature of the beam's waveform. Essentially, by moving the point k nearer to the head of the vehicle, we can mimic a phase shift between the observed value of $\dot{y}(kL)$ and \dot{U} .

In the figures which follow, the tail is the “baseline” tail described in the previous section: $L = 0.34$, $h = 0.077$. In addition, the value for U has been subjected to upper and lower saturation such that $3.8 \leq U \leq 4.2$; removal of these limits affects neither system stability nor the qualitative results, but it is difficult to keep the average velocity between cases the same without imposing them. Furthermore, similar limits are likely to be imposed by any physical pump.

Figure 5.4 gives a comparison of the constant velocity case where $U = 4.0$ and the non-constant velocity case where $\alpha = 40$, $k = 0.75$. The total rotation of the vehicle θ is given in the left axes, and the right axes depict the forward speed of the vehicle U_e and the conveyed fluid velocity $U(t)$. It is clear from the left axes of Fig.5.4 that the $U = U(t)$ case is subject to a net moment over the course of its travel, making a clockwise turn of $\approx 1 \text{ rad.}$ relative to the $U = \text{const}$ case. The middle right axes show the forward speed of the vehicle for both cases, and U_e for both cases can be seen to be very similar; the top right axes show that there are larger fluctuations in the forward speed of the $U = U(t)$ case. The conveyed fluid velocity is shown in the bottom right axes, and the increase in $U(t)$ amplitude and eventual

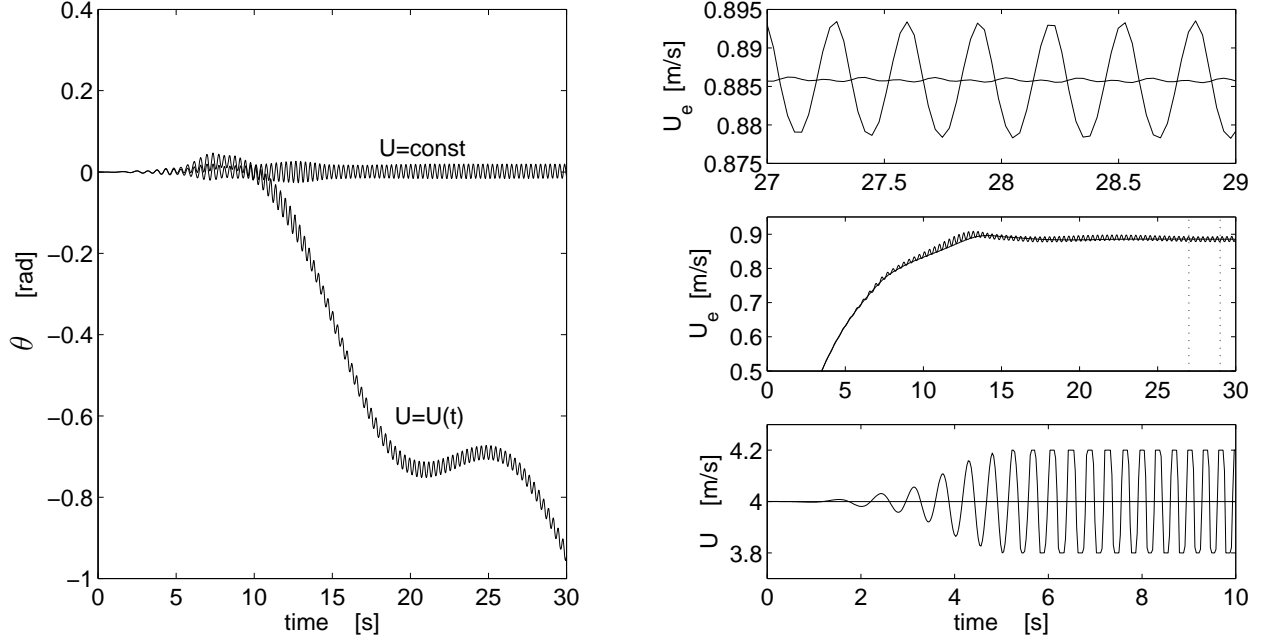


Figure 5.4: Comparison of the constant-velocity $U = 4.0$ case to non-constant velocity case where $\alpha = 40$, $k = 0.75$

saturation is clearly visible. Note that the time scale of the $U(t)$ plot is $1/3$ that of the $U_e(t)$ plot.

Figure 5.5 compares the behavior of three values of k : 0.25, 0.75 and 1.0. The left axes show θ for each case. The right set of axes shows the orientation of each at $t = 20 \text{ sec.}$, marked with a dashed line on the θ axes.

The different behavior of each value of k is evident from each case's θ curve. Measuring the beam velocity at different points places $U(t)$ in different phase with respect to the orientation of the tip of the tail, due to the traveling wave nature of the tail's waveform. A measurement point of $k = 0.75$ corresponds to a large negative moment, $k = 1.0$ a smaller negative moment, and the direction of turn can be reversed by measuring at $k = 0.25$. A physical realization of this type of control is likely to simply reverse the sign of Eq.5.4 in order to reverse the direction of the moment, and it is likely that such a realization will use

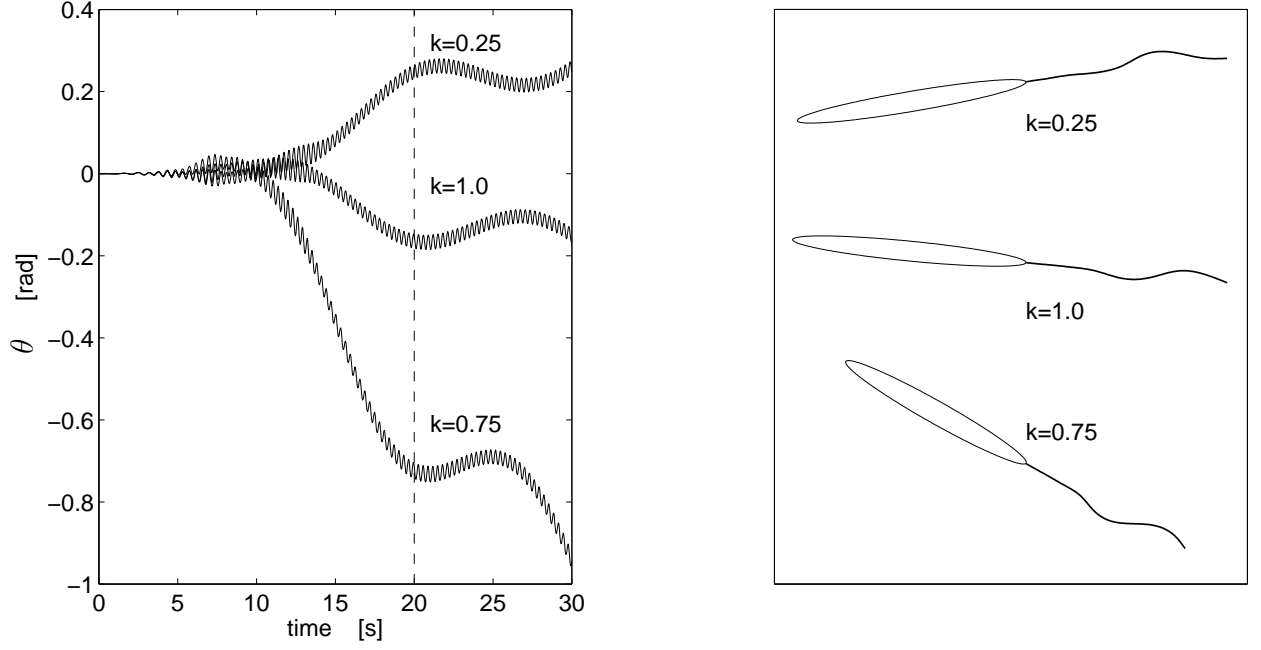


Figure 5.5: Comparison of three values of k : 0.25, 0.75 and 1.0. The scaling parameter $\alpha = 40$ for all cases.

a measurement point near $x = L$, to take advantage of the larger deflections there.

The sequence of images shown in Fig.5.6 have been acquired over one cycle of the tail where $U = U(t)$ with $\lambda = 0.75$ - note that the frame of reference pictured is the non-inertial (xy) frame. Compared to Fig.4.7, there is a distinct asymmetry to the tail's motion; this asymmetry is most clear at the tip of the tail, which spends a larger fraction of the cycle on the right half of the submersible's centerline. This asymmetry is the likely reason for the turning behavior - as the angle of surfaces Γ_2 and Γ_6 change throughout the cycle, fluid which enters through the inlet surfaces Γ_1 and Γ_3 is turned with respect to the centerline.

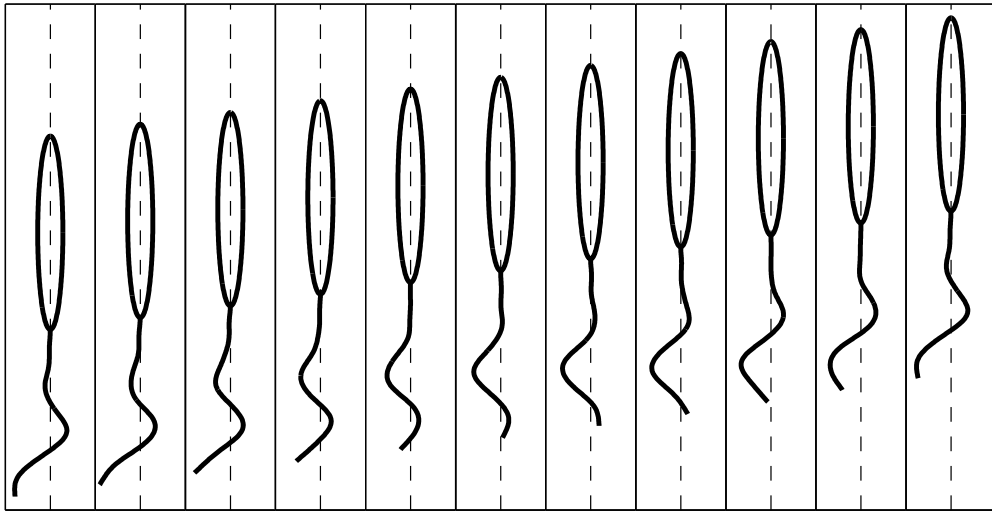


Figure 5.6: An image sequence of the submersible during a turn. Note that the dashed line is collinear with the non-inertial x axis.

Chapter 6

Concluding Remarks and Future Work

6.1 Dynamics of a Pipe Conveying Fluid with a Non-Uniform Velocity Profile

Chapter 2 assessed the dynamics of cantilever pipes conveying fluid with a fully developed non-uniform velocity profile. The equation of motion derived in that section is tractable, requiring only the use of a single empirical parameter μ to account for the dependence of fluid momentum on the square of the fluid velocity. Previous analyses made the assumption of a uniform velocity profile, implicitly assuming μ to be unity. While this assumption is reasonable at high Reynolds number, $\mu = 1$ is the minimum value possible, approached only in the limit of infinite Reynolds number. That is, the momentum flux for real fluid flows will always be greater than the uniform case, and the uniform profile assumption becomes monotonically less accurate as the Reynolds number decreases.

It was shown that the dependence of u , the non-dimensional velocity relevant to the stability of the pipe, is not uniquely dependent on the Reynolds number. Since the Reynolds number determines the velocity profile, a uniform velocity profile may not be generally assumed near the onset of flutter instability, despite the requirement of high u . This is particularly relevant for laminar flow, where the value of μ reaches its maximum value; as the scale of “engineering applications” shrinks, the dynamics of pipes conveying laminar flow with high nondimensional velocity u may become relevant.

The stability characteristics of a sample pipe were assessed with our updated model. In this pipe, the fluid became turbulent at relatively low u with the effect that $\mu \approx 1.05$ when u approached values necessary to achieve flutter instability. This proximity to the uniform model causes similarity between the predictions over much of the parameter space, a similarity which is to be expected since the predictions of the uniform model have been qualitatively verified by experiment. There are significant differences in certain sensitive regions of the parameter space, such as near $\beta = 0.3$ and $\beta = 0.7$. A pipe with dimensions such that the conveyed fluid is laminar at the onset of flutter instability exhibited markedly different stability characteristics from the uniform case. Both the critical velocity and critical frequency were significantly different over large regions of the parameter space.

6.2 Simplified Dynamics of a Fluid-Conveying, Fluid-Immersed Pipe Affixed to a Rigid Body

Chapter 3 derived the equations of motion for an immersed fluid-conveying tail affixed to a rigid body. It was shown that both the cantilever and free pipe can be expressed as special

cases of the rigid body boundary condition. The neutral stability curve in u_i - u_e space was computed over a wide range of values of the rigid body mass fraction. The serpentine nature of these curves renders it difficult to make statements about the entire parameter space; nonetheless, some local trends can be observed. At low values of u_e , a tail affixed to a rigid body of larger mass become unstable at lower values of u_i , but this trend is reversed for higher values of u_e . The system's stability was also found to be largely insensitive to additional rigid body mass above $\mu = 25$, *i.e.*, the system's behavior is largely indistinguishable from that of a cantilever.

Estimates of the sign of the thrust produced by the fluttering tail and the efficiency of that thrust have also been computed via methods first proposed by Lighthill [23]. Although this analysis is less robust than that proposed in Chapter 4, some general statements about the suitability of this type of propulsor can be made. A relatively high value of u_i is required to drive a thrust-producing flutter instability. Although a system of this type may permit flutter instability for $u_i = 0$, instability driven entirely by the external flow does not provide a thrust-producing motion. This $u_i = 0$ limit case is intuitively obvious, since a flapping flag does not produce thrust. The regions of the neutral stability curves where thrust is produced therefore have boundaries primarily defined by u_i , since the internal fluid flow is the only energy input to the system.

It is also clear that a less massive rigid head leads to thrust-producing instability at lower values of u_i , though these motions occur at lower forward velocity. Note also that the efficiency of the produced thrust is relatively insensitive to u_e over a wide range of u_e values. Similar observations have been made for live fish [34], which move with a waveform reminiscent of the traveling waveform generated by a fluid-conveying pipe. It is therefore

heartening that one of the great advantages of fish-like propulsion is preserved.

The analysis proposed in this chapter was confined to the mass of the rigid body, but it is possible to investigate the role of many other parameters for a vehicle of this type. Besides the parameters identified in this work, a terminal nozzle might be used at the free end, or a fish-like planform used for the shape of the tail. Analysis of the latter system must be performed numerically, and will likely be an adjunct to later work along the lines of that presented in Chapter 4.

6.3 General Dynamics of a Fluid-Conveying, Fluid-Immersed Pipe Affixed to a Rigid Body

Chapter 4 presented the planar equations of motion for a fluid-conveying submersible with a fluttering tail without many of the limiting assumptions used in Chapter 3. In particular, the only assumption made regarding the accelerations or rotations of the non-inertial frame attached to the submersible are that the accelerations and rotations occur within a single plane. This derivation therefore comprises the scalar equations for the motion of this non-inertial frame as well as the equation of motion for the fluid-conveying tail within the frame. These equations appear here for the first time in the academic literature likely because most applications for fluid-conveying pipes, such as pipeline vibrations or the simple “garden hose” problem, do not require analysis in a non-inertial frame.

These equations are solved for a variety of tail geometries, and one geometry is presented which produces thrust in excess of a rigid tube of equal length; this provides evidence of what our research group has termed “synergistic propulsion”, in which there is net thrust provided

by the fluttering motion of the tail, in addition to the thrust of the fluid jet. This particular finding has yet to be verified by the experimental work described in Chapter 5, though the speed of a device with a fluttering tail has been shown to exceed that of the device with a dimensionally identical rigid tail. This finding is the same as that of Paidoussis [28], since that work compared the fluttering and non-fluttering tails by placing an additional stiffener on the flexible tail.

The methods laid out in this chapter are likely to be the basis for much of the future work done on this topic; indeed one such “future” topic, control of a fluttering fluid-conveying submersible, is touched upon in Chapter 5 of this communication. This type of empirically-based numerical analysis is perhaps a bridge between the analytical methods typified by the work in Chapter 3 and a full-blown CFD simulation. In addition to further work on control, extension of these methods to non-uniform tail geometries is planned for the future. A fish-like planform, with a large reduction in area near the tip of the tail, has been shown [25] to be highly efficient for producing thrust on the basis of slender-body theory. A beam with a fish-like planform will be relatively weak at a location near its end, and then much stiffer in that portion which mimics the caudal fin. This should lead to a large, out-of-phase angle between this “fin” and the forward portion of the tail, a condition which is seen in swimming fish.

The large angles and large amplitudes associated with non-uniform tail geometries require that the effects of large displacements be accounted for. The equations of motion of a fluid-conveying Euler elastica have been presented before [4] [39], though neither of the cited works considered either external flow or a non-uniform pipe/beam geometry. Extension to these conditions is planned for future work.

6.4 Experimental Studies and Control

Chapter 5 describes a prototype version of a fluttering fluid-conveying submersible that was produced at Michigan State University. Much of the credit for the prototype's design and construction is due to Mr. Paul Streffling, and his M.S. thesis [40] may be used as a more complete source of information about the platform. Preliminary findings qualitatively verify the model proposed in Chapter 4. A great deal of work remains to be done on the experimental hardware. Communication with the device as currently constructed is not possible through water, which means that it is difficult test in a way which removes free-surface effects. Underwater communication is likely to be added soon, as is buoyancy control, to permit running at greater depth.

The equations of motion derived in Chapter 4 have also been extended to permit the use of a time-variable internal fluid velocity, and a simple function for this velocity has been shown to turn the submersible. This function requires the velocity measurement of a single point on the tail; changing this measurement point leads to a phase shift in internal fluid velocity which can be exploited to turn the submersible in both directions. The potential ability to maneuver by changing the internal flow rate is a useful feature, since it would allow control of the submersible without additional control surfaces, such as fins.

The function proposed for the internal fluid velocity produced reasonable turning rates, but it is likely that there is significant potential for improvement by using information about additional states of the system. In particular, Eq.(5.4) contains no information about the global coordinates X , Y , θ in its definition for $\dot{U}(t)$; knowledge of the state of the non-inertial frame will certainly be required for trajectory tracking. Note also that the turn shown in Fig.5.4 takes place over many oscillations of the tail, and the image sequence shown in Fig.

5.6 shows a tail which is oscillating asymmetrically, but not wildly so. It is therefore likely that the device is nowhere near its limits of its turning performance; a functional description for $\dot{U}(t)$ which leads to a more asymmetric oscillation of the tail is likely to increase the turning rate of the vehicle.

BIBLIOGRAPHY

BIBLIOGRAPHY

- [1] PV Alvarado and K Youcef-Toumi. Design of machines with compliant bodies for biomimetic locomotion in liquid environments. *ASME J. Dynamic Systems, Measurement, and Control*, 128:3–13, 2006.
- [2] JM Anderson, K Streitlien, DS Barrett, and MS Triantafyllou. Oscillating foils of high propulsive efficiency. *Journal of Fluid Mechanics*, 360:41–72, 1998.
- [3] H. Ashley and G. Haviland. Bending vibrations of a pipeline containing fluid. *Journal of Applied Mechanics*, 17:229–232, 1950.
- [4] AK Bajaj, PR Sethna, and TS Lundgren. Hopf bifurcation phenomena in tubes carrying fluid. *SIAM Journal of Applied Mathematics*, 39:213–230, 1980.
- [5] DS Barrett, MS Triantafyllou, DKP Yue, and M Wolfgang. Drag reduction in fish-like motion. *J. Fluid Mechanics*, 392:183–212, 1999.
- [6] GK Batchelor. *An Introduction to Fluid Mechanics*. Cambridge University Press (London), 1967.
- [7] R Benedict. *Fundamentals of Pipe Flow*. John Wiley and Sons, 1980.
- [8] RB. Bhat and H. Wagner. Natural frequencies of a uniform cantilever with slender tip mass in the axial direction. *Journal of Sound and Vibration*, 46(2):304–307, 1976.
- [9] CE Brennan. A review of added mass and fluid inertial forces. Technical report, Naval Civil Engineering Laboratory, 1982.

- [10] Z Chen, S Shatara, and X Tan. Modeling of biomimetic robotic fish propelled by an ionic polymer metal composite caudal fin. *IEEE/ASME Transactions on Mechatronics*, 15(3):448–459, 2010.
- [11] HK Cheng and L Murillo. Lunate tail swimming propulsion as a problem of curved lifting line in unsteady flow. *Journal of Fluid Mechanics*, 143:327–350, 1984.
- [12] FE Fish. The myth and reality of gray’s paradox: implication of dolphin drag reduction for technology. *Bioinspiration & Biomimetics*, 1:R17–R25, 2006.
- [13] J Gray. Studies in animal locomotion. i. the movement of fish with special reference to the eel. *Journal of Experimental Biology*, 10:88–104, 1933.
- [14] J. Gray. Studies in animal locomotion vi. the propulsive powers of the dolphin. *Journal of Experimental Biology*, 13:192–199, 1936.
- [15] R.W. Gregory and M.P. Paidoussis. Unstable oscillation of tubular cantilevers conveying fluid. i. theory. *Proceedings of the Royal Society (London)*, 293:512–527, 1966.
- [16] S. Guo, T. Fukuda, and K. Asaka. A new type of fish-like underwater microrobot. *IEEE/ASME Transactions on Mechatronics*, 8(1):136–141, 2003.
- [17] MJ Hannoyer and MP Paidoussis. Instabilities of tubular beams simultaneously subjected to internal and external axial flows. *ASME Journal of Mechanical Design*, 100:328–336, 1978.
- [18] KA Harper, MD Berkemeier, and S Grace. Modeling the dynamics of spring-driven oscillating-foil propulsion. *IEEE J. Oceanic Engineering*, 23:285–296, 1998.
- [19] AM Hellum, R Mukherjee, and AJ Hull. Dynamics of pipes conveying fluid with non-uniform turbulent and laminar velocity profiles. *Journal of Fluids and Structures*, 26(5):804–813, 2010.
- [20] AM Hellum, R Mukherjee, and AJ Hull. Flutter instability of a fluid-conveying fluid-immersed pipe affixed to a rigid body. *Journal of Fluids and Structures*, In Press, 2011.
- [21] SF Hoerner. *Fluid-Dynamic Drag*. Self Published, 1958.
- [22] GV Lauder, EJ Anderson, J Tangorra, and Madden PGA. Fish biorobotics: kinematics and hydrodynamics of self-propulsion. *Journal of Experimental Biology*, 210:2767–2780, 2007.

- [23] M.J. Lighthill. Note on the swimming of slender fish. *Journal of Fluid Mechanics*, 9:305–317, 1960.
- [24] M.J. Lighthill. Hydrodynamics of aquatic animal propulsion. *Annual Review of Fluid Mechanics*, 1:413–446, 1969.
- [25] M.J. Lighthill. Aquatic animal propulsion of high mechanical efficiency. *Journal of Fluid Mechanics*, 44:265–301, 1970.
- [26] MJ Lighthill. Large-amplitude elongated-body theory of fish locomotion. *Proceedings of the Royal Society (London)*, B179:125–138, 1971.
- [27] RL Mcmasters, CP Grey, JM Sollock, R Mukherjee, A Benard, and AR Diaz. Comparing the mathematical models of lighthill to the performance of a biomimetic fish. *Bioinspiration & Biomimetics*, 3:1–8, 2008.
- [28] MP Paidoussis. Hydroelastic ichthyoid propulsion. *AIAA Journal of Hydronautics*, 10:30–32, 1976.
- [29] MP Paidoussis. Marine propulsion apparatus. US Patent 4,129,089, December 1978.
- [30] M.P. Paidoussis. *Fluid-Structure Interactions: Slender Structures and Axial Flow, Volume 1*. Academic Press, 1998.
- [31] MP Paidoussis. *Fluid-Structure Interactions: Slender Structures and Axial Flow, Volume 2*. Academic Press, 2004.
- [32] M.P. Paidoussis and N.T Issid. Dynamic stability of pipes conveying fluid. *Journal of Sound and Vibration*, 33:267–294, 1974.
- [33] MC Potter and JF Foss. *Fluid Mechanics*. Great Lakes Press, 1982.
- [34] J. Rohr and F. Fish. Strouhal number and optimization of swimming by odontocete cetaceans. *SSC San Diego Biennial Review*, pages 175–178, 2006.
- [35] S Saimek and PY Li. Motion planning and control of a swimming machine. *Int. J. of Robotics Research*, 23:27–53, 2004.
- [36] J Saroudis. Propulsion by oscillating plates. B. Eng. Honours Thesis, Department of Mechanical Engineering, McGill University, Montreal, Canada, 1974.

- [37] WW Schultz and PW Webb. Power requirements of swimming: do new methods resolve old questions? *Integrative and Comparative Biology*, 42:1018–1025, 2002.
- [38] AP Seiranyan. Collision of eigenvalues in linear oscillatory systems. *Journal of Applied Mathematics and Mechanics*, 58 (5):805–813, 1994.
- [39] M Stangl, J Gerstmayer, and H Irschik. An alternative approach for the analysis of non-linear vibrations of pipes conveying fluid. *Journal of Sound and Vibrations*, 310:493511, 2008.
- [40] P.C. Streffling. Experimental platform for studying the behavior and performance of a submersible propelled by a fluid-conveying fluttering tail. Master’s thesis, Michigan State University, 2011.
- [41] L. Tang, M.P. Paidoussis, and J. Jiang. Cantilevered flexible plates in axial flow: Energy transfer and the concept of flutter-mill. *Journal of Fluids and Structures*, 326:263–276, 2009.
- [42] GI Taylor. Analysis of the swimming of of long and narrow animals. *Proc. of the Royal Society (London)*, A214:158–183, 1952.
- [43] MS Triantafyllou, GS Triantafyllou, and DKP Yue. Hydrodynamics of fishlike swimming. *Annual Review of Fluid Mechanics*, 32:33–53, 2000.
- [44] T. Yao-Tsu Wu. Hydromechanics of swimming propulsion. part 3. swimming and optimum movements of slender fish with side fins. *Journal of Fluid Mechanics*, 46:545–568, 1971.
- [45] J Yu, S Wang, and M Tan. A simplified propulsive model of bio-mimetic robot fish and its realization. *Robotica*, 23:101–107, 2005.